Geological Image Processing of Petrographic Thin Sections Using the Rotating Polarizer Stage

by

J. Scott Goodchild

A thesis

submitted to the Department of Earth Sciences

in partial fulfillment of the requirements

for the degree of

Master of Science

September, 1998

Brock University

St. Catharines, Ontario

Abstract

One of the fundamental problems with image processing of petrographic thin sections is that the appearance (colour / intensity) of a mineral grain will vary with the orientation of the crystal lattice to the preferred direction of the polarizing filters on a petrographic microscope. This makes it very difficult to determine grain boundaries, grain orientation and mineral species from a single captured image. To overcome this problem, the Rotating Polarizer Stage was used to replace the fixed polarizer and analyzer on a standard petrographic microscope. The Rotating Polarizer Stage rotates the polarizers while the thin section remains stationary, allowing for better data gathering possibilities.

Instead of capturing a single image of a thin section, six composite data sets are created by rotating the polarizers through 90^0 (or 180^0 if quartz c-axes measurements need to be taken) in both plane and cross polarized light. The composite data sets can be viewed as separate images and consist of the average intensity image, the maximum intensity image, the minimum intensity image, the maximum position image, the minimum position image and the gradient image.

The overall strategy used by the image processing system is to gather the composite data sets, determine the grain boundaries using the gradient image, classify the different mineral species present using the minimum and maximum intensity images and then perform measurements of grain shape and, where possible, partial crystallographic orientation using the maximum intensity and maximum position images.

Acknowledgments

In a major project such as this there are many people who give support and advice. First and Foremost, I would like to thank Frank Fueten for his suggestions and guidance over the past few years. Frank has been an outstanding supervisor and I am glad I was able to work with him on this project.

I would also like to thank my committee members Greg Finn and Brian Ross for providing helpful advice and direction when I needed it. I am also grateful to Mike Lozon for his skill and patience in helping produce the figures for this thesis.

Finally, I have my wife Mary to thank for her continuous support and encouragement over the past few years while I worked on this thesis.

Table of Contents

List of Figures

Chapter 1:
Introduction

Introduction

The study of mineral grains in thin sections of rock using a petrographic microscope is an important aspect of the geological sciences. Unfortunately, the use of image processing systems to aid in the study of thin sections has been limited (Fabbri 1984; Petruk 1989; Launeau et al. 1990; Starkey and Samantaray 1991; Pfleiderer et al. 1992; Starkey and Samantaray 1993; Samantaray 1993; Lumbreras and Serrat 1996). With a petrographic microscope a thin section may be viewed in either plane polarized or cross polarized light. Using cross polarized light, some mineral grains may exhibit interference colours similar to their neighbours at certain orientations relative to the polarizers, making the boundary between them difficult to observe. With plane polarized light, many mineral species appear colourless and of those that are coloured, some show variations of colour due to pleochroism. Consequently, the thin section must be rotated relative to the planes of polarization to clearly define all mineral grains present. Traditionally this has been accomplished by rotating the thin section relative to the fixed planes of polarization. Although the human vision system has no trouble keeping track of individual grains as they rotate around the field of view, it is a very difficult task for a computer based vision system. For an image processing system based on a rotating stage, the computer would have to keep track of the behaviour of points within a grain in colour space as well as the motion of these points as the stage is rotated.

A method for alleviating this problem was suggested by Starkey and Samantaray 1993. They found that manually rotating the polarizers while the

thin section remains in a fixed position would yield the results that the pixels in each sequential image remain registered. This idea was advanced by Fueten (1997) who designed a computer controlled Rotating Polarizer Stage. The Rotating Polarizer Stage replaces the upper and lower polarizers on a petrographic microscope. This allows for computerized control of the sampling process since the Rotating Polarizer Stage can automatically rotate its polarizers after each incremental image has been captured and processed. The ability of the stage to allow a thin section to remain fixed while the polarizers are rotated, keeps each point in the viewed area of a thin section registered to a specific pixel at all positions of the polarizers. This greatly reduces the computational requirements of the computer.

This thesis describes the use of the Rotating Polarizer Stage in image processing of petrographic thin sections. The Rotating Polarizer Stage is used in conjunction with an SGI Indigo2 computer equipped with a Galileo video capture board, capable of grabbing frames at a resolution of 640x480 pixels in 24 bit colour (8 bits each of red, green and blue). By obtaining data from images of a thin section at different polarizer positions, the Rotating Polarizer Stage provides an excellent platform for image processing of petrographic images. The data obtained with the stage provide an excellent input for determination of grain boundaries and therefore improves calculations of grain shape and size. Other data collected with the stage can be used to classify the different mineral species present in a thin section and to obtain partial crystallographic orientations of quartz grains within a thin section.

Structure Of The Thesis

The thesis consists of 6 chapters. The present chapter introduces image processing of petrographic thin sections and serves as an introduction to the following chapters.

- Chapter 2 discusses the design and implementation of the Rotating Polarizer Stage in image processing of petrographic thin sections.

- Chapter 3 describes the algorithm developed for automatic segmentation of an image of a thin section into its constituent mineral grains. The algorithm is applied to a composite image of the thin section that displays the summed gradient over a series of 200 images of the thin section. Each of the 200 images are taken at different orientations of the thin section relative to the planes of polarization. In some aspects the algorithm developed for edge detection is similar to the Canny edge detection method (Canny 1986).

- Chapter 4 presents the method developed for classifying the different mineral species present in a thin section. The method requires the image of the thin section to be well segmented such that each mineral grain is completely defined. The user then selects at least one example of each mineral species present in the thin section. The identification algorithm then uses these 'seed' grain(s) to identify the rest of the mineral grains in the thin section.

• Chapter 5 outlines the method of determination of *c*-axes orientations for quartz grains within a thin section. The algorithm is applied to two composite images. The first displays, for each pixel in the image, the maximum intensity obtained in a 180^0 rotation of the thin section relative to the planes of polarization. This image is used in determining *c*-axes inclination. The second composite image displays, for each pixel in the image, the position, relative to the planes of polarization, at which the maximum intensity occurred. This image is used in determining *c*-axes trend.

• Chapter 6 summarizes the conclusions of the thesis research.

Chapters 3 and 5 are written as publishable papers (not yet submitted) and have F. Fueten as a junior co-author. The contributions of the co-author to the two chapters can be summarized as follows:

1. The co-author contributed ideas, generated during discussions, which had a significant impact on the research.
2. The co-author provided scientific guidance and editorial comments on the drafts of the chapters.

References

Canny, J. (1986). A Computational Approach to Edge Detection. *IEEE Trans. Pattern Anal. Mach. Intell.* **PAMI-8(6)**, p. 679-698.

Fabbri, A.G., (1984). Image processing of geological data: *Van Nostrand-Reinhold, Wokingham, U.K. 224 p.*

Fueten, F., (1997). A computer controlled rotating polarizer stage for the petrographic microscope. *Computers & Geosciences* **Vol. 23**, p.203-208.

Launeau, P., Bouchez, J.-L. and Benn, K., (1990). Shape preferred orientation of object populations: automatic analysis of digitized images: *Tectonophysics*, **Vol. 180**, p. 201-211.

Lumbreras, F., Serrat, J. (1996). Segmentation of petrographic images of marbles. *Computers & Geosciences* **Vol. 22**, p.547-558.

Pfleiderer, S., Ball, D.G.A and Bailey, R.C. (1992). AUTO: A computer program for the determination of the two-dimensional auto-correlation function of digital images: *Computers & Geosciences*, **Vol. 19**, p. 825-829.

Petruk, W., ed. (1989). Image analysis in Earth Sciences: *Mineralogical Association of Canada Shortcourse Handbook*

Starkey, J. and Samantaray, A.K., (1991). An evaluation of noise reduction filters, with particular reference to petrographic images: *Journal of Computer-Assisted Microscopy*, **Vol. 3**, p. 171-188.

Starkey, J. and Samantaray, A.K., (1993). Edge detection in petrographic images: *Journal of Microscopy*, **Vol. 172**, p.263-266.

Samantaray, A.K., (1993). Computer-assisted Petrographic image analysis and quantization of Rock Textures: unpublished Ph.D. Thesis, *University of Western Ontario, Ontario, Canada, 176p.*

Chapter 2:
The Rotating Polarizer Stage

Introduction

With a petrographic microscope, a thin section may be viewed in either plane polarized or cross polarized light. Using cross polarized light, some mineral grains will exhibit interference colours similar to those of their neighbours at certain orientations relative to the planes of polarization, making the boundary between them difficult to observe. Consequently, the thin section must be rotated relative to the planes of polarization to clearly define all mineral grains present. Traditionally, this has been accomplished by rotating the thin section while the polarizers remain fixed (Nesse 1991; Starkey and Samantaray 1993; Samantaray 1993). However, for computer-based microscopy, this method would be quite difficult to implement since each pixel in the current image would correspond to a different part of the thin section than it did in the previous image. Starkey and Samantaray (1993) found that keeping the thin section in a fixed position while manually rotating the polarizers would allow the pixels in each sequential image to remain registered.

The idea of rotating the polarizers while the thin section remains fixed was advanced by the design of the computer controlled Rotating Polarizer Stage (Fueten 1997). The Rotating Polarizer Stage attaches directly to the stage of a petrographic microscope and replaces the fixed polarizer and analyzer of the microscope. This allows for computerized control of the sampling process. By automatically rotating it's polarizer and analyzer together, after each incremental image has been captured and processed, the Rotating Polarizer Stage provides a means to digitize a series of images of a stationary thin section.

This is faster and more accurate than rotating the polarizers manually, allowing for quicker sampling and improved data gathering possibilities.

Design of the Rotating Polarizer Stage

The Rotating Polarizer Stage is designed to replace the polarizer and analyzer of the standard petrographic microscope (Figure 2.1). The stage's polarizer and analyzer are each placed inside a gear with each gear connected to a stepper motor by a notched belt. Gearing for the analyzer is identical to that of the polarizer, ensuring that both the polarizer and analyzer rotate synchronously. The stepper motors rotate the gears, while the notched belt assures that no slippage can occur. Each step of a motor induces a 0.9^0 rotation of the corresponding polarizing filter. Therefore, a 180^0 rotation of the polarizers requires the motors to step 200 times.

The stage provides equivalent functionality to the polarizer and analyzer present on a standard petrographic microscope. The stage has the ability to switch from cross to plane polarized light, the polarization directions of the polarizer and analyzer are discernible and the polarizers remain crossed during analysis. The Rotating Polarizer Stage is placed directly on the stage of petrographic microscope, or macroscope, provided the standard polarizers built into the microscope, or macroscope, can be removed from the light path.

In addition to the two rotating polarizers, the Rotating Polarizer Stage also contains a neutral density filter and a fixed polarizing filter. These are housed in the upper assembly of the stage along with the upper rotating polarizer. The

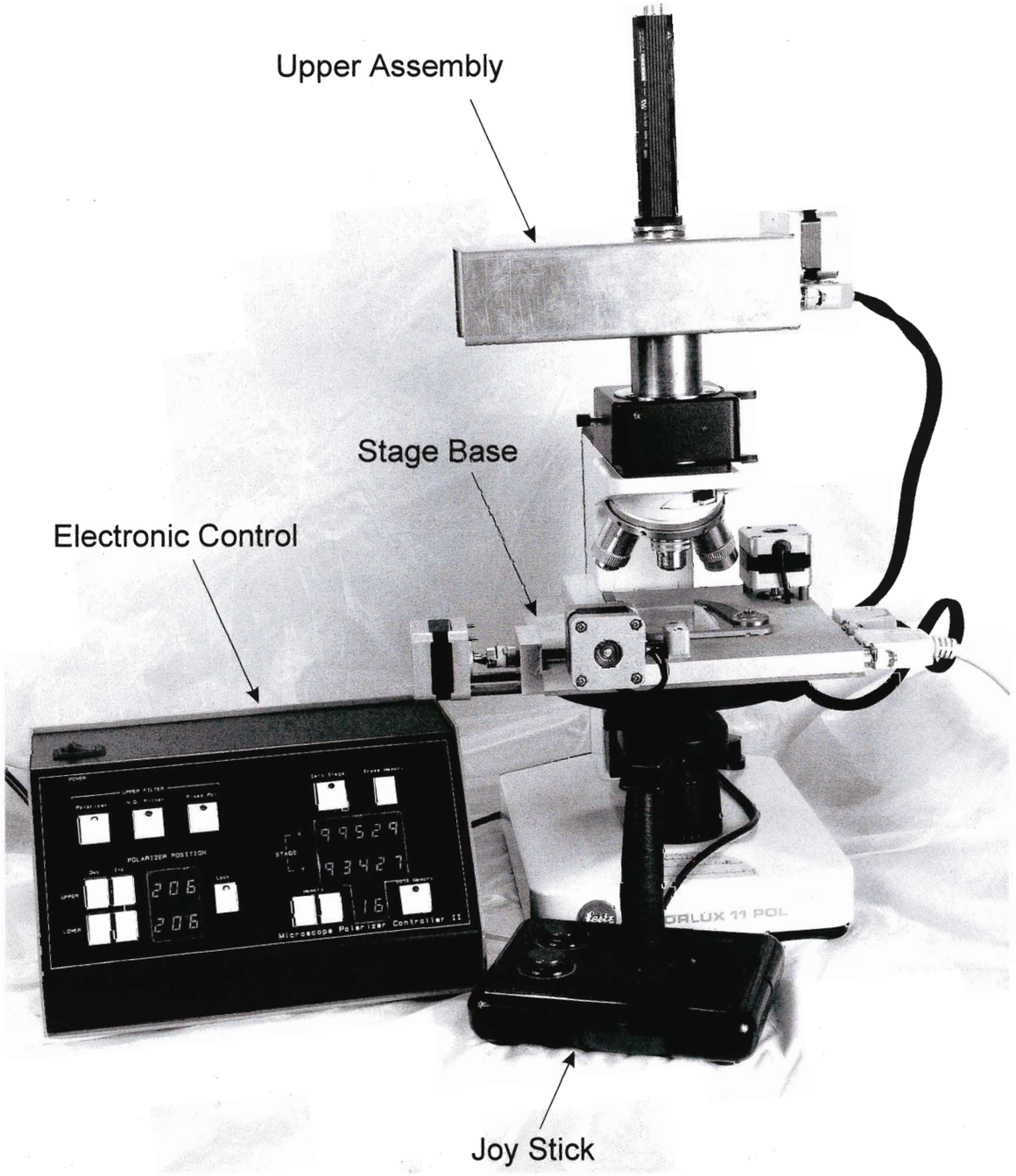
Upper Assembly
Stage Base
Electronic Control
Joy Stick
Microscope Polarizer Controller II

neutral density filter is used for observations made in plane polarized light and the fixed polarizing filter is used for aligning the rotating polarizers. Thin sections are placed in a sample holder between the lower polarizer and the upper assembly. The stage base can accommodate thin sections of various sizes and is equipped with an x/y controller that allows for movement of the sample in the light path. The x/y controller enables an observer to examine the complete thin section by moving it in the light path with a joystick.

The Rotating Polarizer Stage is controlled by specifically designed electronics which communicate with the computer through the serial port. A simple command language directs the movement of the filters housed in the upper assembly to any desired position, rotates either or both polarizers any number of steps in either direction and is capable of moving the x/y controller.

Stage Function

The electronics retain no record of the position of the polarizing filters or the upper assembly when it is turned off. On the initial powering up of the automated stage, the controller moves the filter carriage in the upper assembly laterally, until a microswitch in the filter carriage senses the corresponding wall of the upper assembly. This ensures that the upper assembly is placed into a known position. For most sampling situations, it is desirable to have the rotating polarizers crossed. The rotating polarizers remain crossed by simply rotating synchronously, even if plane light is used and the upper polarizer is out of the light path. A simple procedure is employed to cross the polarizers. Initially, an image is captured

without a sample inserted in the light path. The brightness of the image is calculated by summing the red, green and blue values for the pixels within the image. The upper polarizer is then rotated by a fixed number of steps in one direction, another image is captured and its brightness compared to the first image. If the second image is not brighter than the first, the upper polarizer is again rotated in the same direction, by the same number of steps. If the second image is brighter than the first one, the direction of rotation of the upper polarizer is reversed and the number of steps rotated is reduced. This procedure is followed until the brightness is minimized indicating the rotating polarizers are crossed.

Once the polarizers have been crossed, it may be desirable to align the polarization directions to a known orientation. To accomplish this, the fixed polarizing filter on the upper assembly is moved into the light path. The preferred vibration direction of this fixed polarizer is parallel to the y direction of the thin section. To align the bottom polarizer to the x direction of the thin section and hence perpendicular to the polarization direction of the fixed filter, the brightness minimization procedure described above is run with the exception that both polarizers are rotated synchronously to keep them crossed. After the polarizers have been crossed and aligned, a computer program keeps track of the position of the polarizers with respect to the axes of the thin section.

Light Source Considerations

Caution must be taken when selecting a microscope, or macroscope, to perform petrographic *c*-axis measurements using the Rotating Polarizer Stage. Since the Rotating Polarizer Stage rotates its polarizers while the thin section remains fixed, any polarization of the light source will cause biases in the data collected. With a partially polarized light source, as the preferred direction of the lower polarizer aligns with the preferred direction of the light source, a maximum transmission through the lower polarizer will occur. Similarly, when the preferred direction of the lower polarizer is at 90^0 to the preferred direction of the light source a minimum transmission through the lower polarizer will occur. This effect will cause errors when making *c*-axes measurements on quartz grains in a thin section.

The Image Set

The data collected using the Rotating Polarizer Stage are tailored to the specific image processing applications of this thesis. These include classifying different mineral grain species and measuring grain size, shape and partial crystallographic orientation. Each captured image (Figure 2.2a) requires approximately 1 Mb of storage space, hence a complete set of images representing a 180^0 rotation of the polarizers under conditions of both plane and cross polarized light would require about 400 Mb of storage space (the thin sections used in this study contain quartz and are all sampled through 180^0 to allow for quartz c-axes measurements (Chapter 5)). To reduce the

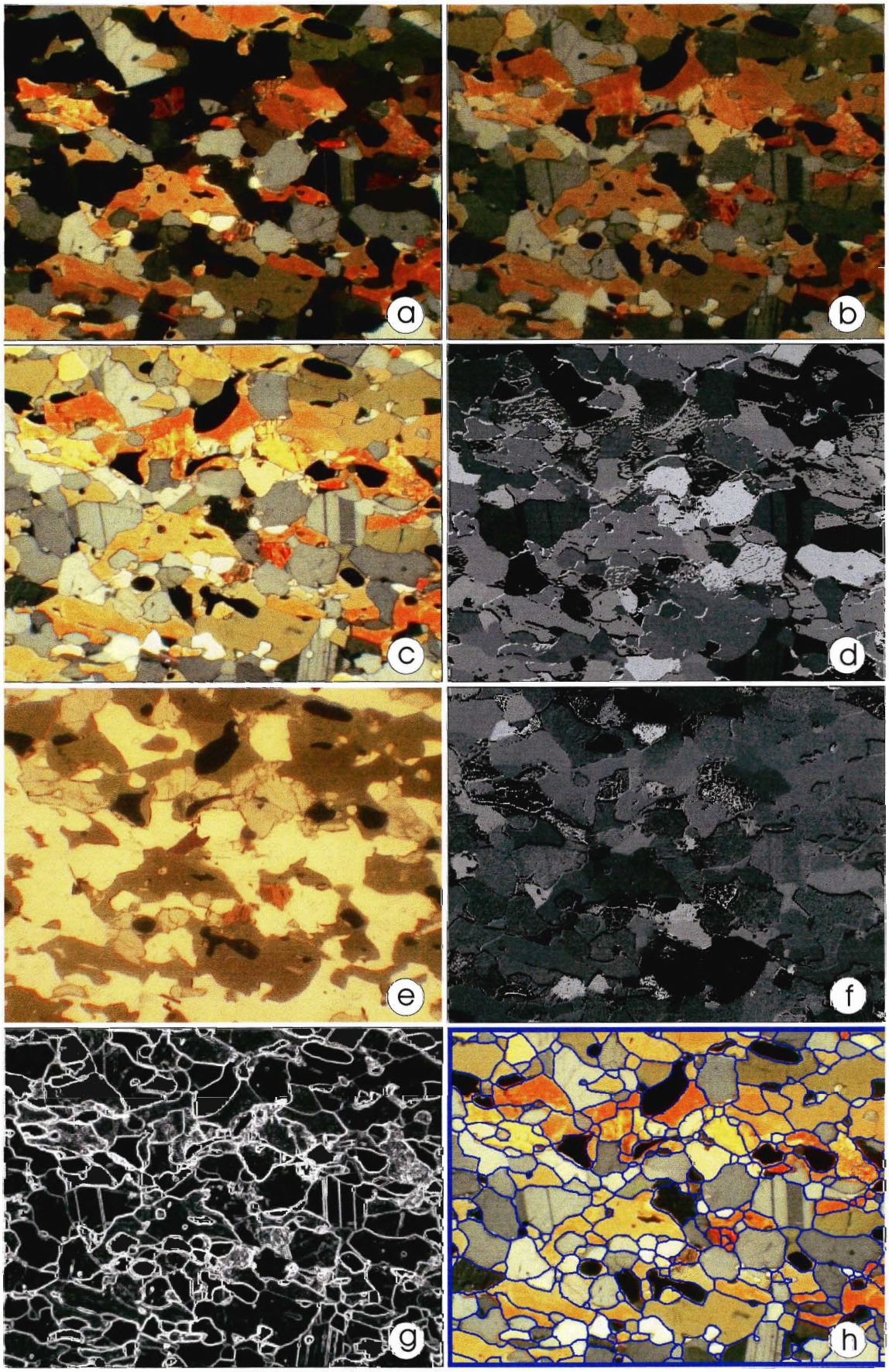
a
b
c
d
e
f
g
h

storage requirements, a series of composite data sets are constructed which each contain selected information obtained during the sampling process of rotating the polarizers through 180^0, first under cross polarized, then plane polarized light. These composite data sets can be viewed as images of the thin section after sampling is complete (Figure 2.2b-g). Combining data from sequentially captured images of a thin section is possible since each pixel remains registered to the same point within a stationary mineral grain for all polarizer orientations.

Sampling Using Crossed Polarized Light

The four composite images compiled when sampling using cross polarized light are the average intensity image, the maximum intensity image, the maximum position image and the gradient image (Figure 2.2b, c, d, g).

The Average Intensity Image

The average intensity image is created using the average red, green and blue component for each pixel during the rotation of the polarizers (Figure 2.2b). It is computed using

$$red = \frac{1}{n}\sum_{i=1}^{n} red_i \qquad (2.1a)$$

$$green = \frac{1}{n}\sum_{i=1}^{n} green_i \qquad (2.1b)$$

$$blue = \frac{1}{n}\sum_{i=1}^{n} blue_i \qquad (2.1c)$$

where n is the number of images obtained in the sampling process. The advantage of this image is that it averages data between minimum (extinction) and maximum (maximum birefringence) intensity.

The Maximum Intensity Image

The maximum intensity image is created by storing, for each pixel in the image, the maximum interference colour (intensity) obtained in a 180^0 rotation of the polarizers (Figure 2.2c). The intensity of a pixel is calculated using the intensity measure in HSI (Hue, Saturation, Intensity) colour space (Gonzalez and Woods 1992) where intensity is defined as:

$$I = \frac{red + green + blue}{3} \qquad (2.2).$$

The maximum intensity image is used in the determination of partial crystallographic orientations of quartz grains as well as in the classification of different mineral species within a thin section.

The Maximum Position Image

The maximum position image is created by storing, for each pixel in the image, the polarizer position, relative to the starting position, where each pixel reached its maximum intensity (Figure 2.2d). For a 180^0 rotation of the polarizers, position values have a range of 0-200, as a pixel can reach its maximum intensity at any one of the 201 steps. The maximum position value is inserted into all three channels making up the image (red, green and blue) producing a grey-scale (8 bit) image. The maximum position image is used along

with the maximum intensity image in determining the partial crystallographic orientation of quartz grains within a thin section.

The Gradient Image

The gradient image is created by passing a gradient operator (Appendix I) which compares the intensity value of a pixel with that of its immediate neighbours in the directions of increasing x and y, across each sequential image (Figure 2.2g). For each pixel, the larger of the gradient values measured is added to an array element representing that pixel. A complete gradient array is built up by the addition of the sequential gradient values while the polarizers are rotated through 180^0. Once the sampling process is complete, the gradient array is scaled to an 8 bit range, with values confined to 0 - 255. In the gradient image the high/bright areas represent the grain boundaries while the low/dark areas represent interiors of mineral grains. A complete set of closed boundaries can be obtained from the gradient image by applying a series of image processing routines.

Sampling using Plane Polarized Light

For sampling under plane polarized light the upper polarizer is moved out of the light path and the neutral density filter is inserted. The neutral density filter serves to compensate for the increase in light intensity reaching the camera without manually adjusting the light source. The two composite images compiled, when sampling using plane polarized light, are the minimum intensity image and

the minimum position image (Figure 2.2e, f). The procedures for obtaining these images are similar to the methods described above except that the minimum intensity of each pixel and it's corresponding polarizer position are stored.

References

Fueten, F., (1997). A computer controlled rotating polarizer stage for the petrographic microscope. *Computers & Geosciences* **Vol. 23**, p.203-208.

Gonzalez, R.C. and Woods, R.E. (1992). Digital Image Processing: *Addison-Wesley, 716 p.*

Nesse, W. D. (1991). Introduction to Optical Mineralogy. *Oxford University Press, New York, 335p.*

Samantaray, A.K., (1993). Computer-assisted Petrographic image analysis and quantization of Rock Textures: unpublished Ph.D. Thesis, *University of Western Ontario, Ontario, Canada, 176p.*

Starkey, J. and Samantary, A.K., (1993). Edge detection in petrographic images: *Journal of Microscopy*, **Vol. 172**, p.263-266.

Chapter 3:
Edge Detection In Petrographic Images Using The Rotating Polarizer Stage

Abstract: Grain boundaries within petrographic thin sections have traditionally been detected using a Canny or Sobel edge detector on a single image of a thin section. Unfortunately, these routines leave gaps within the detected set of edges. Applying a Canny edge detector to several separate images, and adding the results together, produces a somewhat better solution but is computationally expensive. Using the Rotating Polarizer Stage, grain boundaries are obtained by minimizing the computation for each incremental image and performing complex calculations on one final image.

A gradient operator, which compares the intensity value of a pixel with that of its neighbours in both the positive x and y directions is passed over each incremental image. For each pixel, the maximum gradient is recorded in an incremental gradient array. A complete gradient array is built up by the addition of incremental gradient values while the polarizers are rotated through 180^0. Following the acquisition of a complete data set, the total gradient array is scaled to an 8-bit range, with values falling between 0 and 255. This image can be viewed as a gray-scale image with high/bright values representing grain boundaries while low/dark areas form the interior of grains. Using a modified Canny algorithm, the gray-level image is manipulated to produce a binary image containing only edges and interiors. This binary image is a very good approximation of the grain boundaries present in the viewed area of a thin section.

Introduction

One of the earliest goals of petrographic image analysis is the segmentation of the image of a thin section into its constituent mineral grains (Fabbri 1984; Allard and Benn 1989; Simigian and Starkey 1989). This has been accomplished either by using a digitizing tablet to trace the outline of individual mineral grains on a photograph or slab (Fabbri 1984; Simigian and Starkey 1989), or by the use of image processing techniques on captured image(s) of a thin section (Starkey and Samantaray 1993; Samantaray 1993; Lumbreras and Serrat 1996). While using a digitizing tablet is accurate, it is very time consuming and user intensive. Image processing routines offer a quicker and almost as accurate method of grain boundary detection in petrographic images.

This study uses the Rotating Polarizer Stage to acquire data from a thin section (Fueten 1997). The polarizers are rotated through 180^0 with sampling performed at 0.9^0 intervals. For edge detection, the sequential images are operated on individually by passing a simple gradient operator across the image after it has been captured. The resulting edges are accumulated and re-scaled after sampling to create a single image, named the gradient image, which is a composite of the captured and processed individual images. The gradient image is segmented into its constituent mineral grains by applying a sequence of image processing routines to it, which are a modification of those described by Canny, 1986. The resultant extracted edges form closed boundaries around individual mineral grains in the thin section.

Edges in petrographic images

In petrographic images, a grain boundary, or edge, is recognized where there is a distinct change in image intensity between two regions (Marr and Hildreth 1980; Gonzalez and Woods 1992; Starkey and Samantaray 1993; Parker 1994; Jain *et al.* 1995). The change in image intensity can be modeled as either a step discontinuity or a line discontinuity. With a step discontinuity, image intensity changes abruptly from one level to another (Figure 3.1a). A line discontinuity shows image intensity changing abruptly from one level to another as well, but there is also a return to the original intensity value after a short spatial distance (Figure 3.1b). These hypothetically modeled discontinuities rarely exist in real images because of noise and/or the effect of smoothing

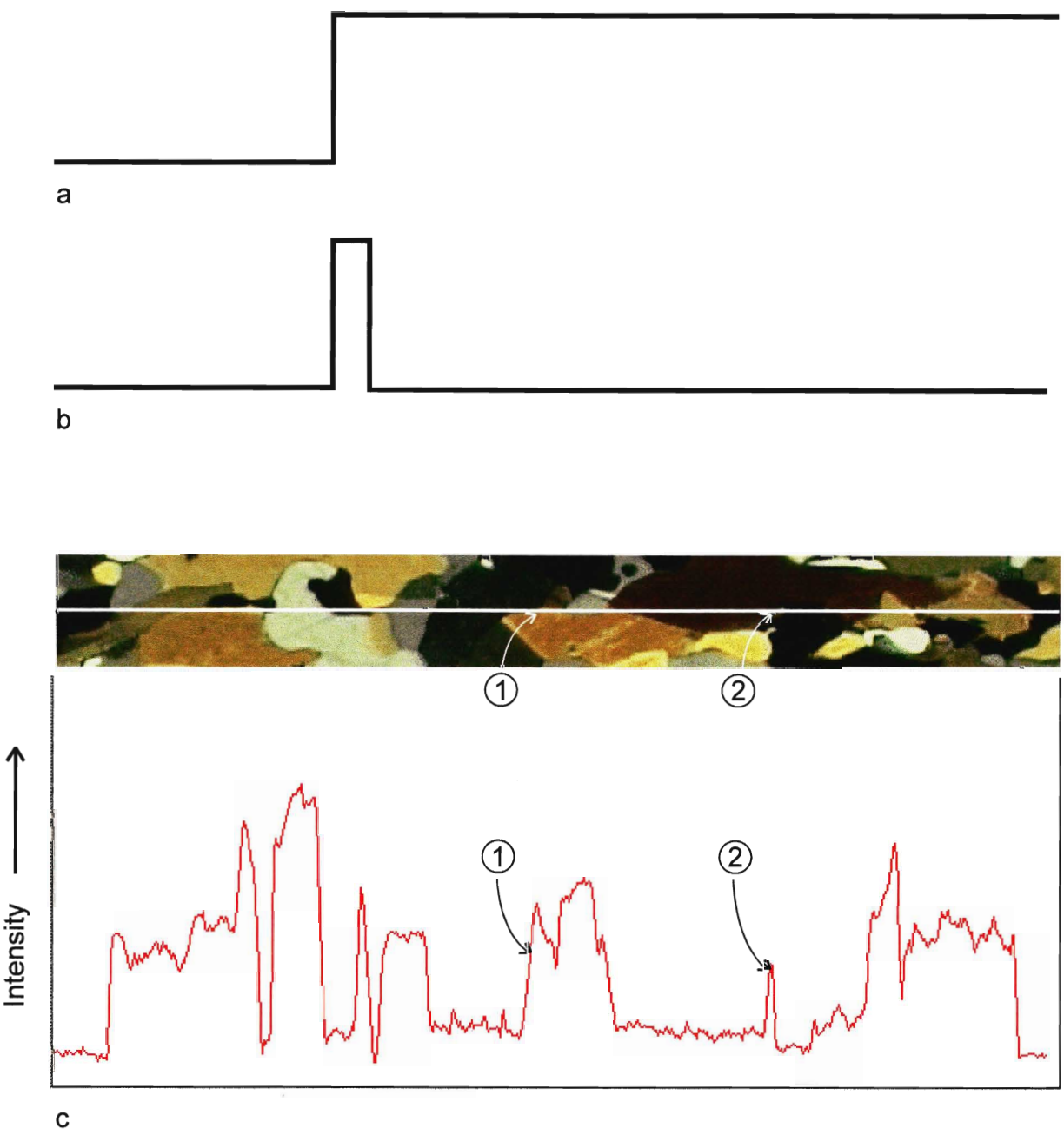
a
b
1
2
Intensity
1
2
c

introduced by most sensing devices (Horn 1986; Jain *et al.* 1995). Where intensity changes in the image occur over a finite distance instead of abruptly, step edges in the image are seen as ramps from one intensity level to another and line edges are seen as peaked roofs between two regions of similar intensity (Figure 3.1c).

The set of edges produced by an edge detector used on a petrographic image can be divided into three different categories (Venkatesh and Kitchen 1992; Jain *et al.* 1995). The first is the set of correct edges. These are the edges that correspond to actual mineral grain boundaries in an image (Edge a in Figure 3.2). The correct edges should form closed boundaries since the features they outline are continuous. In this study, edges that do not form closed boundaries are not considered valid and are removed. The second set of edges is the set of false edges. These are the edges that do not correspond to mineral grain boundaries and are usually caused by the presence of inhomogeneities and/or fractures within grains (Edge b in Figure 3.2). An example of false edges would be twin planes in feldspar grains. The final set of edges is the set of missing edges, which are the grain boundaries that should have been detected but were not. Missing edges usually occur between two mineral grains of the same species, whose crystallographic orientations are similar (Edge c in Figure 3.2).

The Gradient Image

For petrographic images, passing a gradient operator (Appendix I) over a single image will not be sufficient to recognize all grain boundaries present.

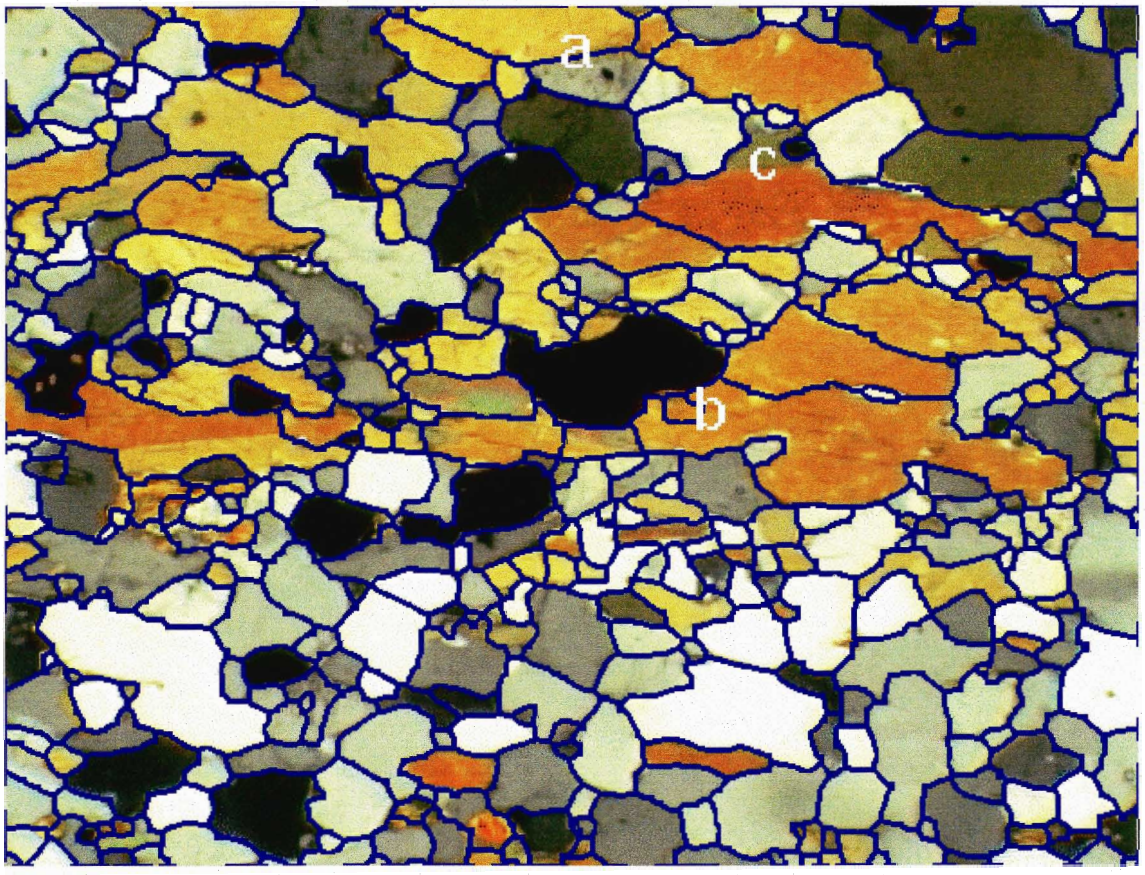
a
c
b

Taking the gradient of several different images, produced by rotating the polarizers relative to the thin section, and combining these results, is an efficient first step in identifying the grain boundaries present in a petrographic image.

The gradient image (Figure 3.3a) is a composite image, produced during the sampling process under conditions of cross polarized light. It is created using equation I.4 (Appendix I) and the discrete approximation to the gradient (Appendix I, equations I.6 and I.7). For each pixel in a captured image, the maximum gradient value is found by comparing the gradient in the x and y directions and adding the greater value to an array element representing that pixel. This is carried out for each sequential image in the sampling process, building up the array of summed gradient values. After sampling is complete, the array of summed gradient values is re-scaled to a range of 0-255 to produce the gradient image.

The gradient image has its highest values corresponding to pixels in the sampled image where the summed gradient was greatest and its lowest values where the summed gradient was least. Generally, the pixels that show the greatest values correspond to the boundaries between mineral grains, while the pixels showing the lower values correspond to the interiors of mineral grains.

Edge Extraction

A simple solution to extracting correct edges from the gradient image is to threshold the gradient image to a level that preserves the higher intensity pixels (i.e., preserves the grain boundaries) and removes the lower intensity pixels (i.e., turns the pixels corresponding to the interior of grains off). However, the pixels that correspond to weak edges in the image are at an intensity level that is close to, or lower than, the intensity level of pixels corresponding to the interior of some grains. This causes the loss of the weaker grain boundaries when thresholding is applied to the gradient image to turn the lower intensity pixels in the image off. A sequence of image processing routines was developed and applied to the gradient image to attempt preservation of both the stronger and weaker boundaries while still turning off pixels in the interior of grains. The method centers on the fact that pixels along both strong and weak grain boundaries will be, locally, at a higher intensity level than the surrounding pixels that correspond to the interior of mineral grains. The sequence of routines designed to exploit this carries out seven separate operations on the gradient image in ten steps. These operations, in order of implementation, are:

1. Gaussian smoothing (Figure 3.3b).
2. Localized enhancement (Figure 3.3c).
3. Gaussian smoothing (Figure 3.3d).
4. Localized enhancement (Figure 3.3e).
5. Nondirectional nonmaxima suppression (Figure 3.3f).
6. Double thresholding (Figure 3.3g).
7. Dilation (Figure 3.3h).
8. Skeletonization (Figure 3.3i).

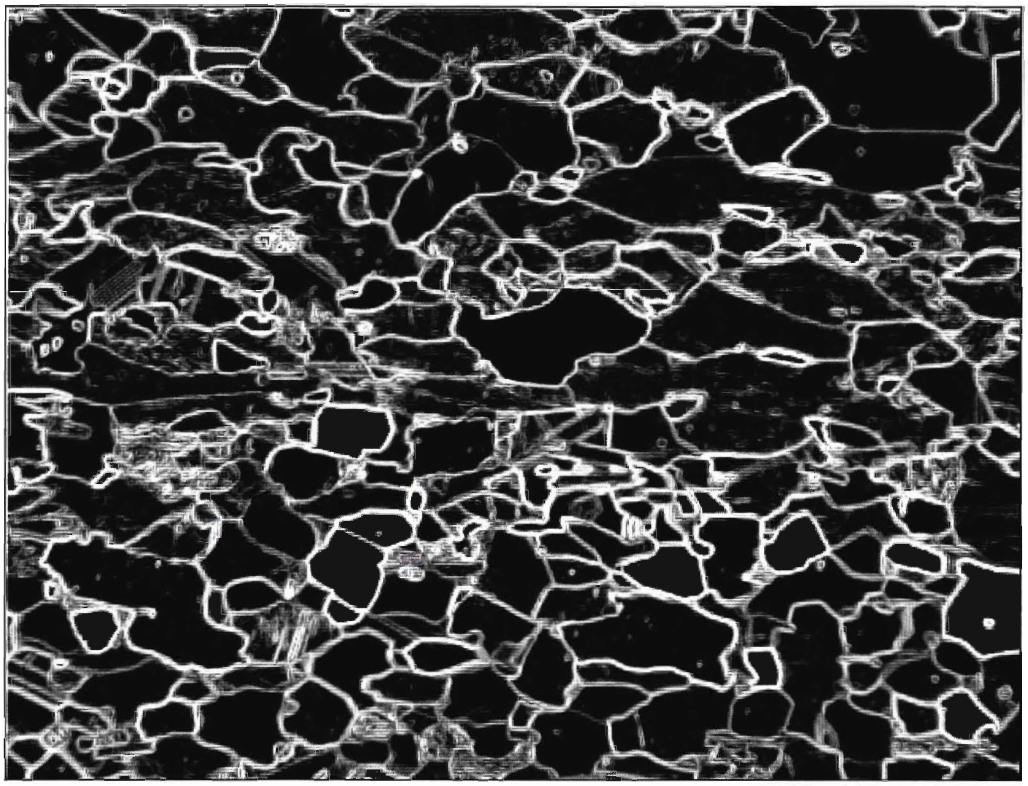

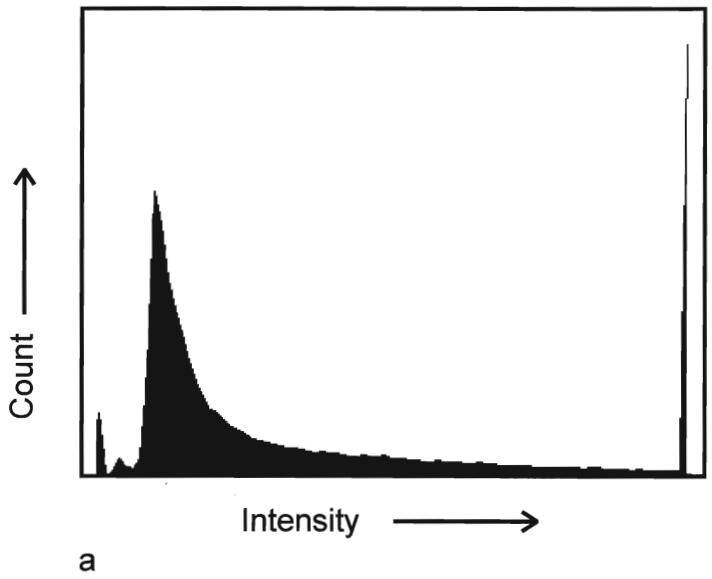

a

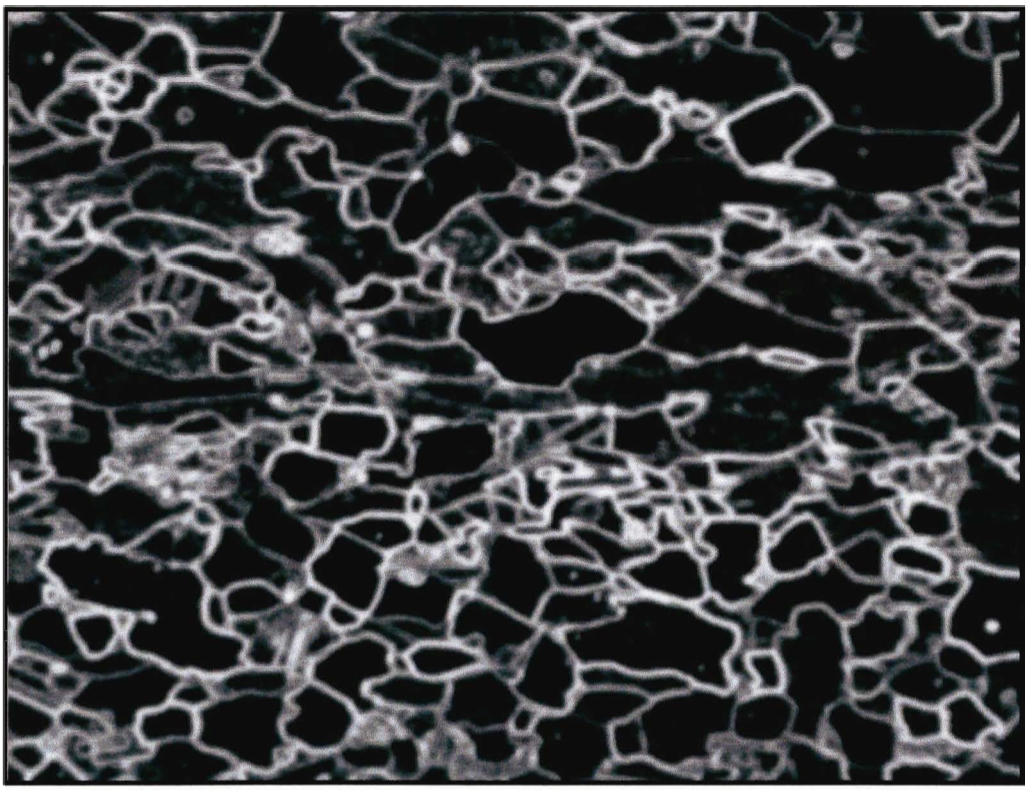

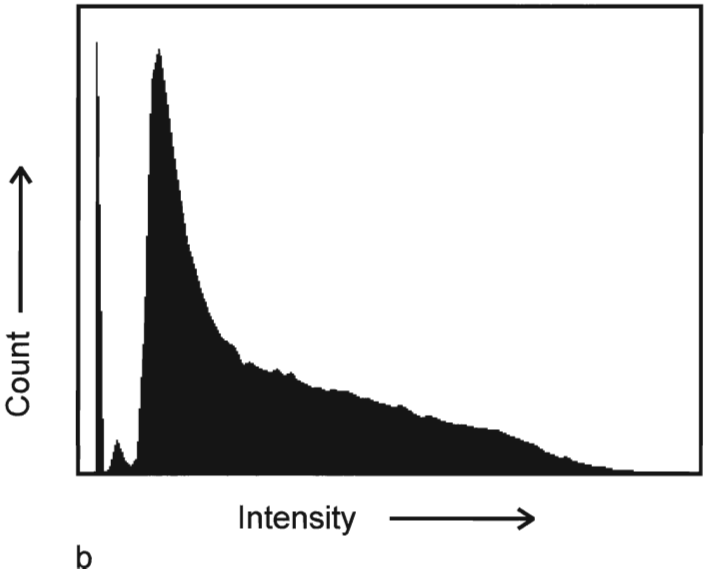

b

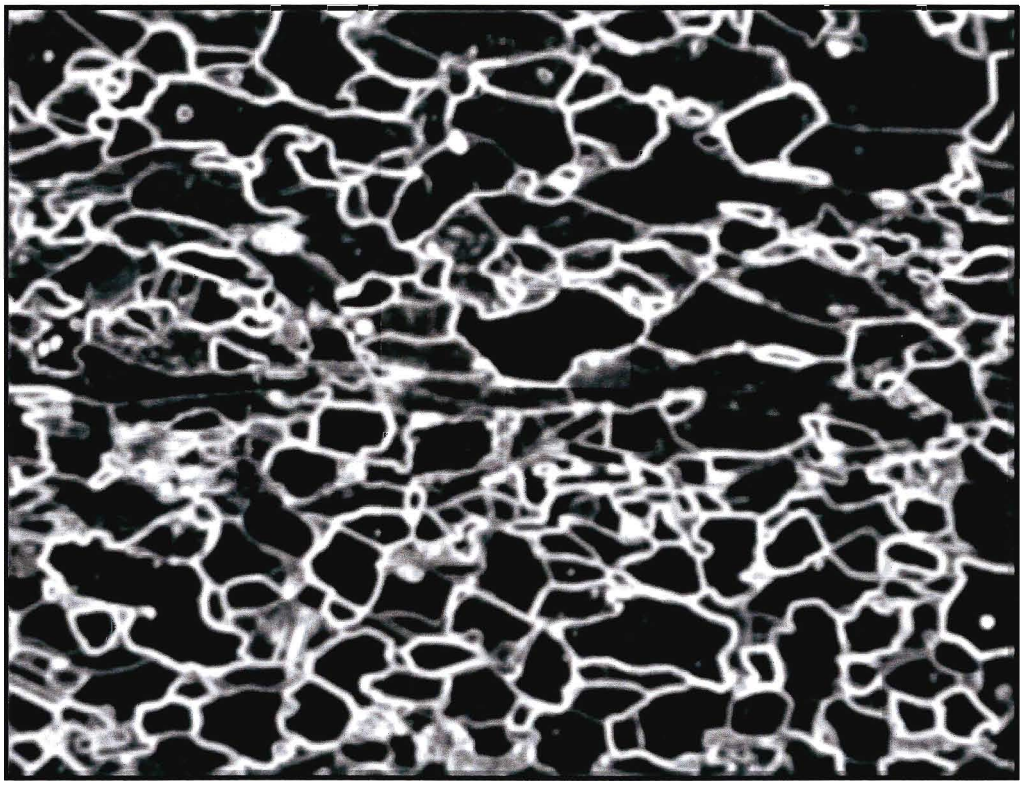

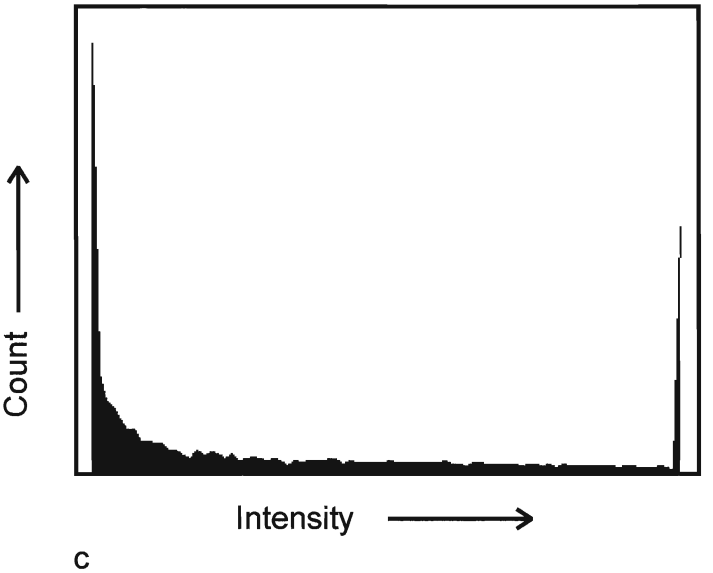

c

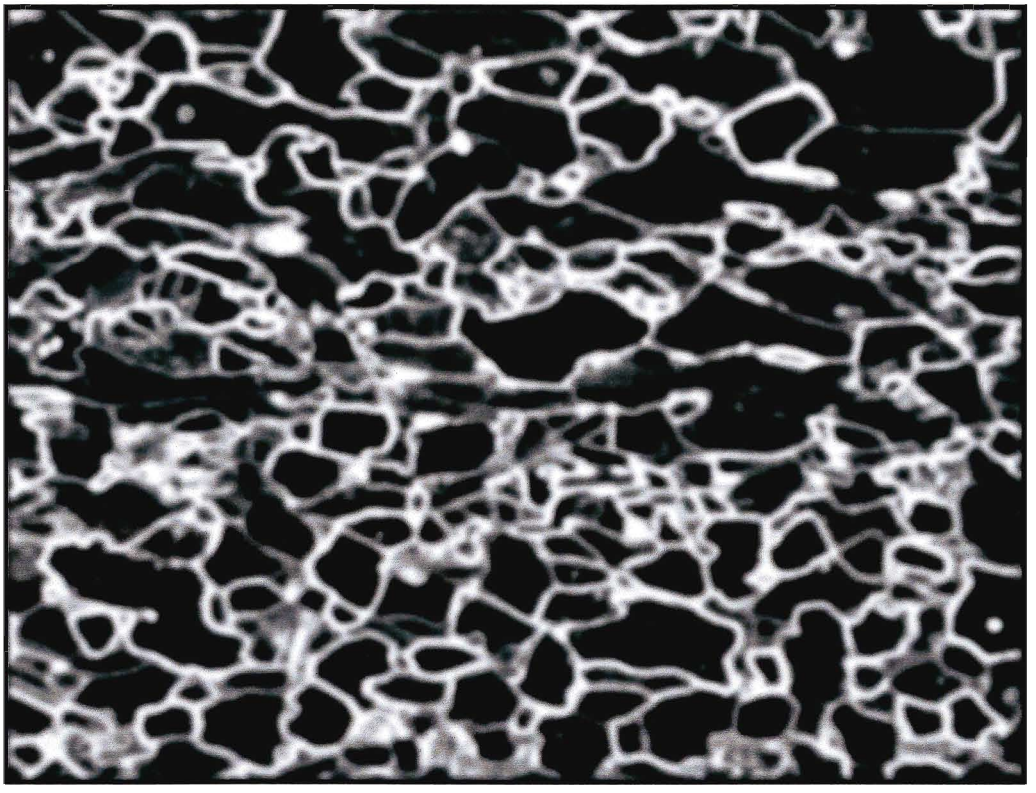

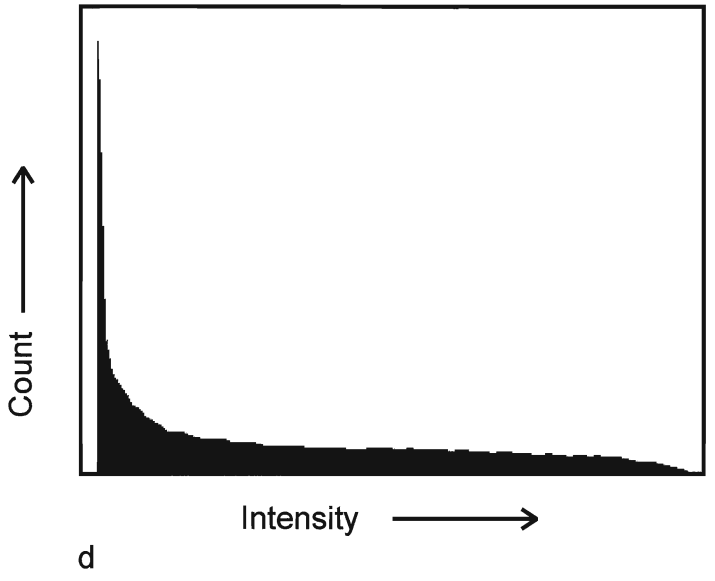

d

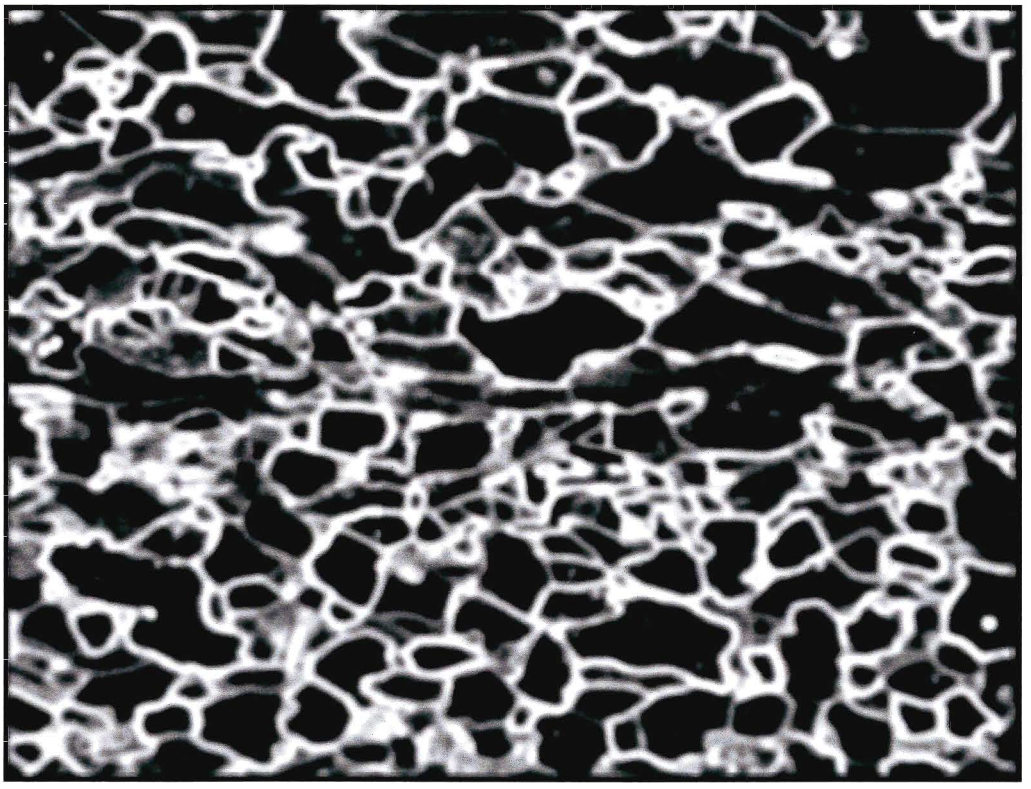

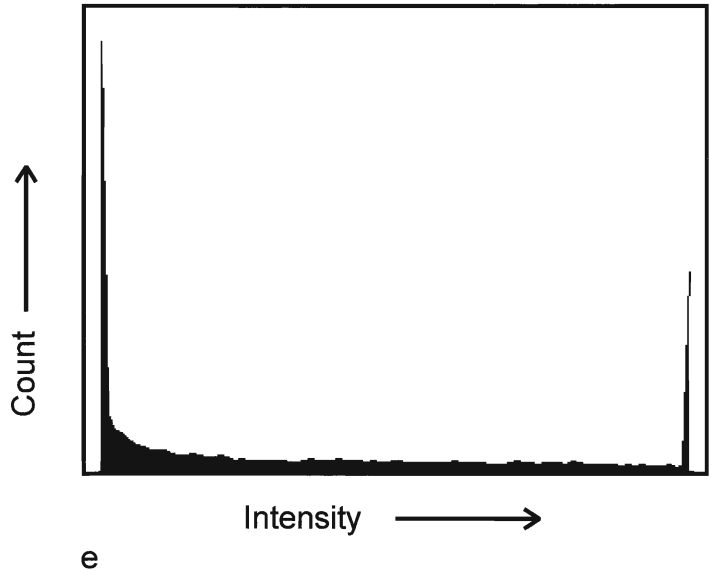

e

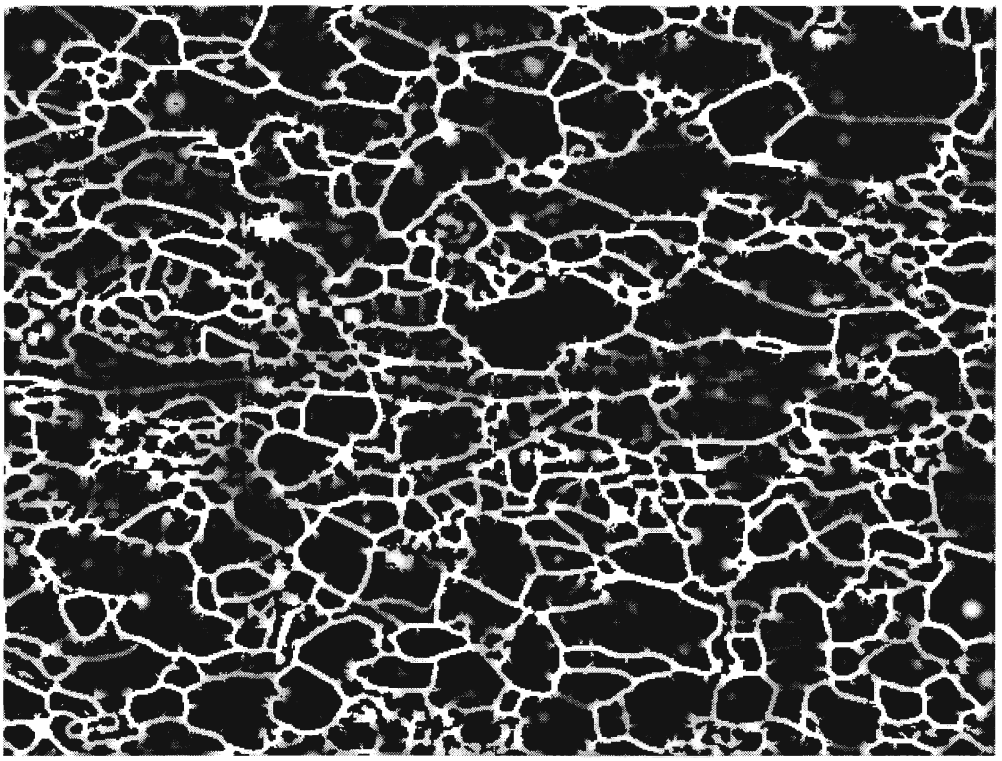

f

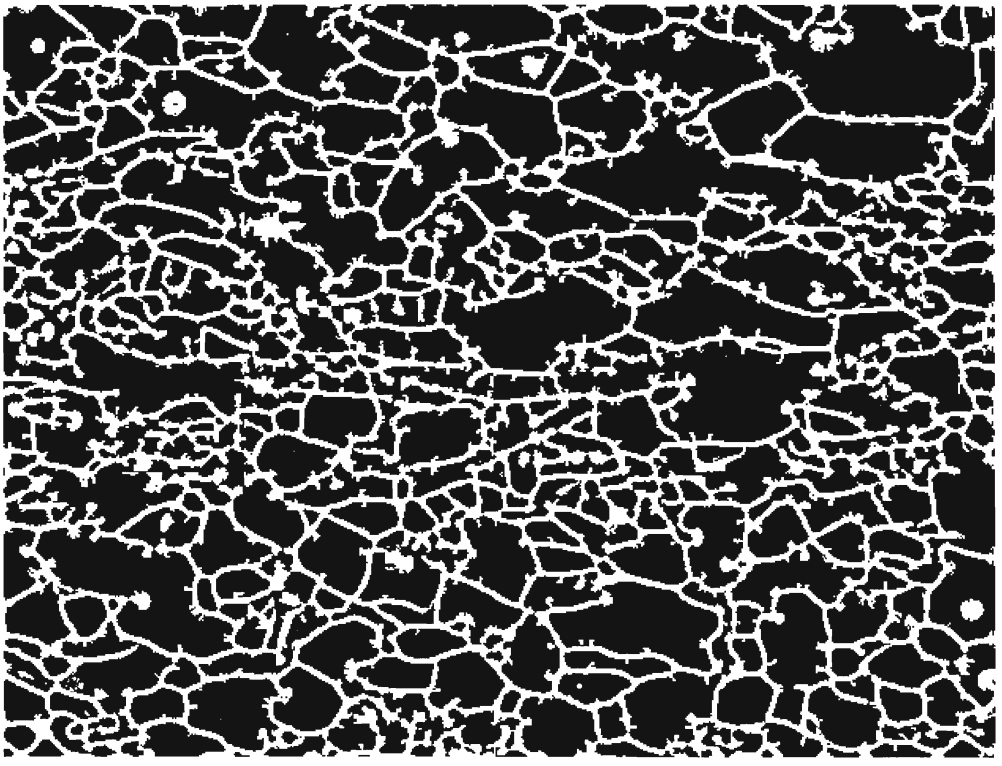

g

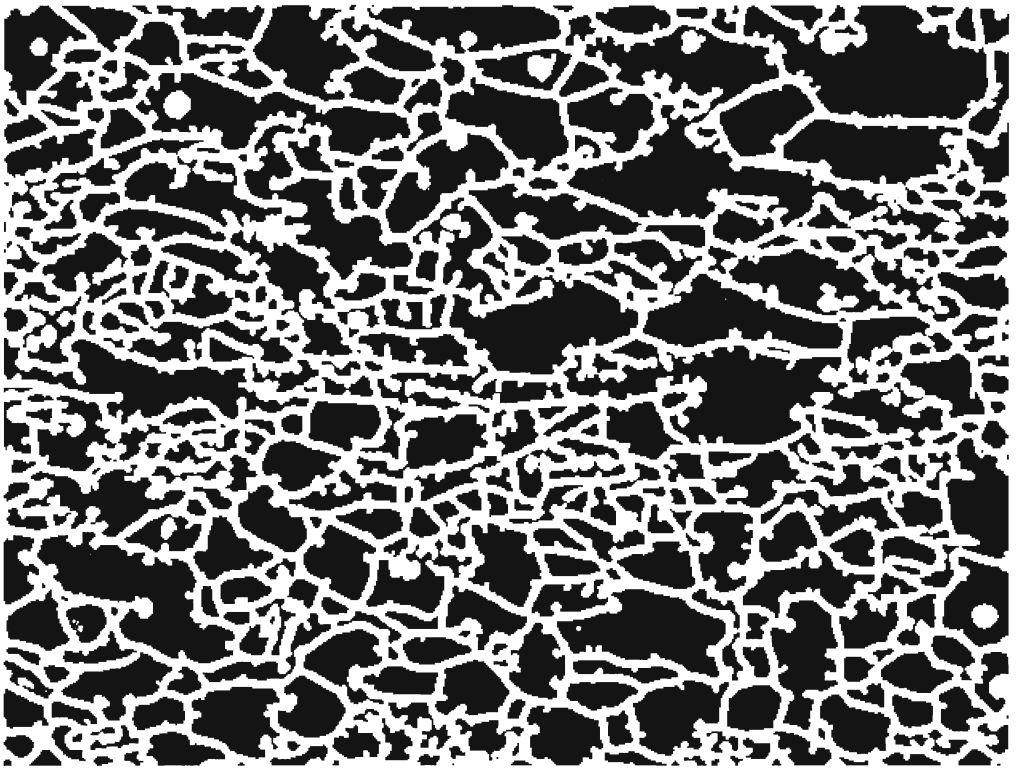

h

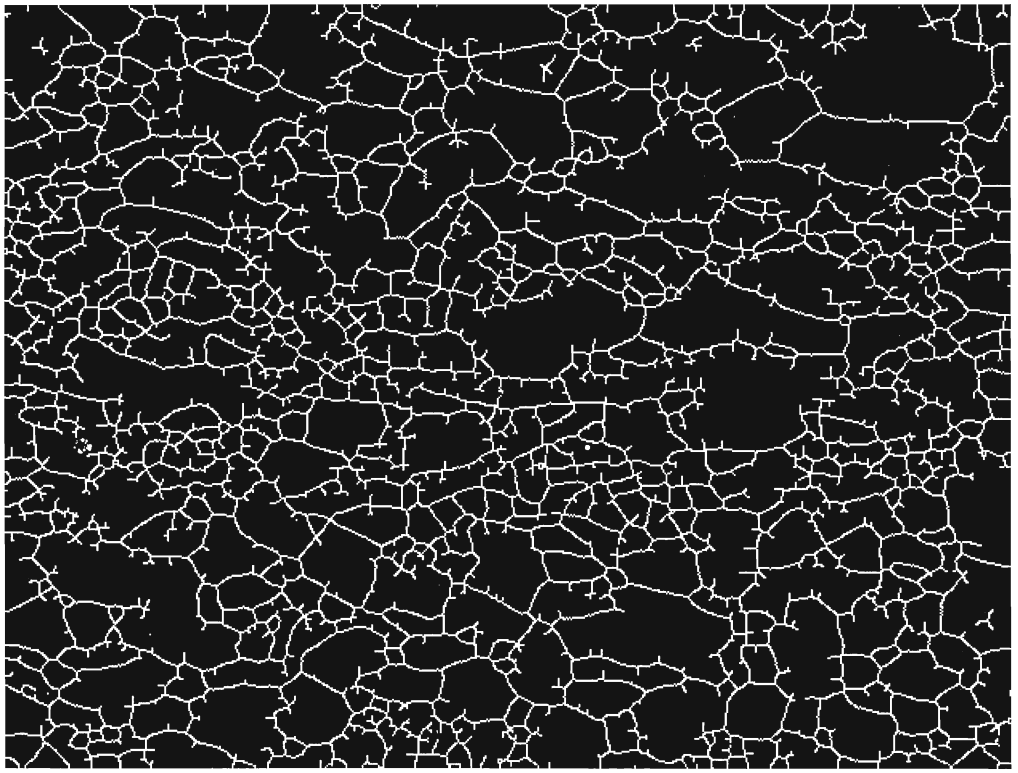

i

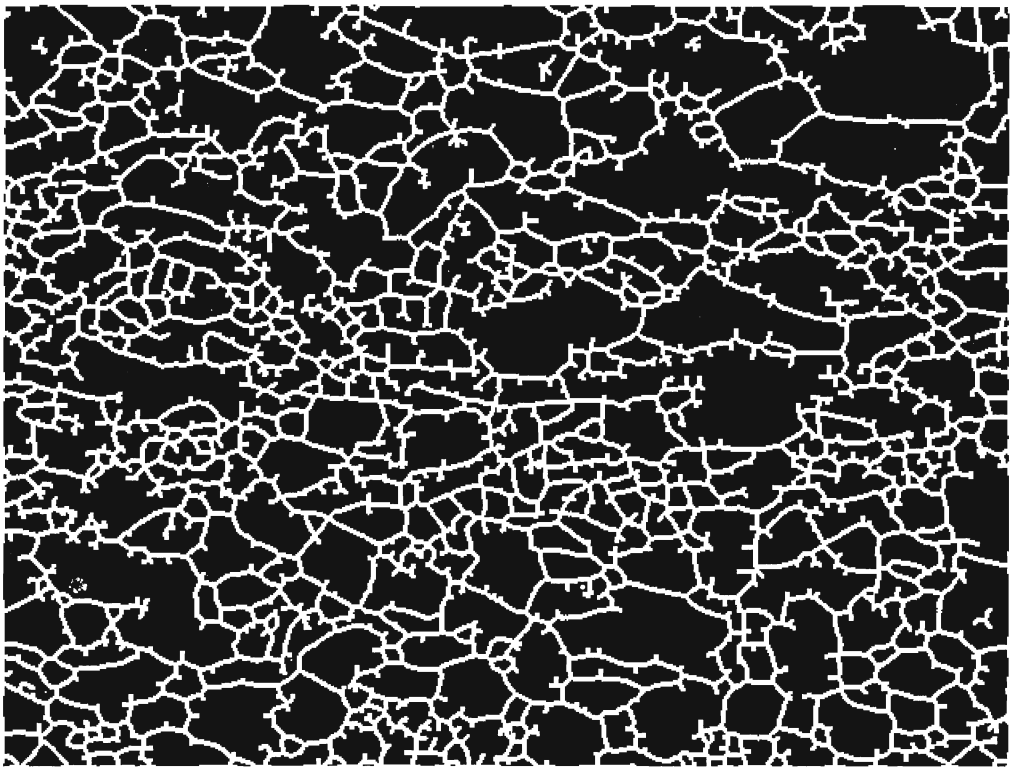

j

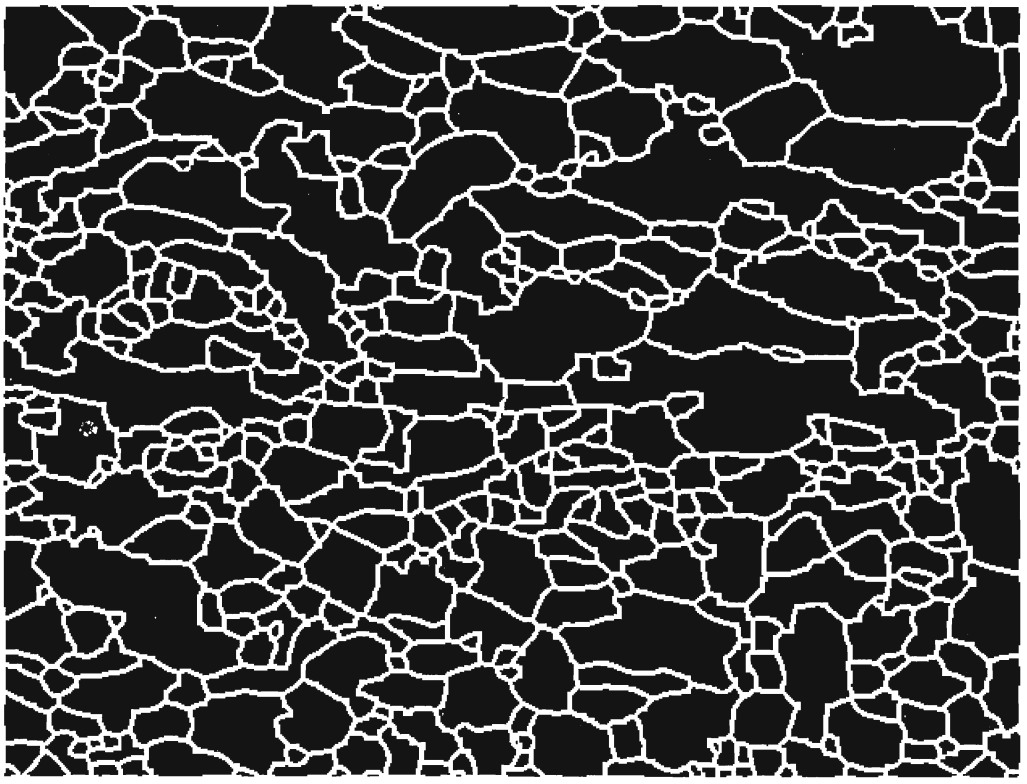

k

9. Dilation (Figure 3.3j).
10. Removal of all unclosed boundaries (Figure 3.3k).

Each of the seven different routines used in edge extraction is described below.

Gaussian smoothing

Gaussian smoothing passes a convolution, with weights chosen according to the shape of a Gaussian curve (Figure 3.4), across an image (Marr and Hildreth 1980; Parker 1994; Jain *et al.* 1995). This flattens and spreads out laterally all features in the image. Gaussian smoothing causes correct edges to become rounded, with smooth sloping sides, and flattens the intensity variations within the interiors of mineral grains.

For the purposes of this study there are two properties of the Gaussian function (Jain *et al.* 1995) that make it a useful smoothing mask. The first is that the Gaussian function is rotationally symmetric. The smoothing performed by the Gaussian convolution will thus be the same in all directions and will not create any biases in smoothing the image. The second property is that the Gaussian function has a single lobe. Due to this, the weights given to neighbours of the central pixel in the convolution (Appendix I) decrease monotonically with distance from the central pixel. This means Gaussian smoothing will not deform the edges in the image by giving more significance to pixels farther away from the pixel of interest.

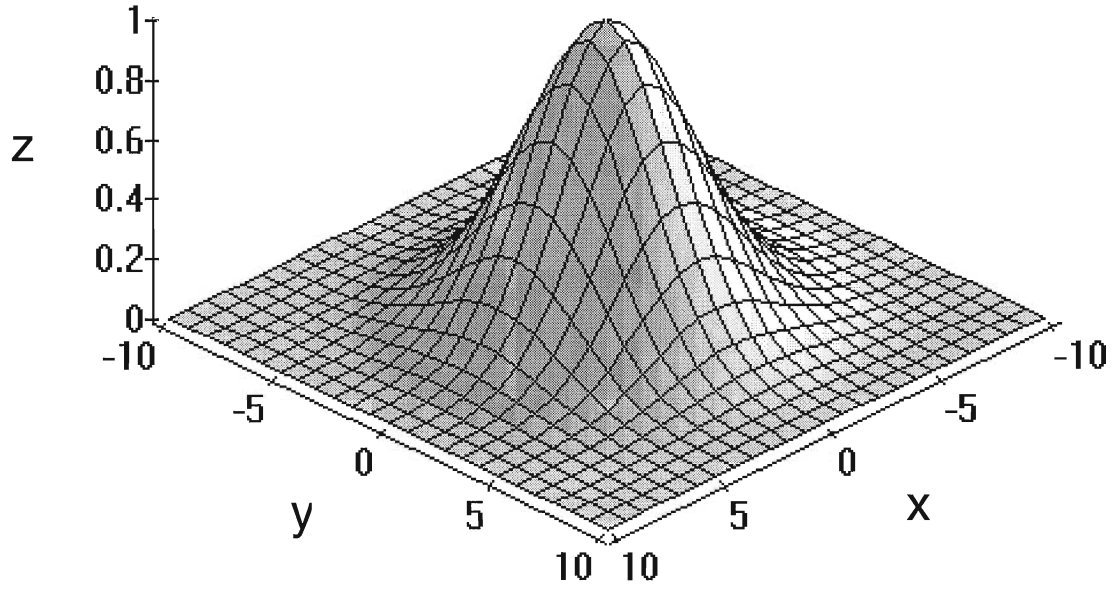
z
1
0.8
0.6
0.4
0.2
0
-10
-5
0
5
10
y
-10
-5
0
5
10
x

Gaussian smoothing is performed by convolving an image with a Gaussian mask. The two dimensional zero-mean discrete Gaussian function is defined as:

$$g[x,y] = c\exp\left(\frac{-(x^2+y^2)}{2\sigma^2}\right) \qquad (3.1) \quad \text{(Jain } et\ al.\text{ 1995)}$$

where σ determines the degree of smoothing applied and c is a normalizing constant. Using equation 3.1, the weights of a 7x7 Gaussian mask, calculated with $\sigma = 1$ (Appendix II), are as follows:

$$\begin{bmatrix} 1 & 1 & 2 & 2 & 2 & 1 & 1 \\ 1 & 2 & 2 & 4 & 2 & 2 & 1 \\ 2 & 2 & 4 & 8 & 4 & 2 & 2 \\ 2 & 4 & 8 & 16 & 8 & 4 & 2 \\ 2 & 2 & 4 & 8 & 4 & 2 & 2 \\ 1 & 2 & 2 & 4 & 2 & 2 & 1 \\ 1 & 1 & 2 & 2 & 2 & 1 & 1 \end{bmatrix} \qquad (3.2)$$

Note that the weights of the Gaussian function sum to 140. For this reason, the derived pixel values must be normalized by 140 when performing the convolution, to ensure that the derived pixel values remain in the range 0-255.

Localized enhancement

Localized enhancement is the operation of re-scaling truncated pixel intensity levels in each area of a sectioned image. Enhancement of the image is used to suppress or remove any pixels from the image that are at a locally low intensity level, while preserving and strengthening pixels that are at a locally higher level. To accomplish this without deleting any weak grain boundaries, the

image is broken-up into a number of smaller rectangular sections. These rectangular sections contain sufficient pixels such that there is a nearly continuous range of intensity levels represented. Each small section can therefore be meaningfully re-scaled, while still protecting weaker edges in the image.

Pixels in the image that are at a locally low intensity level are known as noise pixels. Noise can be defined as the presence of a high gradient at a non-edge location in the image due to impurities and/or inconsistencies within a mineral grain. Breaking the image up into smaller pieces for enhancement greatly reduces the possibility of making comparisons between weak edges and strong noise. Higher intensity noise pixels are normally found near stronger edges while lower intensity noise pixels are normally found near weaker edges. In both cases the noise pixels surrounding the edge pixels are locally at a lower level than the edge pixels themselves.

The first step in localized enhancement is the truncation of the histogram of each region. The 10% of pixels that correspond to the lowest grey levels in each region and the 5% of the pixels that correspond to the highest grey levels in each region are the truncated pixels. The 10% of the pixels corresponding to the lowest grey levels in each region are interpreted to coincide with the interior of mineral grains and as such are arbitrarily assigned a value of 0. The 5% of pixels that correspond to the highest grey levels in each region are interpreted to lie on correct edges in the image and for this reason are assigned a value of 255. The truncation of the histogram creates a new highest grey level and new lowest grey

level to be used in the re-scaling operation. The re-scaling is done linearly, to a range of 0-255 within each rectangular section, for each non-truncated pixel. To re-scale properly, each non-truncated pixel in a region must first have the minimum value in the (truncated) region subtracted from it. This forces the minimum value in the region to be zero. Multiplying by the ratio of desired intensity range to truncated intensity range completes the re-scaling. This is accomplished using the simple formula:

$$new(x,y) = \left(old(x,y) - \min\right)\left[\frac{255-0}{(\max)-(\min)}\right] \qquad (3.3)\ (\text{Parker } 1994)$$

where $new(x,y)$ represents the intensity of the re-scaled pixels, $old(x,y)$ represents the intensity of the truncated pixels prior to re-scaling and max and min are, respectively, the highest and lowest levels in the region after truncation of the histogram.

Nondirectional Nonmaxima Suppression

Nondirectional nonmaxima suppression (NDNMS) is a modification of nonmaxima suppression described by Canny (1986). NDNMS thins an image by finding the locally most intense pixels in the image. It does this by comparing the intensity level of a pixel being examined to the intensity level of pixels in a surrounding square area. If there are more than a certain number of neighbouring pixels at a higher intensity than the central pixel, the central pixel is deleted. If there are less, the central pixel is saved as an edge pixel. The cutoff

number of surrounding pixels, that determines whether or not a pixel is to be deleted, defines the threshold applied.

Since a digital image is represented on a square grid, each pixel in the image has a common boundary with 4 pixels and shares a corner with 4 additional pixels (Figure 3.5). These 8 pixels, collectively, represent the first neighbourhood around a central pixel (Gonzalez and Woods 1992; Parker 1994; Jain *et al.* 1995). Subsequent neighbourhoods are defined by the consecutive layers of pixels, defining successively larger squares, around a central pixel.

The number of neighbourhoods used in NDNMS has a direct effect on the performance of the algorithm. If one or two neighbourhoods are used there are gaps created where weaker edges intersect stronger edges. These gaps are the result of the algorithm determining that the weaker edges are noise adjacent to stronger edges in the image. When NDNMS is applied to the pixels that represent the weaker boundary, at the weak to strong junction, a limited number of neighbourhoods allows the pixels belonging to the strong edge to account for a large portion of the compared pixels. Since these pixels are at a higher intensity level, the threshold is readily reached and the pixels belonging to the weak boundary are marked for deletion. Using a larger number of neighbourhoods increases the number of pixels saved as edge pixels on application of the algorithm. Although this solves the problem of broken boundaries at weak to strong junctions, a larger number of neighbourhoods can also mark too many pixels as edge pixels, introducing many false edges into the complete edge set. Each different number of neighbourhoods will have its own,

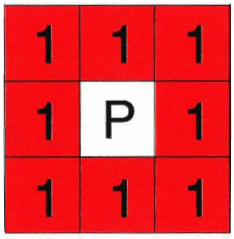
1 1 1
1 P 1
1 1 1

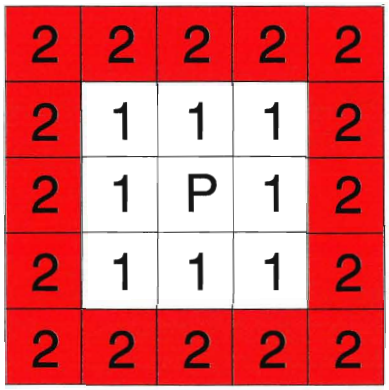
2 2 2 2 2
2 1 1 1 2
2 1 P 1 2
2 1 1 1 2
2 2 2 2 2

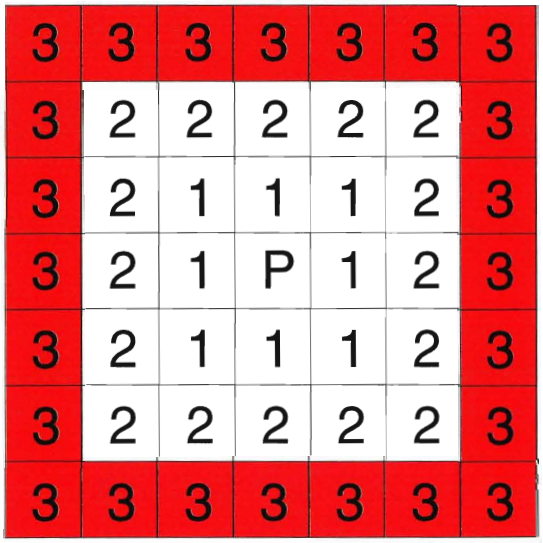
3 3 3 3 3 3 3
3 2 2 2 2 2 3
3 2 1 1 1 2 3
3 2 1 P 1 2 3
3 2 1 1 1 2 3
3 2 2 2 2 2 3
3 3 3 3 3 3 3

experimentally determined, best threshold level for optimal performance. Increasing the threshold level from the optimal value will cause too many pixels to be saved which will contribute to noise in the end. Decreasing the threshold level will remove noise but also remove some weak grain boundaries. The comparison of the different number of neighbourhoods discussed above were performed using the optimal threshold level for each different number of neighbourhoods.

By experimental determination it was found that the optimal number of neighbourhoods to use in NDNMS was 3, at a threshold level of 22. The NDNMS algorithm counts the number of pixels in the first 3 neighbourhoods around a central pixel that are at a higher level than the central pixel. If there are more than 22 at a higher level, the central pixel is marked for deletion. Pixels marked for deletion are not deleted until all pixels in the image, that are on, have had NDNMS applied to them.

Double Thresholding

After NDNMS there are many false edge fragments left in the image among the correct edges. Double thresholding attempts to reduce the number of false edge fragments while linking correct edge fragments (Canny 1986; Jain *et al.* 1995). The double thresholding algorithm applies two thresholds to the image, producing two different thresholded images, I_L (Figure 3.6a) and I_H (Figure 3.6b), with I_H having a higher threshold applied to it than I_L. Since I_H was created using a higher threshold, it will contain fewer false edges than I_L, but I_H will have breaks

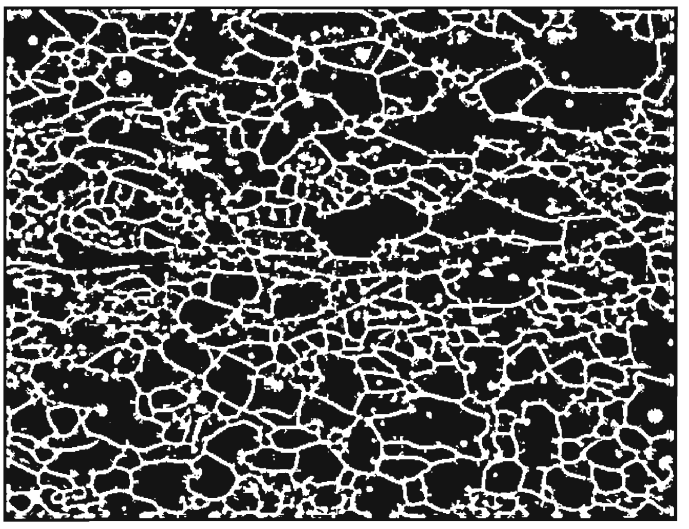

a

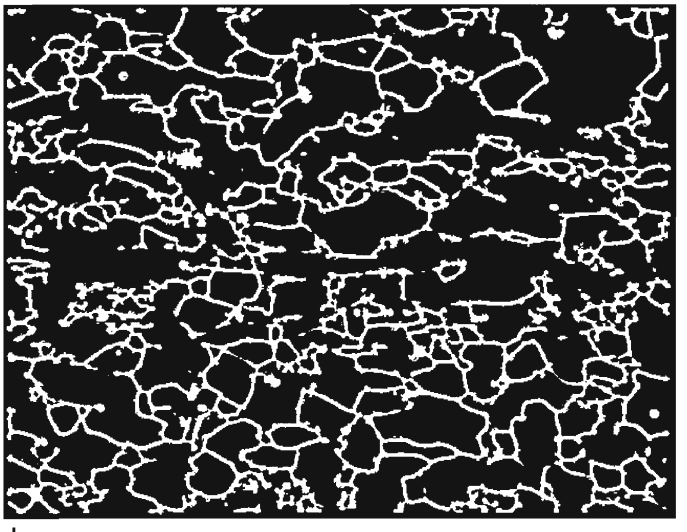

b

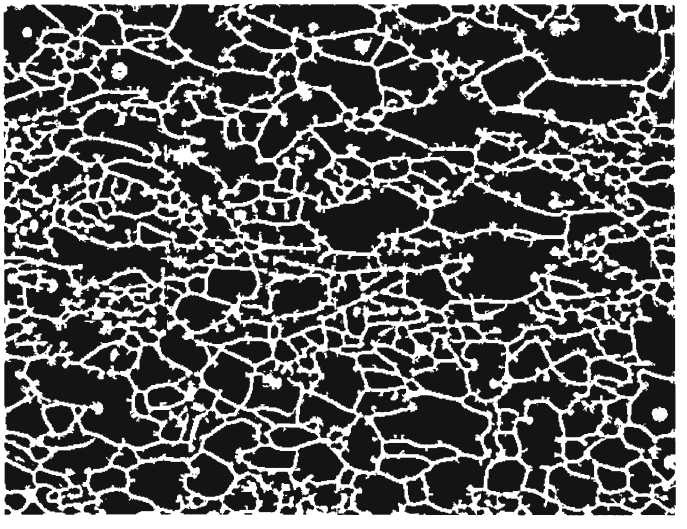

c

(or gaps) in its set of edges. The double thresholding algorithm links the edges in I_H by taking information from I_L whenever it reaches a gap in I_H. At a gap in I_H, the first neighbourhood around the corresponding pixel in I_L is checked for pixels that can be linked to the end of the broken edge in I_H. In this way the image in I_H grows its missing edges from I_L without keeping unwanted edge fragments. After double thresholding, the image is bi-level with the mineral grain boundaries at a grey level of 255 (white) and mineral grain interiors at a grey level of 0 (black).

Dilation

The edge linking provided by the double thresholding algorithm leaves some small gaps present in the set of edges extracted to this point. To close these remaining gaps a dilation routine is applied to the image. The process of dilation adds a new layer of pixels around the boundary of a region. To accomplish this, a structuring element is passed across the image (Fabbri 1984; Gonzalez and Woods 1992; Parker 1994; Jain *et al.* 1995). A structuring element is a mask of a particular shape using multiple pixels. It is passed over the image and is centered on each pixel to be examined. The shape of the structuring element is compared to the shape created by the surrounding pixels in the image that are on. If a match for the shape is not found, surrounding pixels in the image that are off are turned on until the shape of the structuring element is reproduced, creating the dilation.

In this study, a single neighbourhood 'cross' structuring element was used to produce a dilation (Figure 3.7a). This is the first neighbourhood approximation

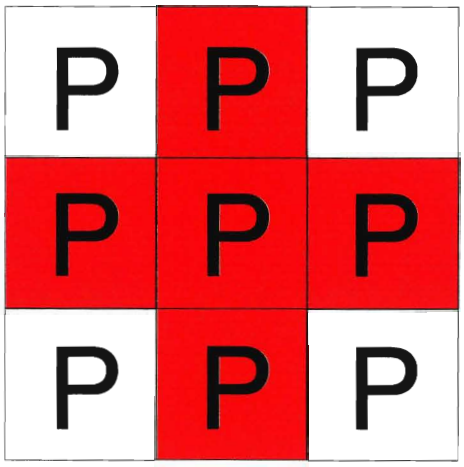

a

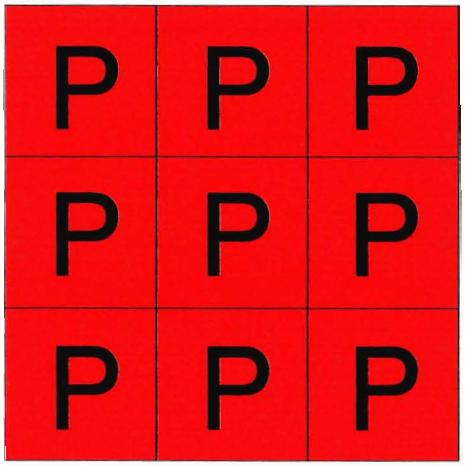

b

of a circle and as such will not tend to add corners, or 'square', the image as a structuring element representing all the pixels in a first neighbourhood would do (Figure 3.7b). The 'cross' structuring element best preserves the original shape of the boundaries after dilation.

On application of the algorithm small gaps in the image are closed as the dilation routine adds thickness to the edges in the image. This adding of pixels is not restricted to gaps in the edges but can occur wherever edge pixels are present in the image (Figure 3.8). The result of this is closed but thicker contours. The thickness added is less than what would be if a 1-neighbourhood square structuring element was used. This is advantageous since adding too much thickness to the edges could close over the interiors of small grains.

Skeletonization

Skeletonization removes extra pixels from an image to produce a simpler image having the same shape and number of regions as the original image. The skeletonized image must have three basic properties, described by Parker (1994):

1. It should consist of thinned regions, 1 pixel wide.
2. The pixels comprising the skeleton should lie near the center of a cross-section of the region.
3. Skeletal pixels must be connected to each other to form the same number of regions as existed in the original image.

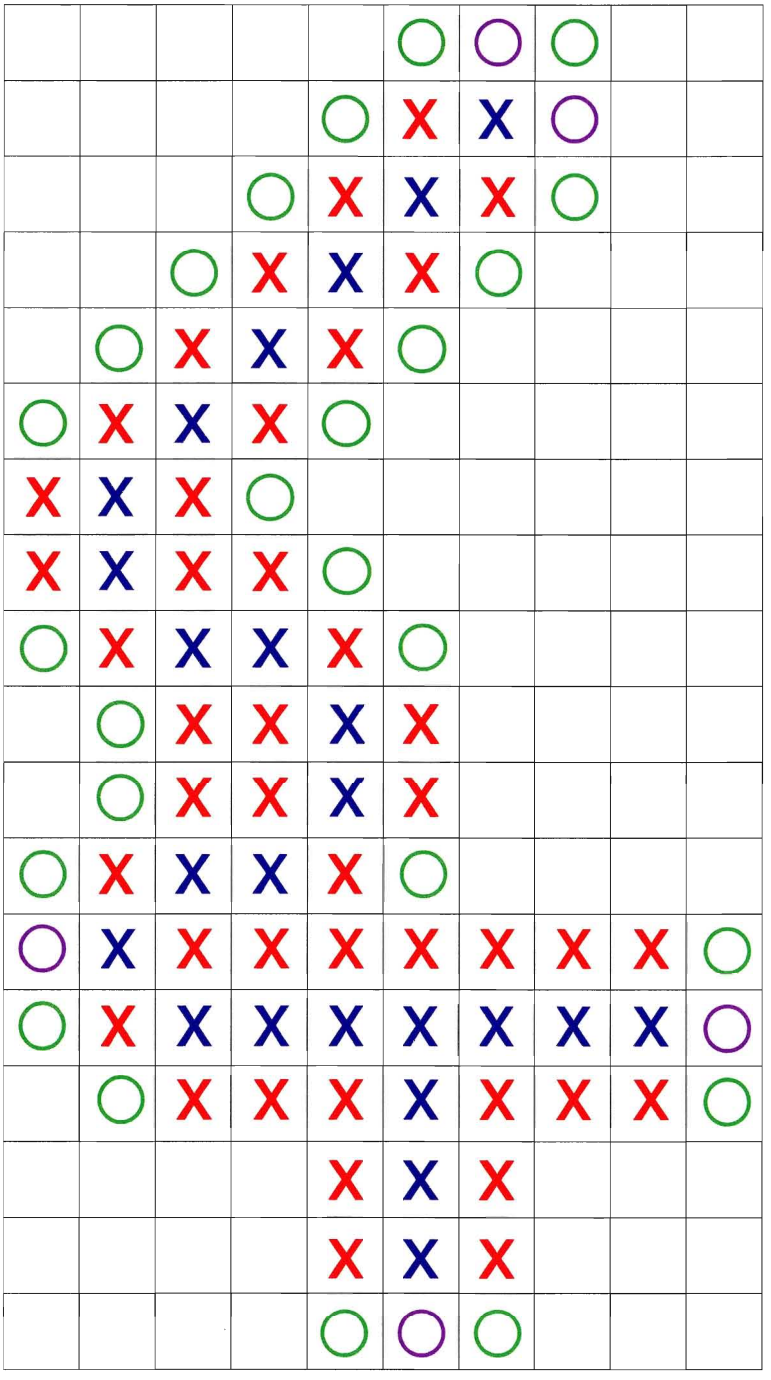

Skeletonizing the image requires two passes over the image each time a layer of pixels is to be removed. The first pass marks pixels which are to be deleted, the second pass actually deletes the marked pixels.

There are three rules that are followed to decide whether or not to mark a pixel for deletion in the first pass across the image (Parker 1994). First, a pixel can be marked for deletion if it has greater than 3 and less than 7 of the pixels in its first neighbourhood on. This ensures that the end points of the skeleton are not eroded away and that pixels are removed from the boundary of the wide edge and not from the inside. Second, a pixel can be marked for deletion if its neighbour directly behind it and its neighbour directly to the left of it have not already been marked for deletion (in a top-bottom, left-right traverse across the image). This rule is applied to ensure that the skeleton of a wide edge is found at the center of the wide edge. Third, a pixel cannot be marked for deletion if it is connected to more than one region. This rule ensures that formerly connected regions in the image remain connected after the skeletonization process is complete.

Removal of Broken Boundaries

The final step in the edge extraction process is to remove all edge fragments that are not part of a closed loop. These dangling edge fragments are almost all relics of noise from within the mineral grains, although a few may be unclosed grain boundaries. The removal of broken boundaries requires that the edges in the image have a width greater than 1 pixel. To accommodate this the

dilation routine is applied to the skeletonized image before the algorithm is applied.

The routine begins by applying a standard recursive fill algorithm to the image (Foley *et al.* 1995). Since, at this point, all mineral grain boundaries are present, the fill algorithm assigns each non-edge pixel to a specific mineral grain number as each individual grain is filled. This information is used to determine the number of mineral grain(s) that bound each edge fragment in the set of edges. If an edge fragment is bounded by pixels from more than one mineral grain, it is kept as a correct edge, as at least two mineral grains are needed to define a correct edge. If however, the edge fragment is bounded by pixels from only one mineral grain, it is not considered to be a correct edge and is deleted.

In order to determine the number of mineral grains that surround each edge fragment, two scans across the image are made. The first is in the x-direction, moving in a left to right traverse across the image. The second scan is in the y-direction, moving in a top to bottom traverse. In both cases, the pixel directly behind each edge pixel (in the direction of traverse) has its grain number compared with the pixel six steps ahead (in the direction of traverse). If the grain numbers are the same, the edge pixel is immediately turned off. If the grain numbers are different, the edge pixel is left on as a true edge.

Following the removal of broken boundaries, the edge extraction procedure is complete. An illustration of the extracted grain boundaries overlain on top of the maximum intensity image is shown in Figure 3.9b.

Discussion

Using the Rotating Polarizer Stage to create the gradient image, and applying the image processing techniques described above, produces a segmented image, containing all the grain boundaries detected in a sequence of captured images (Figure 3.9b). The grain boundaries detected, however, do not all correspond to correct edges in the image. Fractures and twins are prominent features in most thin sections and these, if strong enough, will produce false edges. There are also, in some cases, grain boundaries that go undetected in the edge extracted image. These occur between mineral grains that never show a significant intensity difference throughout a series of captured images. This normally occurs when two adjacent mineral grains are of the same species and have crystallographic orientations that are similar. Manual editing of the edge extracted image in the cases of false and missing edges is necessary to produce the final edge extracted image (Figure 3.9c).

All of the strong and most of the weak correct edges from the gradient image are preserved in the final edge extracted image. The number of false edges present in the final edged image has a direct correspondence to the amount of fracturing and to the number of twinned feldspar grains present in the thin section being examined. The more fractures and twinned grains present, the more false edges are produced. Due to this, the edge detection and extraction works better on 'cleaner' thin sections than on fractured or thin sections containing twinned minerals.

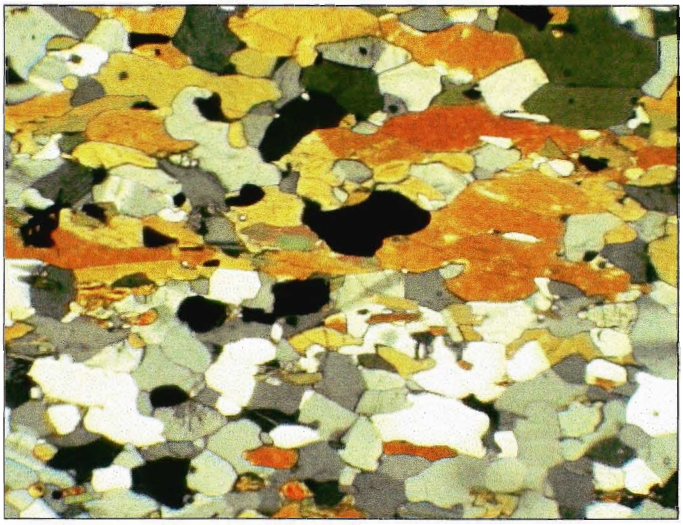

a

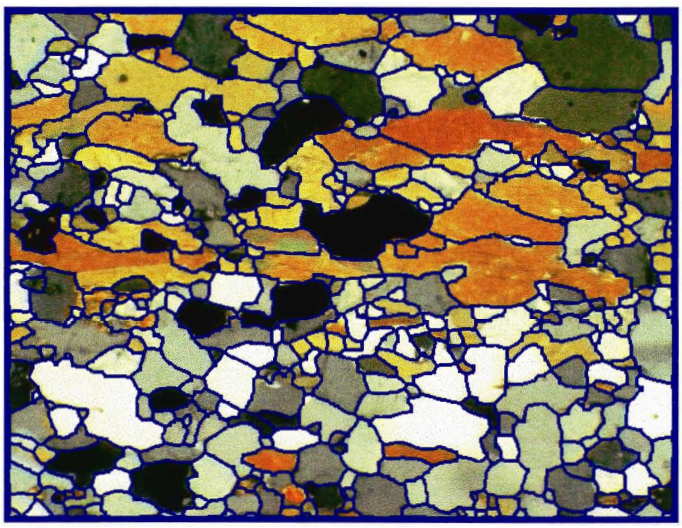

b

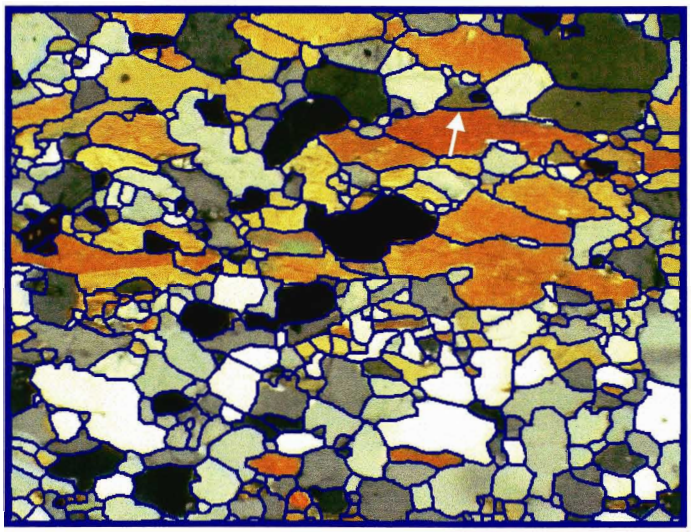

c

Although a direct comparison with the system developed by Starkey and Samantaray (1993) is impossible, some inferences can be made about the relative performance of the system described here. Starkey and Samantaray (1993) do not achieve a complete description of the grain boundaries present in a thin section automatically. Of the grain boundaries they are able to obtain, some are doubled and many are incomplete and are left as such in their final combined image. Their system does not require that detected grain boundaries form closed loops. The double edges are produced as a result of passing a Canny edge detector across the same image of the thin section at different orientations to the polarizers. Different lighting conditions can cause the detected edges, for the same grain boundaries, to be slightly offset from one another since the Canny algorithm requires boundaries to be 1 pixel wide. When the detected edges for each sequential image are then combined, double edges are produced where only a single edge should have occurred.

Even with the relatively few mistakes of false and missing edges, the overall performance of the edge detection and extraction routines described here is very good. It obtains a very nearly complete description of grain boundaries in a thin section and all of the grain boundaries detected are closed contours.

References

Allard, B. & Benn, K. (1989). Shape Preferred Orientation Analysis Using Digitized Images on a Microcomputer. *Computers & Geosciences,* **Vol. 15**, 441-448.

Canny, J. (1986). A Computational Approach to Edge Detection. *IEEE Trans. Pattern Anal. Mach. Intell.* **PAMI-8(6)**, p. 679-698.

Fabbri, A. G. (1984). Image Processing of Geological Data. *Van Nostrand Reinhold, New York, 224p.*

Foley, J. D., van Dam, A., Feiner, S. K. & Hughes, J. F. (1995). Computer Graphics Principles and Practice. *Addison-Wesley Publishing, New York, 1174p.*

Fueten, F. (1997). A computer controlled rotating polarizer stage for the petrographic microscope. *Computers & Geosciences* **Vol. 23**, p 203-208

Gonzalez, R. C. & Woods, R. C. (1992). Digital Image Processing. *Addison-Wesley Publishing, New York, 716p.*

Horn, B. K. P. (1986). Robot Vision. *MIT Press, Cambridge, Mass, 509p.*

Jain, R. Kasturi, R. & Schunck, B. G. (1995). Machine Vision. *McGraw-Hill, New York, 549p.*

Lumbreras, F. & Serrat, J. (1996). Segmentation of petrographical images of marbles. *Computers & Geosciences* **Vol. 22**, p. 547-558.

Marr, D. & Hildreth, E. (1980). Theory of Edge Detection. *Proceedings of the Royal Society of London*, Series B. **Vol. 207**, p. 187-217.

Parker, J. R. (1994). Practical Computer Vision Using C. *John Wiley & Sons, Toronto, 476p.*

Samantaray, A. K. (1993). Computer assisted petrographic image analysis and quantization of rock textures. Unpublished Ph.D. thesis, *University of Western Ontario, Ontario, Canada, 176p.*

Simigian, S. & Starkey, J. (1989). IMAGE: Modified For Use on a Microcomputer Based System. *Computers & Geosciences*. **Vol. 15**, p. 237-254.

Starkey, J. & Samantaray, A. K. (1993). Edge Detection in Petrographic Images. *Journal of Microscopy*. **Vol. 172**, p. 263-266.

Venkatesh, S. & Kitchen, L. J. (1992). Edge Evaluation Using Necessary Components. *Computer Vision, Graphics and Image Processing: Graphical Models and Image Processing*. **Vol. 54**, p. 23-30.

Chapter 4:
Semi-Automated Mineral Grain Classification In Well Segmented Petrographic Images

Chapter 4: Semi-automated mineral grain classification in well segmented petrographic images.

Abstract: A simple method for semi-automated mineral grain classification in geological thin sections is described. The method requires that images of a thin section be well segmented such that each mineral grain is spatially well defined. To classify mineral grains, a user must first select one or more representative grains from each mineral species present in an image of a thin section. The classification algorithm compares the modal colour (RGB) of each selected grain to the modal colour of each non-selected grain in the thin section. Each non-selected grain is assigned the mineral type of the previously selected grain which produced the smallest displacement vector, in colour space, with the non-selected grain in question. The accuracy of classification increases as the number of representative grains selected in the image of the thin section increases. This procedure can be applied to images of a thin section taken under conditions of both plane and cross polarized light.

Introduction

When observing a thin section with a petrographic microscope, one of the primary goals is the identification (classification) of the different mineral species present in the thin section. However, there have been relatively few attempts in the past to automate the process of mineral grain identification. Shoji (1991) developed an expert system to aid in the mineral grain identification process. It requires that the user observe mineral grains using a petrographic microscope and manually input the observed properties of individual grains into a computer. The program then compares the input data with a stored knowledge base to determine each mineral type. A similar system was developed by Shoji and Kaneda (1994) to assist in identification of ore minerals. Wang (1995) used digital image processing techniques on images of thin sections to automate the determination of the rock type represented in a thin section. Although this system proved to be successful, it does not require the classification of the individual mineral grains making up a thin section. Marschallinger (1997) describes a method for mineral classification in the macroscopic scale. Both unsupervised

and supervised classification schemes were investigated with the supervised classification scheme proving to give a higher probability for success.

This study describes a simple method of mineral grain classification within thin sections using image processing techniques. The method is one of supervised classification, which is used in the analysis of remotely sensed images (Richards 1986). In supervised classification, a representative set of mineral grains is selected by an analyst and used to train the algorithm to recognize the remaining grains in the image. The Rotating Polarizer Stage (Fueten 1997) is used to create a series of composite images from which the data necessary for classification is derived. The classification procedure makes colour comparisons between the grains and the training set in 3-D colour space (with colour axes defined by R, G and B) to perform the categorization.

To compile the data necessary for classification, the Rotating Polarizer Stage rotates its polarizers through 180^0 while the thin section remains stationary. Data are collected at each incremental step and combined once the sampling procedure is complete. This produces a series of composite images of the same field of view of the thin section. The composite images used for classification are the minimum intensity image (Figure 4.1a) and the maximum intensity image (Figure 4.1b). The minimum intensity image is collected from sampling under conditions of plane polarized light and represents, for each pixel in the image, the minimum intensity value obtained in a 180^0 rotation of the polarizers. The maximum intensity image is collected by sampling under

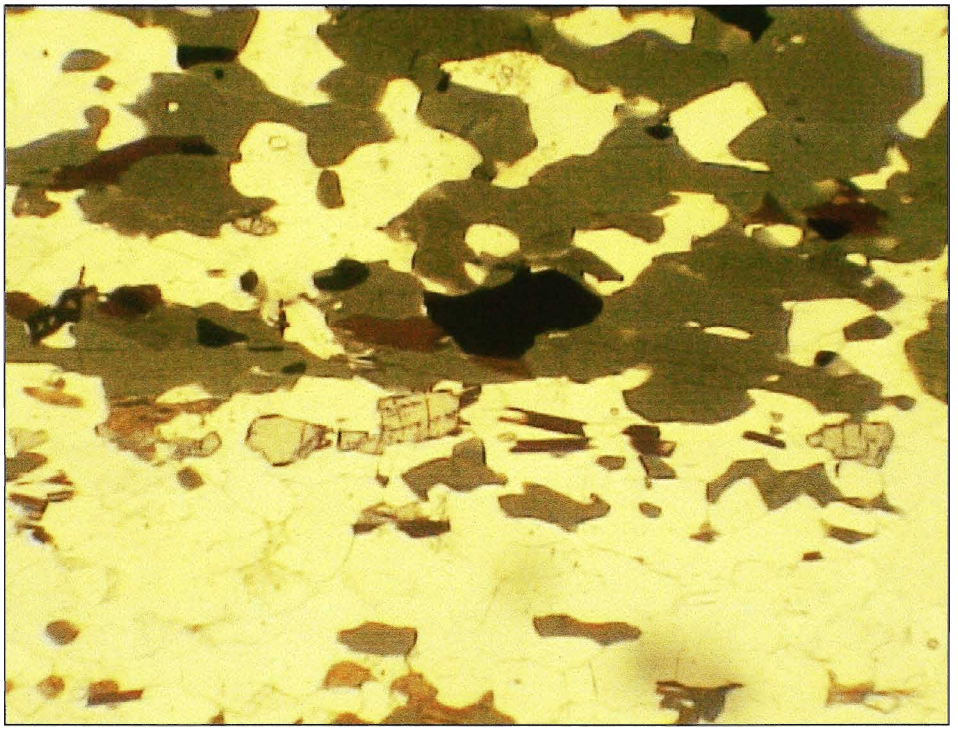

a

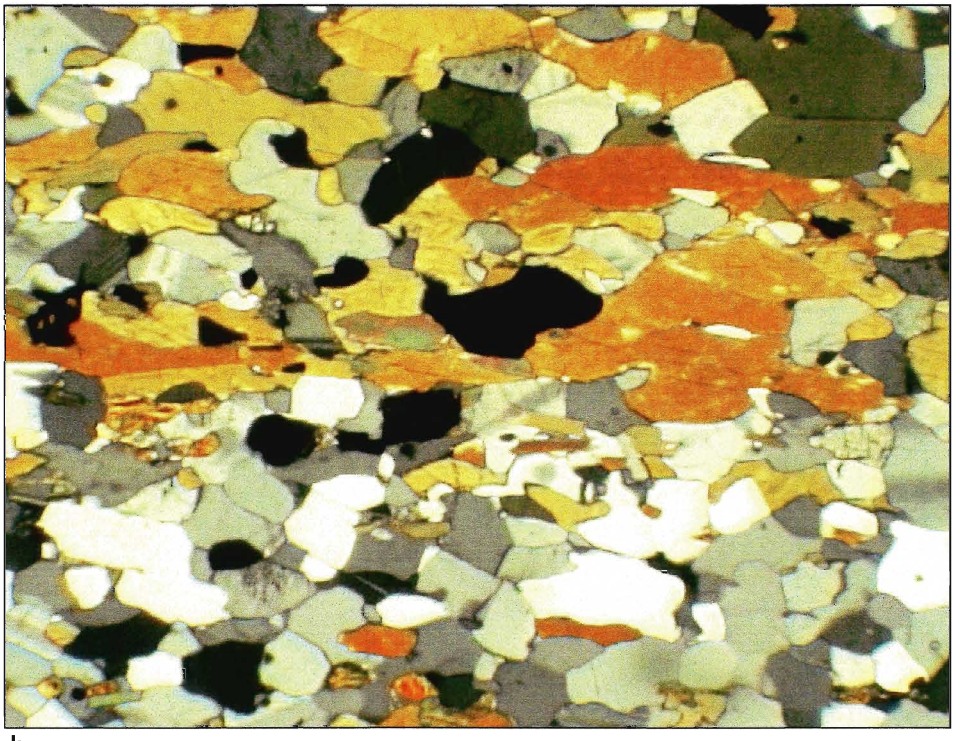

b

conditions of cross polarized light and represents, for each pixel in the image, the maximum intensity value obtained in a 180^0 rotation of the polarizers.

The Classification Procedure

In order to classify individual mineral grains within a thin section, a complete description of the spatial extent of each mineral grain is required. This can be accomplished, automatically, by applying the edge detection algorithm, outlined in chapter 3, which defines all of the mineral grain boundaries present in the viewed area of a thin section (Figure 4.2) (Goodchild and Fueten in prep.). The completely defined edges can be used to determine which pixels in the image belong to each individual grain by using a standard fill algorithm within each bounded mineral grain (Foley *et al.* 1996). Colour information, taken from each grain's constituent pixels, is statistically utilized to provide the data necessary for the classification procedure.

The classification procedure begins by requiring the user to manually select a representative example of each mineral species present in the image of the thin section (Figure 4.3). This must be repeated each time the classification algorithm is invoked as there is no permanent knowledge base from which the algorithm can retrieve colour information about different mineral species. These representative grains are termed 'seed' grains. The more seed grains picked from each species, the better able the classification algorithm is to identify the remaining grains of the same species in the thin section.

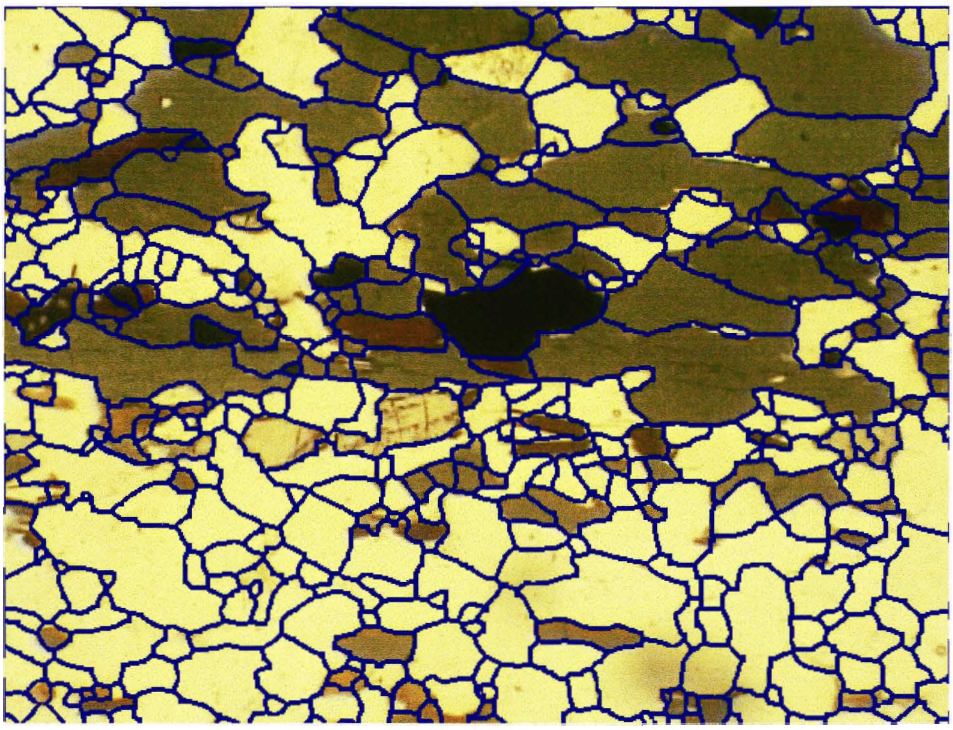

a

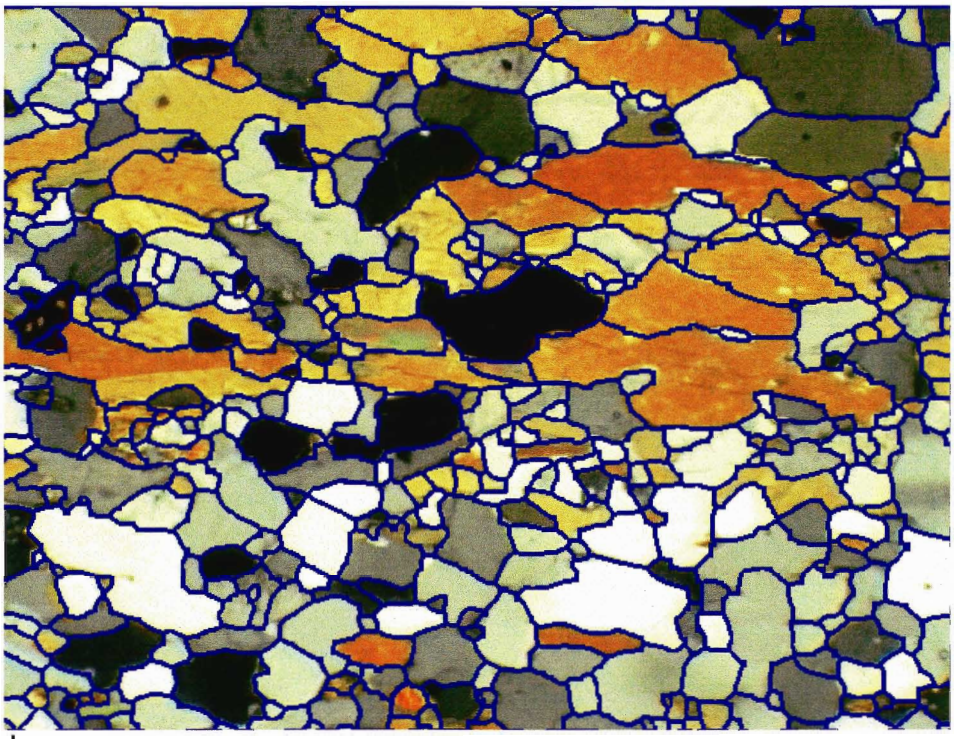

b

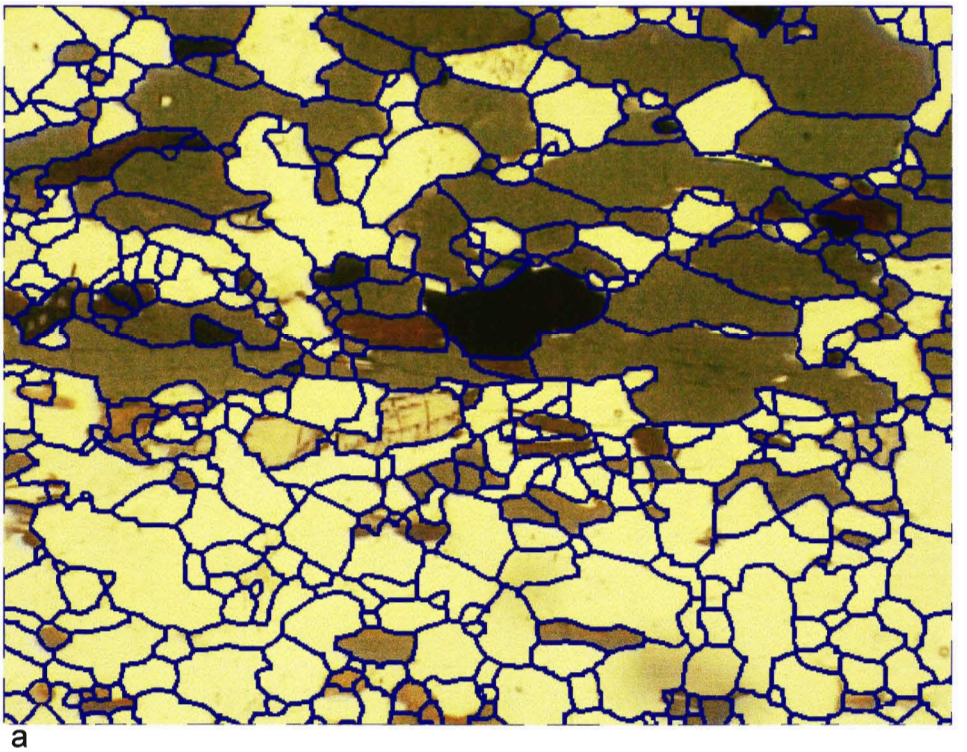

a

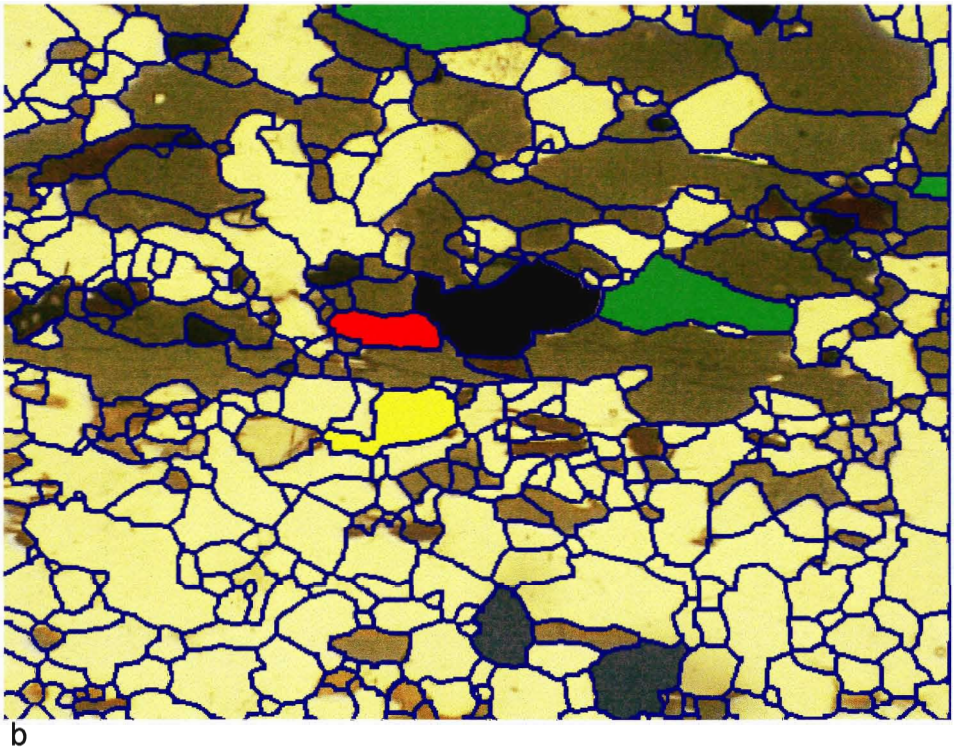

b

With the representative grains selected, the remaining mineral grains are automatically classified using simple statistical analysis. The statistical measure used to classify the remaining grains is the mode of the intensity (R + G + B) of pixels making up each mineral grain. Each, as yet unclassified, grain in the image has the intensity mode of its constituent pixels compared with the intensity mode of each of the seed grains. In 3-D colour space, each colour (or mode of colours) is represented by a point with R, G and B components. The magnitudes of the displacement vectors, defined by end points due to the unclassified grain in question and each of the seed grains, are compared to categorize the unclassified grains. Each unclassified grain is assigned to the mineral type of the seed grain that produced the smallest displacement vector magnitude for the unclassified grain in question (Figure 4.4). The directions of the displacement vectors are not considered.

The procedure of seeding and subsequent mineral grain classification can be accomplished in an image produced using plane polarized light or cross polarized light. It is sometimes easier to identify certain minerals using plane polarized light, so, normally, the classification procedure begins with the minimum intensity image. For example, it is easier to identify hornblende in plane polarized light since all the hornblende grains will occur with similar (minimum) pleochroic colours (in the minimum intensity image). Also, many minerals that are coloured in cross polarized light appear colourless in plane polarized light. This eliminates one risk of misclassification when identifying grains that are coloured in plane light, such as hornblende.

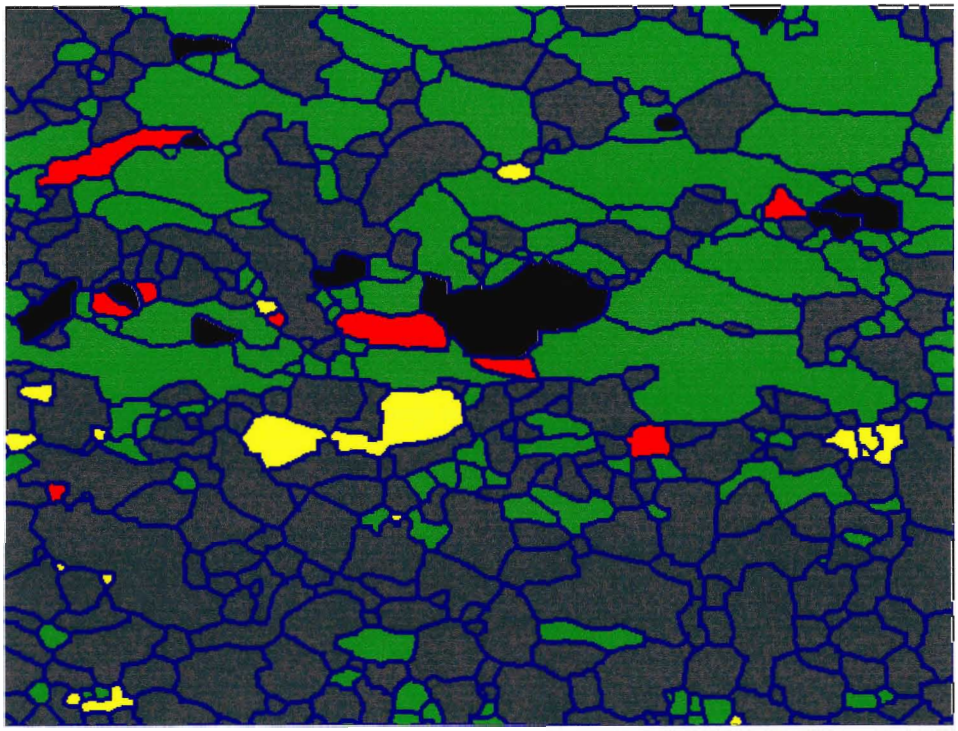

The mineral grains that appear colourless (plane polarized image) are normally identified as type 'unknown' when classified using plane polarized light (Figure 4.4). It is possible to identify the grains classified as type unknown in the plane polarized image using the cross polarized image. In the cross polarized image, all grains that were identified as other than type unknown in the plane polarized image are masked out. The colour of the mask used on each masked grain is representative of the mineral type assigned to the grain (Figure 4.5a). This leaves only the grains that were identified as type unknown in the plane polarized image to be further classified (Figure 4.5). The classification of these grains proceeds in exactly the same manner, with seed grains being selected and used to classify the remaining unmasked grains in the cross polarized image. The grains previously identified in the plane polarized image do not affect the classification of the remaining unclassified grains, since they are all masked out in the cross polarized image.

The accuracy of the classification algorithm increases as the number of seed grains selected for each species present in the thin section becomes larger. By choosing more than one seed grain to represent each mineral species, the algorithm has a greater database from which to make comparisons when determining the mineral type of unclassified grains. However, misclassifications can occur regardless of how many seed grains are used due to impurities, or dirt, within a grain. When a misclassification occurs, a built-in manual override can be used to correct the erroneous classification of the mineral grain in question. The

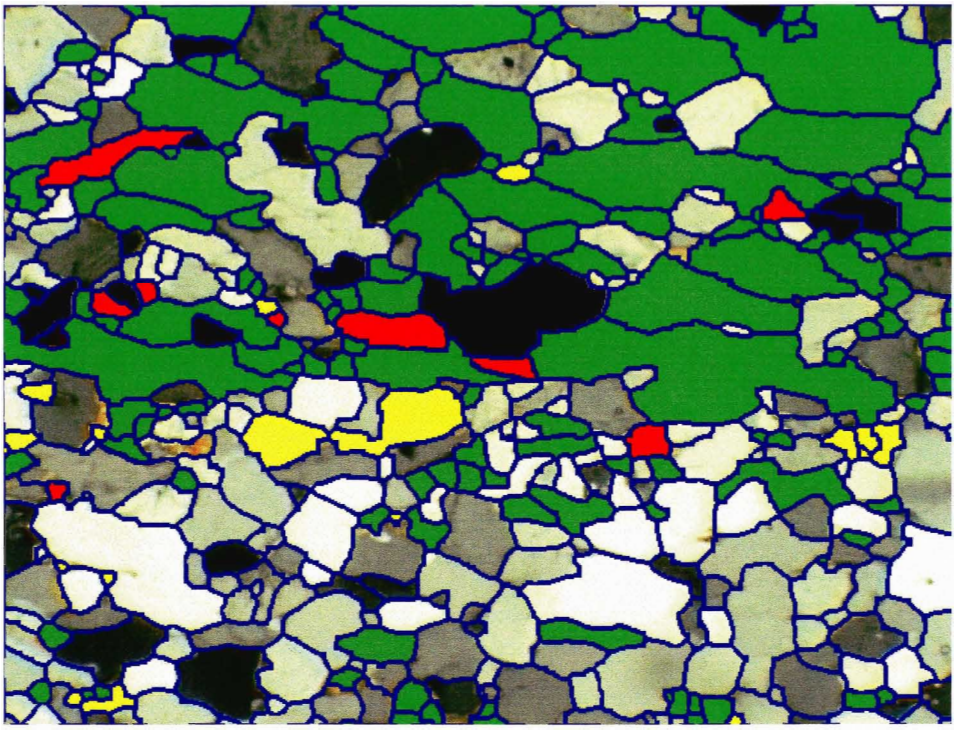

a

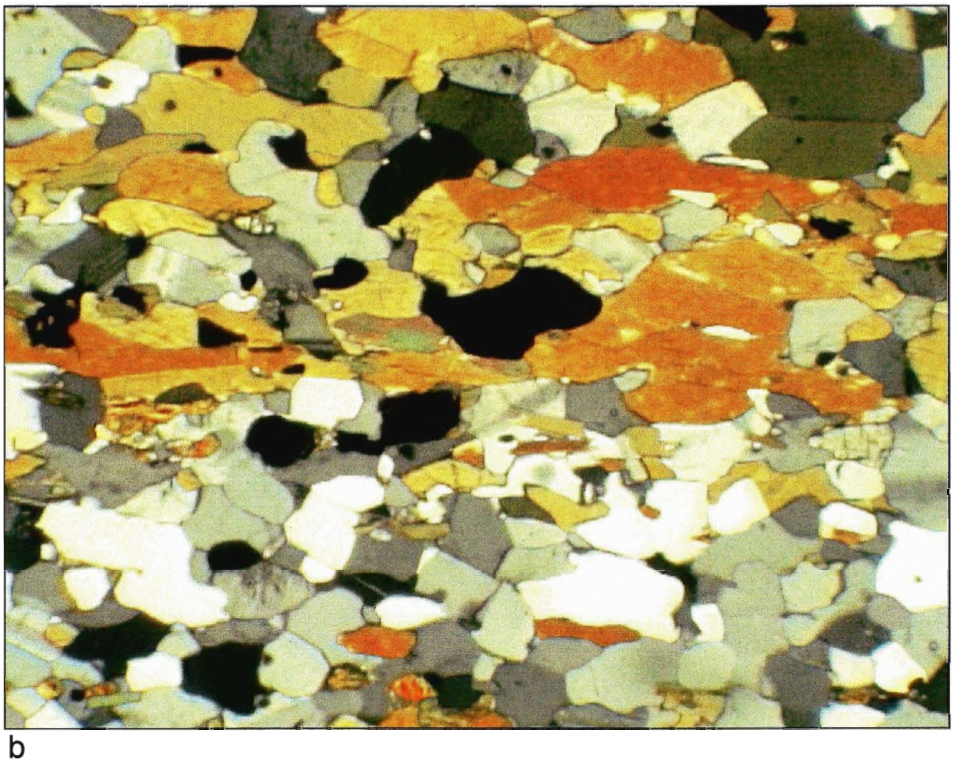

b

manual override is applied once the algorithm has classified all the non-seed grains in the image of the thin section.

Discussion

Using the Rotating Polarizer Stage to create the maximum and minimum intensity images and applying the algorithm described above is a simple yet effective method of mineral grain classification in digital images of thin sections. Once representative grains have been selected, the exact speed of classification will be dependent on the number of mineral grains in the viewed area of the thin section as well as the computer used to run the algorithm. For a viewed area of a thin section containing approximately 400 grains and running the algorithm on an SGI Indigo2, the time for classification of all non-seed grains is about 10 seconds.

The classification algorithm may assign some mineral grains to the wrong mineral type during execution. This can occur in grains that lie in an area of a thin section where there are inclusions, alterations or a smudge of dirt. Imperfections will cause changes in the intensity distribution of pixels within the grain(s) in question, which in turn causes the misclassification. Errors in classification can also occur between two mineral species whose mineral grain intensity distributions are very close. An example would be in trying to differentiate between green biotite and green hornblende in an image taken using plane polarized light. In this case, classification errors can be reduced by increasing the number of seed grains used to define each different species.

Even on a well seeded image of a thin section there are some pairs of mineral species which the algorithm cannot distinguish. An example would be feldspars and quartz. Both feldspars and quartz are colourless in plane polarized light and both show the same interference colours in cross polarized light.

With semi-automated determination of mineral species in a thin section, many interesting petrologic measurements can be easily made. These can include mineral species distributions (modal analysis), determination of which mineral species are in equilibrium and which are not, as well as any other petrologic measurements the user may be interested in.

In conclusion, the semi-automated classification of mineral species within thin sections using the Rotating Polarizer Stage has the potential to considerably reduce the amount of time required to identify mineral species and to measure many important petrologic properties of mineral grains in a thin section.

References

Foley, J. D., van Dam, A., Feiner, S. K. & Hughes, J. F. (1995). Computer Graphics Principles and Practice. *Addison-Wesley Publishing, New York, 1174p.*

Fueten, F. (1997). A computer controlled rotating polarizer stage for the petrographic microscope. *Computers & Geosciences* **Vol. 23**, p. 203-208.

Goodchild, J. S., & Fueten, F., Edge detection in petrographic images using the Rotating Polarizer Stage. In prep.

Marschallinger, R (1997). Automatic mineral classification in the macroscopic scale. *Computers & Geosciences* **Vol. 23**, p. 119-126.

Nesse, W. D. (1991). Introduction to Optical Mineralogy. *Oxford University Press, New York, 335p.*

Richards, J.A. (1986). Remote Sensing Digital Image Analysis An Introduction. *Springer-Verlag, New York.*

Shoji, T. (1991). An interactive system to assist mineral identification with the petrographic microscope. *Geoinformatics* **Vol. 2**, p. 219-224.

Shoji, T., & Hiroaki, K. (1994). An interactive system to assist in mineral identification in ore microscopy. *Mathematical Geology* **Vol. 26 No. 8**, p. 961-972.

Wang, L. (1995). Automatic identification of rocks in thin sections using textural analysis. *Mathematical Geology* **Vol. 27 No. 7**, p. 847-865.

Chapter 5:
Automated Determination Of Quartz *c*-axes Orientations

Abstract: The automated determination of quartz grain *c*-axes orientations from captured digital images of a thin section of rock can be used as an alternative to conventional petrographic methods. For each pixel within a quartz grain, the maximum intensity and the position at which the maximum intensity occurred (maximum position) are measured during the rotation of the polarizers through 180^0. The polarizer orientation at which the pixel reaches its maximum intensity is related to the trend of the *c*-axis, while the intensity value itself can be related to the inclination of the *c*-axis. Orientation of *c*-axes are plotted on an equal area net but can also be overlain on the image of a thin section. The final results compare favourably when plotted against data obtained using a universal stage.

Orientations can be represented in several different ways. Two of the techniques do not require the presence of grain boundaries to define the individual quartz grains present in the thin section. They output *c*-axes on an individual pixel basis and on a square grid basis. The *c*-axes for the square grids are taken from the modal maximum intensity and modal maximum position within each grid. Overlaying the *c*-axis grid on an image of the thin section produces *c*-axis fields which are useful in illustrating variations of *c*-axis orientations in large grains or in fine grained areas where edge detection is difficult. The technique requiring the presence of grain boundaries determines *c*-axes orientations on a grain by grain basis. The *c*-axes of individual quartz grains are taken from the modal maximum intensity and modal maximum position of each quartz grain in the thin section.

Introduction

The determination of crystallographic orientations of quartz grains in a thin section is an important procedure in the microstructural analysis of quartz bearing rock (Pauli *et al.* 1996; Turner and Weiss 1963). Studies of crystallographic directions, such as *c*-axes, can show the presence and degree of preferred crystallographic orientation within a sample, which in turn can be used to help determine the strain history of a rock.

Historically, Optical Measurements of quartz grain *c*-axes are obtained in one of two ways; by the use of a universal stage (Turner and Weiss, 1963) or by the use of the photometric method (Martinez 1958; Price 1973, 1980). The universal stage allows for the determination of *c*-axis orientations of individual

grains of quartz within a thin section. However, it is a very time consuming and labourious process. The photometric method, on the other hand, is much quicker. It measures the modal orientation of a collection of grains at once, but in doing so sacrifices the finer detail possible with a universal stage.

An alternative method of *c*-axis orientation determination was proposed by Beyna *et al.* (1990). They showed that it is possible to determine quartz *c*-axis orientations using simple image processing routines on a set of images taken from a horizontal thin section. The advantage of this is each measurement is made with incident light always through an orthogonal cross section (as opposed to using the universal stage, where the thin section must be tilted). Their method does not require the segmentation of the image to define individual quartz grains, as the *c*-axis measurements are made individually for each pixel in the image of the thin section. This allows for the determination of variations in *c*-axis orientation within grains as well as the distribution of *c*-axis orientations for the sample as a whole. Although their method is promising, the equations described by Beyna *et al.* (1990) to calculate *c*-axes trend and plunge cannot be solved directly. The trend and plunge must be approximated from their respective equations for each pixel in the image. This is much more difficult and time consuming than the simple substitutions required by the equations developed here.

A similar technique was brought forward by Heilbronner and Pauli (1993). Like Beyna *et al.* (1990) Heilbronner and Pauli (1993) determine *c*-axes orientations on a pixel by pixel basis, using image processing routines on images

of a thin section containing quartz. However, in their study, Heilbronner and Pauli (1993) make no attempt to derive analytical equations describing *c*-axes trend and plunge. Instead they rely on pre-determined experimental curves when analyzing their data. Their method further differs from the one described here as they require the use of polished thin sections, monochrome filters and a lambda plate mounted on the lower polarizer. Since the lambda plate produces a colour image, and their final data must come in the form of an intensity, the colour information produced by rotating the polarizers is reduced by inserting a monochrome filter into the light path, with the ideal filter for every different thin section determined by the thin section thickness.

This study describes a method of quartz *c*-axes measurement using image processing routines applied to images of a horizontal thin section obtained with the Rotating Polarizing Stage (Fueten 1997). The segmentation of the image to define individual quartz grains, or regions containing only quartz (Figure 5.1) (Goodchild and Fueten in prep), is initially required to ensure that *c*-axes are calculated only for quartz. Like the methods described by Beyna *et al.* (1990) and Heilbronner and Pauli (1993), *c*-axes are calculated on a pixel by pixel basis for each quartz grain, or region containing quartz, within a thin section. However, the method of *c*-axes determination introduced in this paper is much easier to implement than either of the previously developed methods. In order to display the calculated c-axes orientations, we are able to extend the pixel by pixel analysis statistically to obtain *c*-axes for individual grains, or to obtain *c*-axes for square grids breaking up a region containing quartz. The square grid method

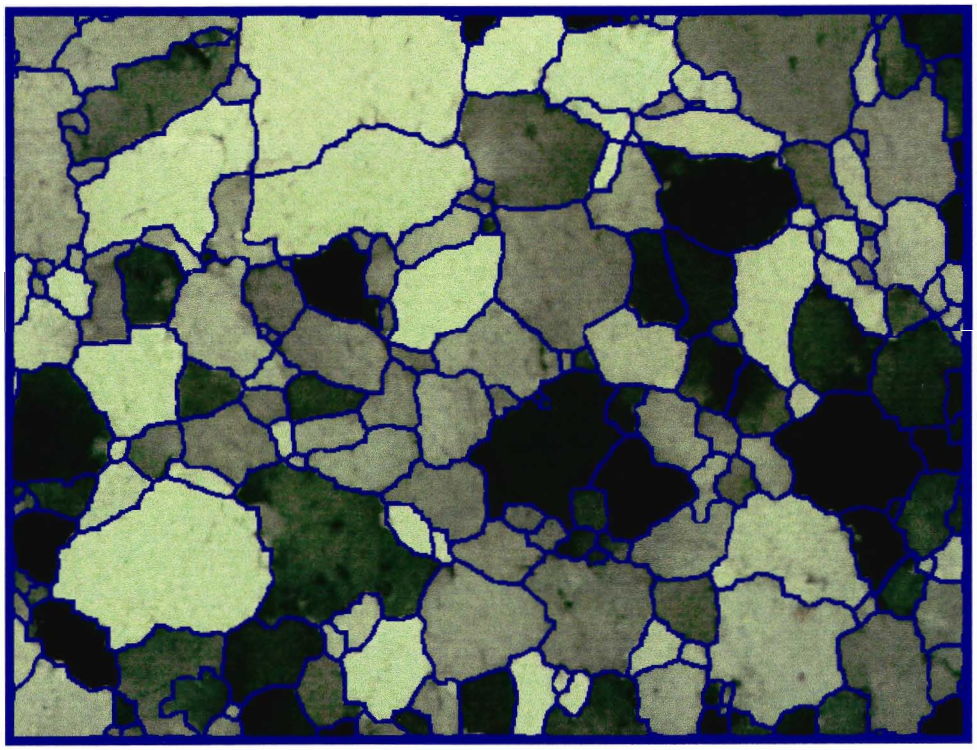

a

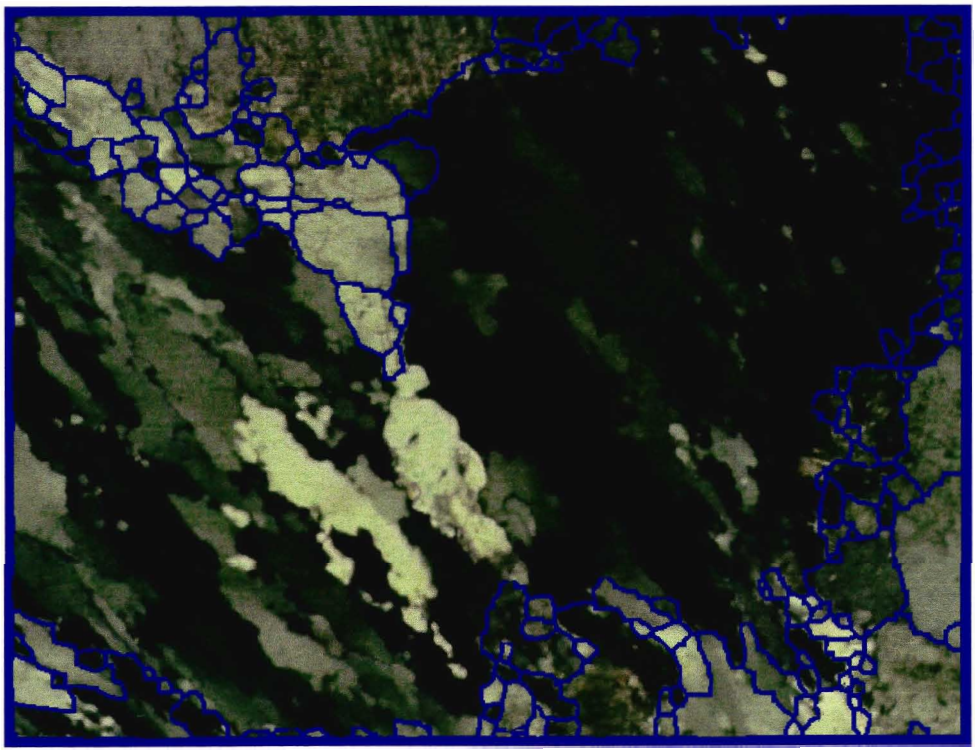

b

produces *c*-axis fields which can illustrate the variation in *c*-axis orientation within large quartz grains, or within a region containing many quartz grains. Like the results of the conventional techniques, automated measurements can be plotted on a stereo net for analysis.

Theoretical Model

To determine the orientations of quartz *c*-axes from captured images of a thin section, a mathematical model of the behaviour of quartz under cross polarized light is needed. The model relates the maximum intensity quartz obtains in a 180^0 rotation, under crossed polars, to *c*-axis inclination, and the angular position at which the measured maximum intensity occurred (relative to the planes of polarization) to *c*-axis trend.

The Rotating Polarizer Stage (Fueten 1997) is used to acquire data from a thin section. For *c*-axes orientation determination, two composite images formed from the incremental sampling process are used. They are the maximum intensity image and the maximum position image (Figure 5.2). The maximum intensity image displays the maximum intensity value obtained, for each pixel, in a 180^0 rotation of the polarizers. It is an RGB (24-bit colour) image with each of the three channels having values ranging from 0 - 255. The maximum intensity is recorded when (R + G + B) / 3 is at its highest value. The maximum position image records the position (relative to the planes of polarization) at which the maximum intensity value was obtained, for each pixel, in a 180^0 rotation of the

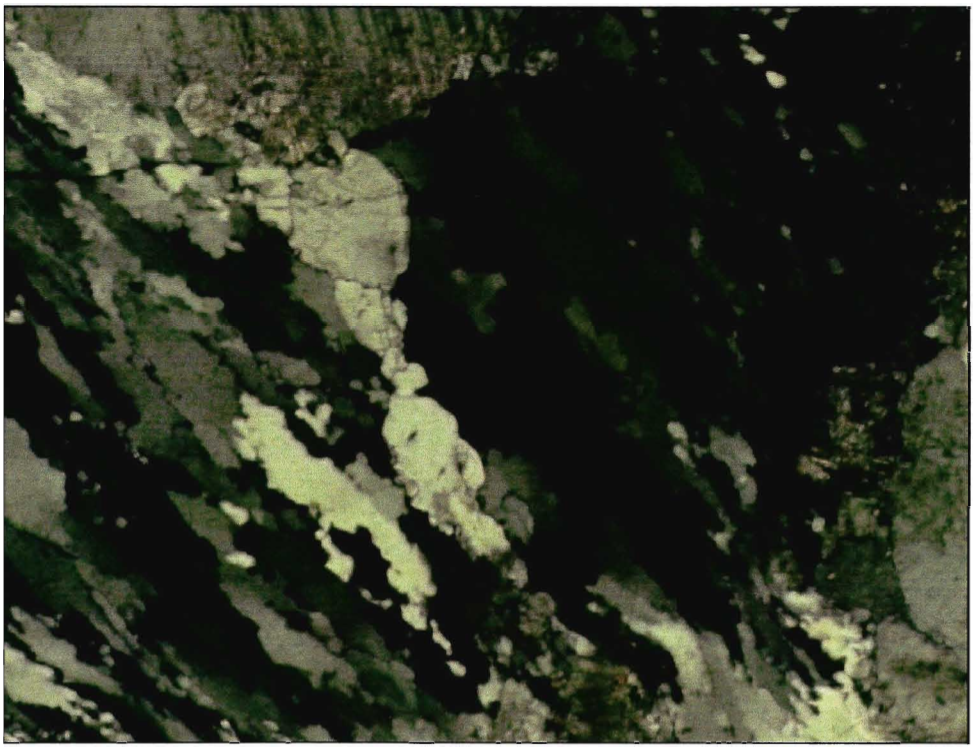

a

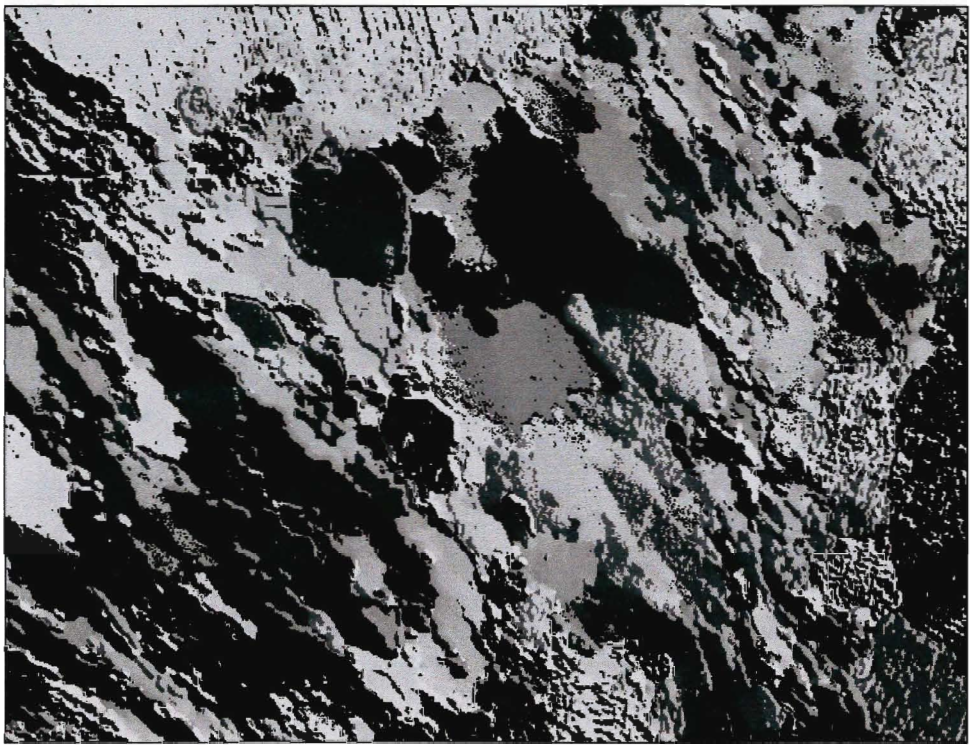

b

polarizers. It is a grey level image, with values ranging, for each pixel, from 0 - 200 in each channel.

Trend of quartz c-axes

A 180^0 rotation of the polarizers, relative to a stationary thin section, produces the occurrence of two intensity maxima and two intensity minima in quartz. The two maximum intensity peaks occur when *c*-axes are at 45^0 and 135^0 to the lower polarizer preferred vibration direction. In a normal petrographic microscope the two maximum intensity peaks are of equal intensity and colour. However, they can be distinguished by inserting an accessory plate and rotating the quartz grain. The quartz grain must be rotated relative to the stationary accessory plate, with both of the maximum intensity peaks occurring when the vibration directions of the quartz grain are parallel to the vibration directions in the accessory plate. However, the interference colours produced when the slow ray vibration direction in the interference filter is parallel to the slow ray vibration direction in quartz are of higher order than when the slow ray vibration directions are perpendicular (Nesse, 1991). This characteristic change in the interference colour provides the ability to distinguish between the two maximum intensity peaks in quartz and to determine the trend of the c-axes.

The polarizers in the Rotating Polarizer Stage are made of plastic polarizing film sandwiched between two layers of anisotropic plastic. Because the plastic is firmly attached to the polarizing layer, it will have the same orientation to the polarizing layer at all orientations of the upper polarizing filter.

Hence, its effect will be the same as the insertion of an accessory plate in a conventional microscope. Rotating the polarizers through 180^0, relative to a stationary thin section, will permit the determination of a single unique maximum intensity peak which is used for the determination of c-axes trend.

The effect of the plastic polarizing films is so small that it is not recognizable to the naked eye. However, the video capture board is sensitive enough to detect the difference in the two maximum intensity peaks within a 180^0 rotation of the polarizers (Figure 5.3).

The colour difference results in one peak having higher red and green values than the other. This means that one peak is of a more yellow (red + green) than the other. Because red and green are the two dominant channels in the system, an increase in red and green also results in an increase in the intensity ((R + G + B) / 3). Hence it is possible to use the already calculated data in the intensity image for the calculation of the trend of the c-axes.

In order to calculate c-axes trend, it is first necessary to check the system to define the orientation of the accessory vibration directions within the polarizing filter. This will determine which maximum intensity peak will be enhanced during sampling (45^0 or 135^0). The check can be accomplished by sampling a grain of quartz with a known orientation and noting the enhanced peak.

In our system it was found that the plastic acts as an interference plate with the maximum intensity peak at 135^0 enhanced. A plot of *c*-axes trend vs. position at which the maximum intensity occurred in a 180^0 rotation of the polarizers was constructed in order to derive a mathematical relationship

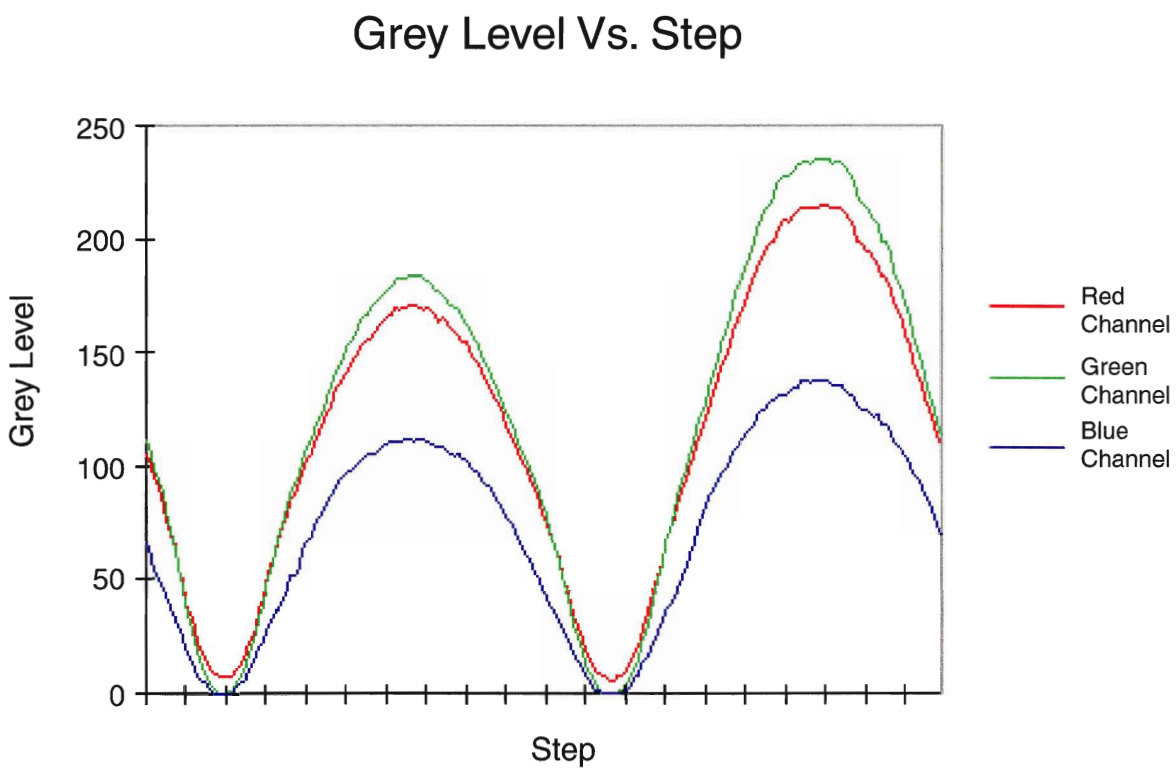
Grey Level Vs. Step
250
200
150
100
50
0
Grey Level
Step
Red Channel
Green Channel
Blue Channel

between c-axis trend and maximum position (Figure 5.4). The trend data were collected for individual grains of quartz from measurements made on a universal stage. The maximum position data was collected by taking the mode of the maximum positions of individual pixels making up the quartz grains. The plot shows a simple linear relationship between *c*-axes trend and the position at which maximum intensity occurs.

Analysis of the plot allows the fit of linear curves to the data collected. When the maximum position measured is less than or equal to 45^0 the following equation holds:

$$\text{trend} = \text{maximum position} + 135^0 \quad (5.1).$$

When the maximum position measured is greater than 45^0 the following equation holds:

$$\text{trend} = \text{maximum position} - 45^0 \quad (5.2).$$

In Figure 5.4 there are data points that do not fit on either one of these curves. These data correspond to erroneous measurements of the position of the enhanced maximum intensity. In this situation, errors introduced into the system by the light source and/or the video board can cause the maximum at the 45^0 position to be greater than the maximum at the 135^0 position (for the current system setup). The number of data points that are in error correspond to approximately 5% of the data points plotted.

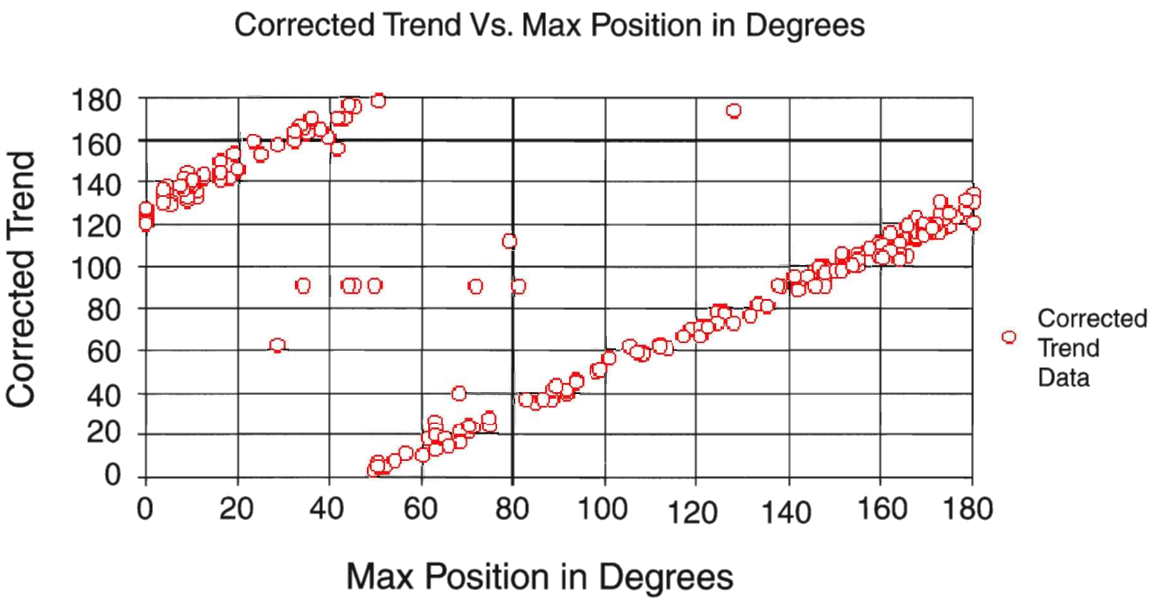
Corrected Trend Vs. Max Position in Degrees
Corrected Trend
180
160
140
120
100
80
60
40
20
0
0
20
40
60
80
100
120
140
160
180
Max Position in Degrees
Corrected Trend Data

Inclination of quartz c-axes

With quartz, the magnitude of the global maximum intensity reached in a 180^0 rotation of the polarizers will be dependent on the inclination of its *c*-axis. The greatest intensity magnitudes are attained when *c*-axes are horizontal or near horizontal, while the smallest intensity maxima are reached when *c*-axes are vertical or near vertical. The inclination of the *c*-axes measured on a universal stage, when plotted against the maximum intensity data, do not produce a linear relationship. Hence, it was necessary to use the uniaxial positive indicatrix (quartz being a uniaxial positive mineral) to determine the mathematical relationship between *c*-axis inclination and maximum intensity.

The behaviour of light as it passes through quartz is modeled by the uniaxial positive indicatrix (Figure 5.5). In the uniaxial (positive) indicatrix, the two allowed, mutually perpendicular vibration directions, will always lie in an elliptical section that is perpendicular to the wave normal direction of the incident light. The vibration directions are parallel to the axes of the elliptical section and the refractive indices define the lengths of the axes. In Figure 5.5a, the ordinary ray, ω, vibrates parallel to AB and has refractive index n_ω. The component of the extraordinary ray, ε', vibrates parallel to AC and has refractive index n'_ε. The angle between the wave normal (WN) and the optic axis (OA), θ, is equivalent to the angle between n'_ε and the plane of the circular section (Figure 5.5b).

In any uniaxial mineral, such as quartz, the *c* crystallographic axis is coincident with the optic axis of its indicatrix. Further, the wave normal of the incident light on a thin section in a petrographic microscope is vertically oriented.

Uniaxial Positive Indicatrix

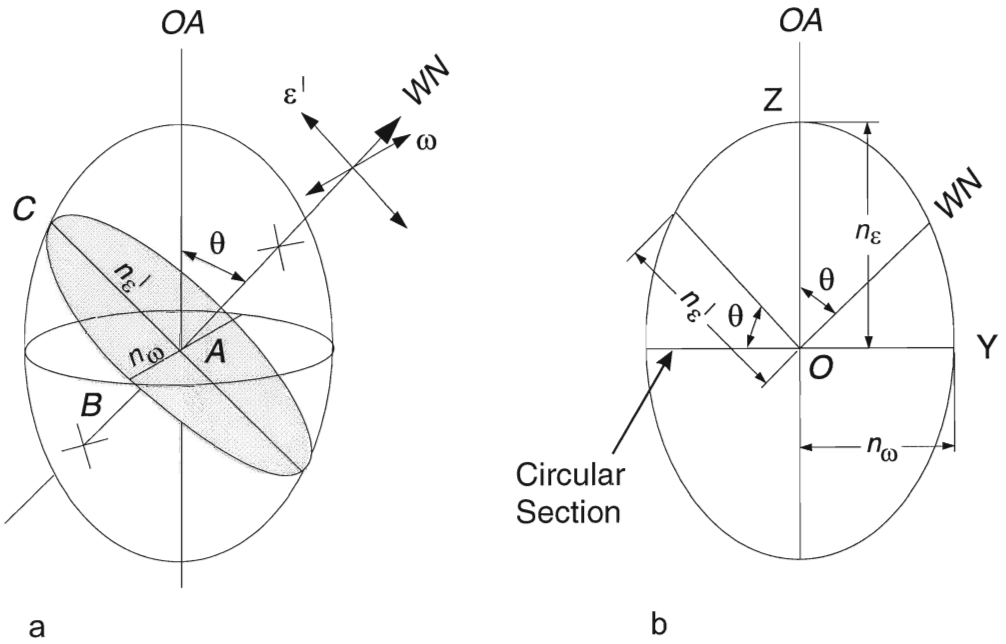

Hence, the angle θ, in Figure 5.5, can be thought of as defining the angle between the *c* crystallographic axis in a quartz grain and vertical.

We can define the principal section of the uniaxial positive indicatrix in Figure 5.5b, by the equation of an ellipse:

$$\frac{y^2}{n_\omega^{\,2}} + \frac{z^2}{n_\varepsilon^{\,2}} = 1 \qquad (5.3)$$

To put equation 5.3 into polar form, let $y = n'_\varepsilon \cos\theta$ and $z = n'_\varepsilon \sin\theta$

$$\frac{n'^{\,2}_\varepsilon \cos^2\theta}{n_\omega^{\,2}} + \frac{n'^{\,2}_\varepsilon \sin^2\theta}{n_\varepsilon^{\,2}} = 1 \qquad (5.4)$$

Re-arranging and solving equation 5.3 for $n'^{\,2}_\varepsilon$ yields:

$$n'^{\,2}_\varepsilon = \frac{n_\omega^{\,2} n_\varepsilon^{\,2}}{n_\varepsilon^{\,2}\cos^2\theta + n_\omega^{\,2}\sin^2\theta} \qquad (5.5)$$

Simplifying equation 5.5 so that there is only one term involving θ produces:

$$n'^{\,2}_\varepsilon = \frac{n_\omega^{\,2}}{\left(\frac{n_\omega^{\,2}}{n_\varepsilon^{\,2}} - 1\right)\sin^2\theta + 1} \qquad (5.6)$$

Solving for θ yields:

$$\theta = \frac{1}{2}\cos^{-1}\left[1 - 2\frac{\left(\frac{1}{n'^{\,2}_\varepsilon} - \frac{1}{n_\omega^{\,2}}\right)}{\left(\frac{1}{n_\varepsilon^{\,2}} - \frac{1}{n_\omega^{\,2}}\right)}\right] \qquad (5.7)$$

Equation (5.7) relates the angle between the *c*-axis and vertical, for quartz, to the ratio of partial birefringence to birefringence. However, to utilize this formula we would need to be able to easily measure n'_ε, n_ε and n_ω, which we cannot do. The solution to this problem is to replace the ratio of partial birefringence to

birefringence with the ratio of maximum intensity attained in a 180^0 rotation to maximum possible intensity in a 180^0 rotation. The justification for this is as follows:

The theoretical percentage light transmission through the analyzer given by Price (1973) (see also McKie and McKie 1974) is

$$I = \cos^2\phi - \sin 2(\tau - \phi)\sin 2\tau \sin^2\left(\frac{\pi d(n'_\varepsilon - n_\omega)}{\lambda}\right) \qquad (5.8):$$

where, I represents the percentage of light transmitted through the analyzer; ϕ represents the angle between the allowed vibration directions in the polarizer and analyzer; τ represents the angle between the polarizer's allowed vibration direction and the quartz grain's closest allowed vibration direction; d represents the thickness of the sample; and λ represents the wavelength of the light.

In this study, all measurements were made at $\phi = 90^0$ (crossed polars) and at the position of maximum intensity $\tau = 45^0$ or 135^0. Substituting these values into equation (5.8) produces:

$$I = \sin^2\frac{\pi d(n'_\varepsilon - n_\omega)}{\lambda} \qquad (5.9)$$

In uniaxial minerals, both of the principal refractive indices are wavelength dependent (McKie and McKie 1974). This means both the size and shape of the indicatrix can vary with wavelength. In quartz, the dispersion of the extraordinary and ordinary rays are small and they follow a similar path (Figure 5.6). Consequently, the dispersion of the birefringence is negligible. This causes the

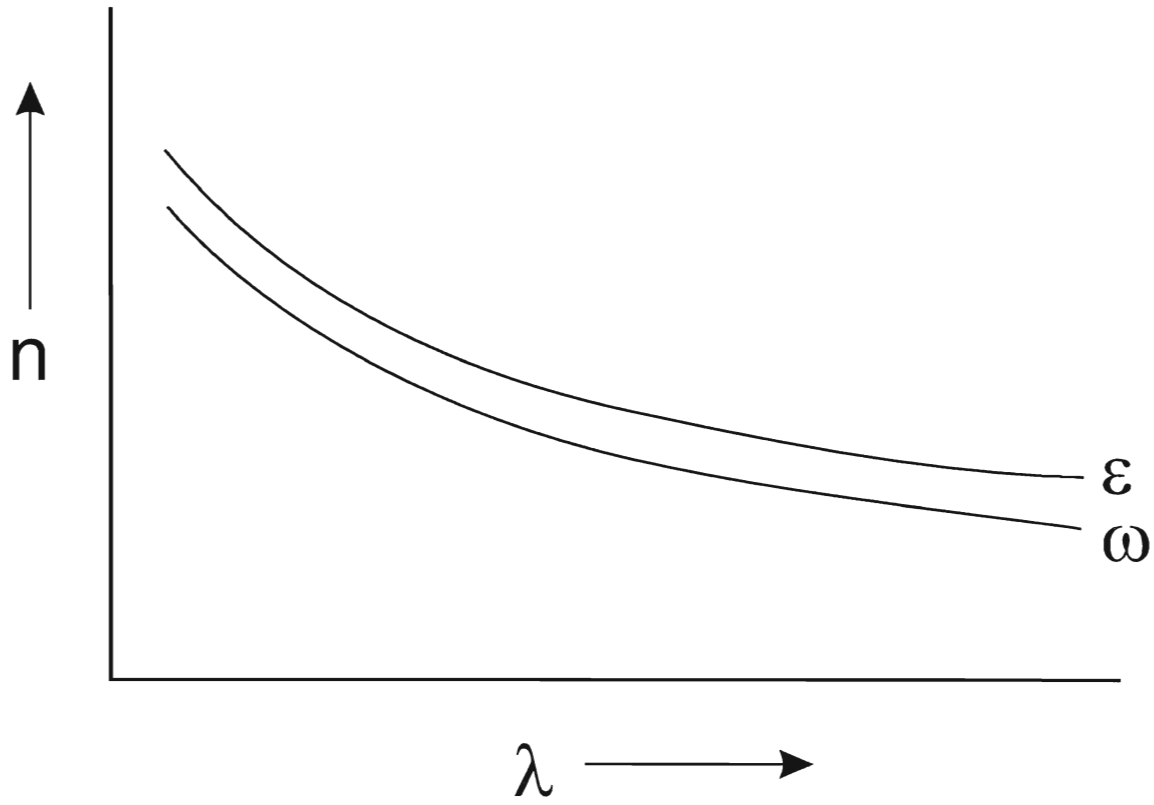
n
ε
ω
λ

size of the quartz indicatrix to vary with wavelength, while the shape remains constant.

Hence, for a sample of constant thickness and light of any wavelength, the maximum intensities that quartz grains can acquire are controlled solely by the birefringence of each individual grain in question.

Using the relation above we can approximate the birefringence in a quartz grain by the maximum intensity that grain acquires in a 180^0 rotation. To accomplish this mathematically, we replace the term $\left(\frac{1}{n_\varepsilon'^2}-\frac{1}{n_\omega^{\ 2}}\right)$ in equation (5.7) with the maximum intensity the mineral grain acquires in a 180^0 rotation (I); and the term $\left(\frac{1}{n_\varepsilon^{\ 2}}-\frac{1}{n_\omega^{\ 2}}\right)$ in equation (5.7) with the maximum possible intensity a quartz grain can acquire in a 180^0 rotation (I_{max}). Substituting into equation (5.7) produces:

$$\theta=\frac{1}{2}\cos^{-1}\left[1-2\frac{I}{I_{\max}}\right] \qquad (5.10)$$

Equation (5.10) relates the *c*-axis orientation measured from the vertical to the intensity ratio the grain acquires in a 180^0 rotation. It is preferable to have the *c*-axis orientation measured from the horizontal as this is the customary way to measure *c*-axis inclination. To do this we replace θ with $\frac{\pi}{2}-\theta$ in equation (5.10).

This produces the equation relating *c*-axis inclination to the maximum intensity a quartz grain acquires in a 180^0 rotation:

$$\theta = \frac{\pi}{2} - \frac{1}{2}\cos^{-1}\left[1 - 2\frac{I}{I_{\max}}\right] \qquad (5.11)$$

Which simplifies to the final form of the equation (Appendix III):

$$\theta = \frac{1}{2}\cos^{-1}\left[2\frac{I}{I_{\max}} - 1\right] \qquad (5.12).$$

The intensities used in equation 5.12 are calculated from the intensity defined in the Hue, Saturation and Intensity (HSI) colourspace. This means the value of I has a range of 0 - 255 and is calculated from the maximum intensity image using the formula (for each pixel):

$$I = \frac{R + G + B}{3} \qquad (5.13).$$

Figure 5.7 is a plot of equation 5.12 with $I_{\max}$ set to 255 (full 8 bit intensity range).

In practice $I_{\max}$ must be obtained through a calibration process prior to calculating *c*-axes from the measured maximum intensities. This calibration can be done in one of three ways. The first is to arbitrarily assign $I_{\max}$ to a value of 255, preserving the full 8 bit range of possible intensity values. Using this calibration, we are assuming that horizontal *c*-axes will always reach an intensity level of 255. Different lighting conditions will cause the maximum intensity attained in a 180^0 rotation to vary. Thus, simply assigning the maximum possible intensity to 255, in many cases, will cause errors. A second method of calibration is to measure the value of $I_{\max}$ directly from the thin section being studied. This

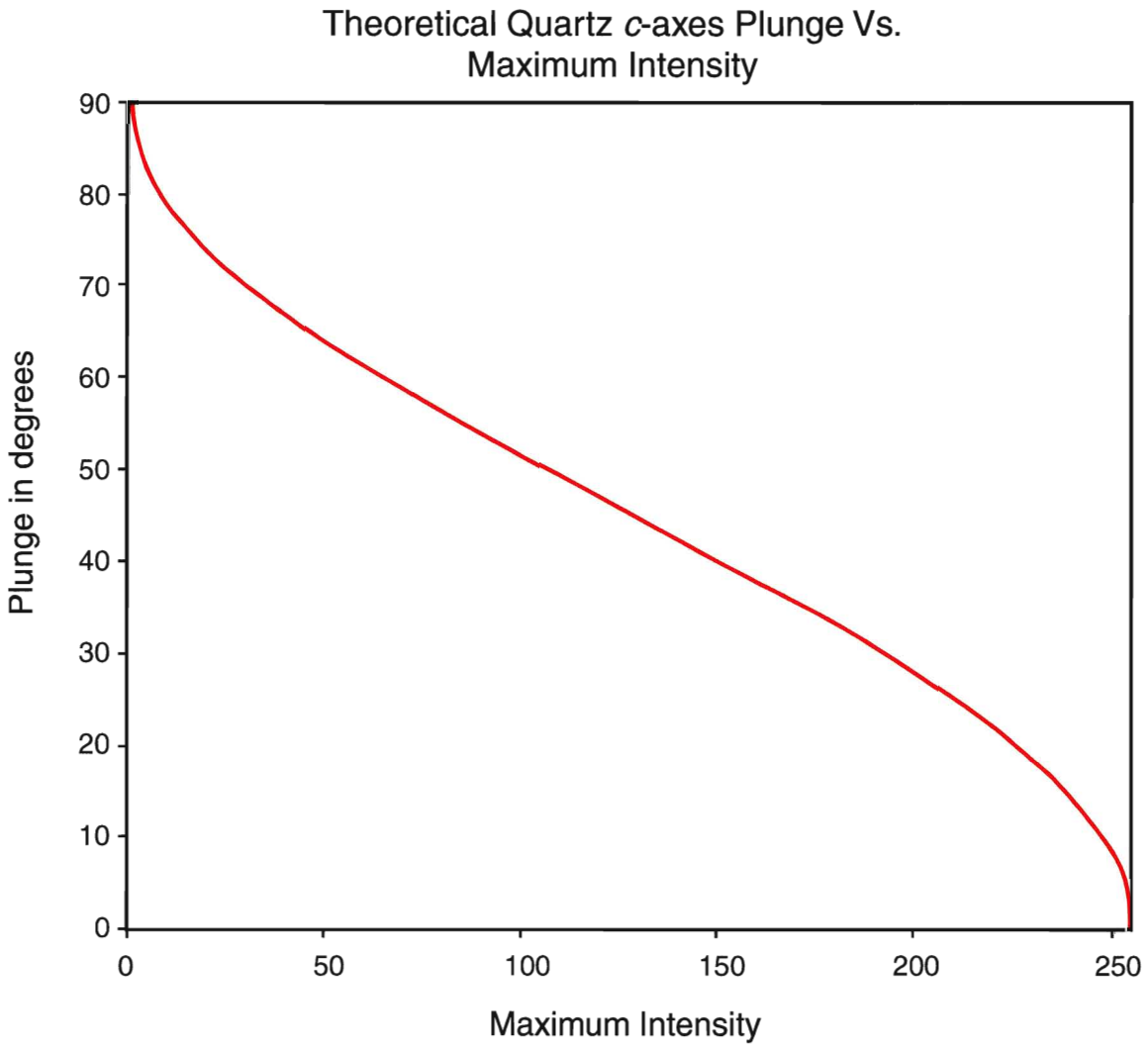
Theoretical Quartz c-axes Plunge Vs.
Maximum Intensity
Plunge in degrees
90
80
70
60
50
40
30
20
10
0
0
50
100
150
200
250
Maximum Intensity

is accomplished by finding the maximum quartz intensity and assigning that value to $I_{\max}$. The limitations of this method are 1) we are assuming that the quartz that produced the highest intensity value has it's *c*-axis horizontal and 2) there is no common maximum value between different samples. The third and final calibration method would be to measure a quartz grain of known orientation (preferably with a horizontal *c*-axis). This would allow the value of $I_{\max}$ to be determined such that any subsequent samples taken (without changing the light levels used to calibrate the system and assuming all samples are of approximately equal thickness) would have a known global intensity maximum corresponding to quartz with a horizontal *c*-axis.

In order to verify the use of the theoretical curve, a plot of *c*-axes inclination vs. maximum intensity was constructed (Figure 5.8). Two sets of data are displayed on the plot. The solid black circles represent the theoretical relationship between inclination and maximum intensity (derived above). The open red circles are a plot of inclination of quartz *c*-axes measured on the universal stage vs. maximum intensity attained in a 180^0 rotation. Although the data show a good fit to the theoretical curve, the data in the region between maximum intensity 60 and maximum intensity 150 show most of the plotted points falling above their expected values while the data between maximum intensity 150 and 250 show most of the plotted points falling below their expected values. A possible explanation for this is the response of the camera and/or video board to the intensity of transmitted light. This has not yet been fully investigated, but should be in the future.

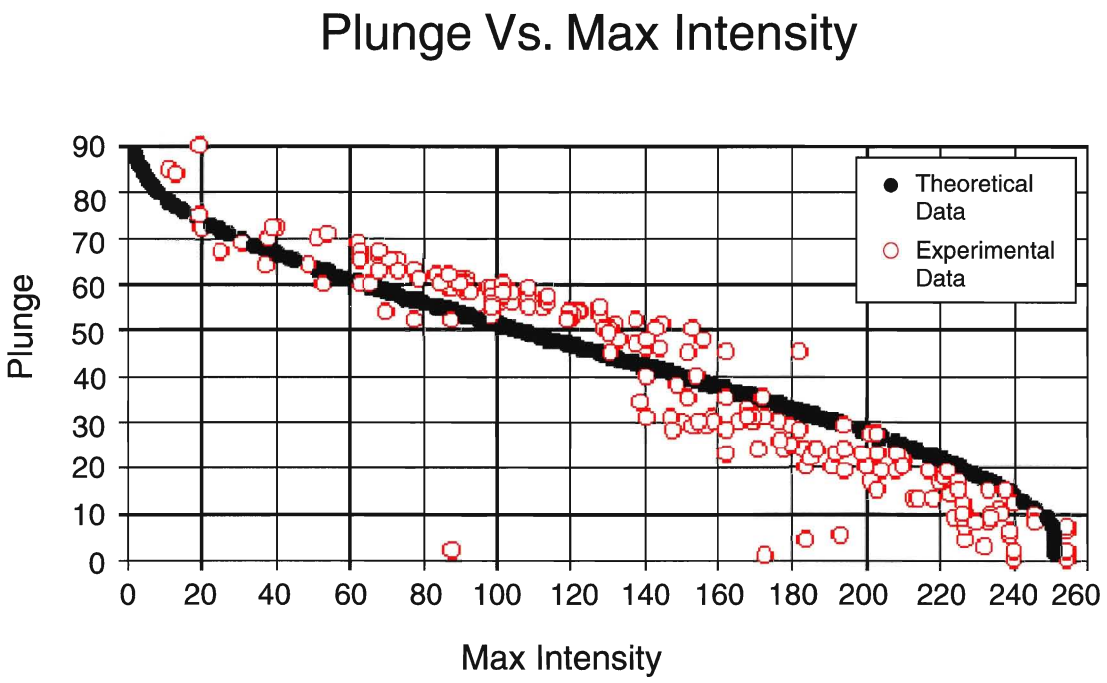
Plunge Vs. Max Intensity
Plunge
Max Intensity
0
10
20
30
40
50
60
70
80
90
0
20
40
60
80
100
120
140
160
180
200
220
240
260
Theoretical Data
Experimental Data

Application

Quartz *c*-axes are calculated for each pixel belonging to a grain or region that is classified as quartz. It is also desirable to produce a single *c*-axis for each quartz grain present, or to produce a single *c*-axis for small rectangular areas breaking up a region containing quartz. The rectangular grid elements can range in size from 10 pixels by 10 pixels to 100 pixels by 100 pixels, with the actual size used being selected by a user. To acquire *c*-axes for individual grains or grids, we must extend statistically the data used to calculate individual pixel *c*-axes. Therefore, for individual grains, the trend of the *c*-axis is calculated by using the modal maximum position of all the pixels within the quartz grain and the inclination of the *c*-axis is calculated by using the modal maximum intensity of all the pixels within the grain. Similarly, for regions containing quartz, the trend and inclination of the *c*-axes are found by using modal analysis on each of the small grid elements making up the region.

For individual quartz grains, the calculated *c*-axes can be displayed on a stereo net as well as overlain on one of the composite images of the thin section (Figure 5.9). Figure 5.9a shows the *c*-axes for each quartz grain overlain on top of the maximum intensity image. For each individual grain, the direction of the line represents the trend of the *c*-axis and the length of the line represents the inclination of the *c*-axis. The longer lines correspond to *c*-axes that have a shallow inclination, while shorter lines correspond to *c*-axes that have a steep inclination. Figures 5.9b and 5.9c show stereo net plots of the *c*-axes for the thin section represented by the image in Figure 5.9a. In Figure 5.9b, each *c*-axis is

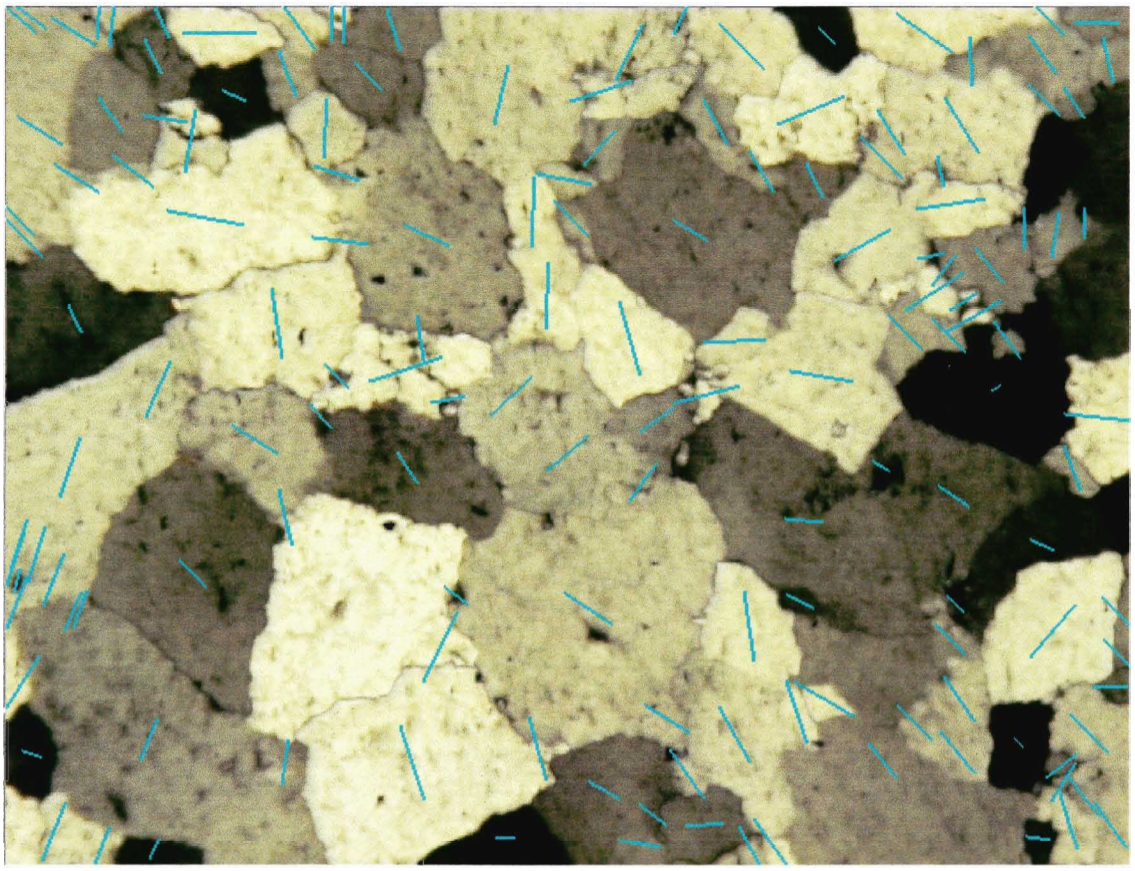

a

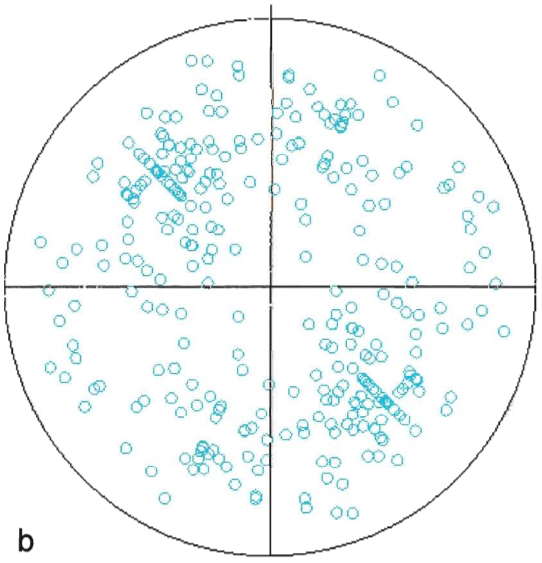

b

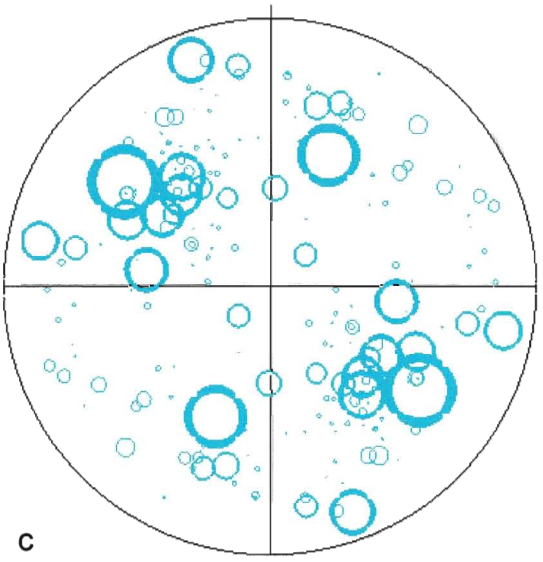

c

represented by an open circle. In Figure 5.9c, each *c*-axis is also represented by an open circle, however, the size of the circle representing a particular *c*-axis is a function of the relative area (in pixels) of the quartz grain from which the *c*-axis was calculated. Therefore, the larger the circle, the larger the quartz grain the *c*-axis was calculated from. For regions in thin sections containing quartz that are very fine grained, or are difficult to detect edges in (Goodchild and Fueten in prep), *c*-axes can be calculated on a rectangular grid within the region of interest (Figure 5.10). The calculated *c*-axes can be displayed on a stereo net as well as overlain on one of the composite images of the thin section. Figure 5.10a shows the *c*-axes calculated using a 10 pixel by 10 pixel grid for a region identified as containing quartz overlain on top of the edge extracted image. Figure 5.10b shows the same *c*-axes overlain on top of the maximum intensity image. The rectangular grid method produces *c*-axes 'fields' within the region of interest when the *c*-axes are overlain on top of a composite image. These are useful in visualizing the distribution of *c*-axes within a fine grained region as well as the variations in *c*-axis orientation within larger grains of quartz.

Some of the grid elements in a region containing quartz will have edge pixels within them or will possess pixels from an adjacent mineral grain, identified as something other than quartz. In each element, the pixels that were not identified as quartz are not used in the determination of the modes. Therefore, a minimum number of quartz pixels must be present to allow for a meaningful calculation of orientation of *c*-axes. Hence, each grid element is only allowed to produce a *c*-axis when at least 50% of the pixels making up the element were

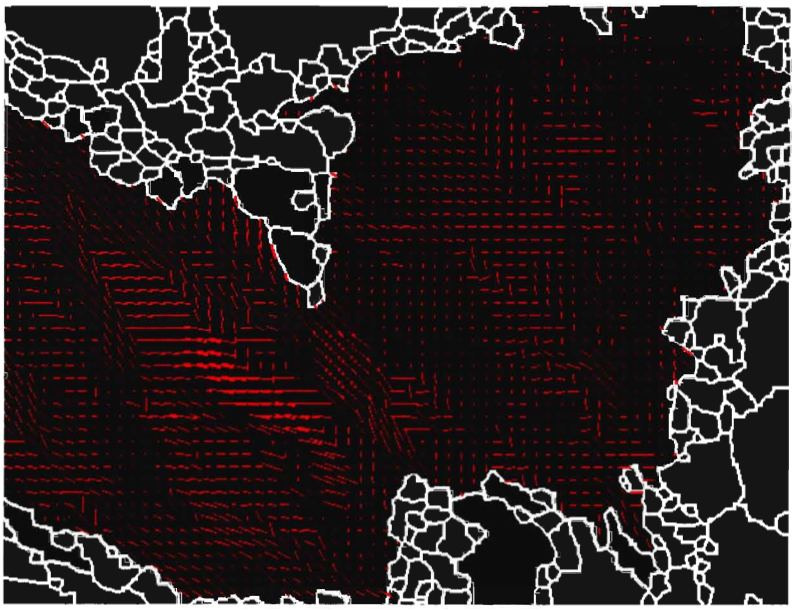

a

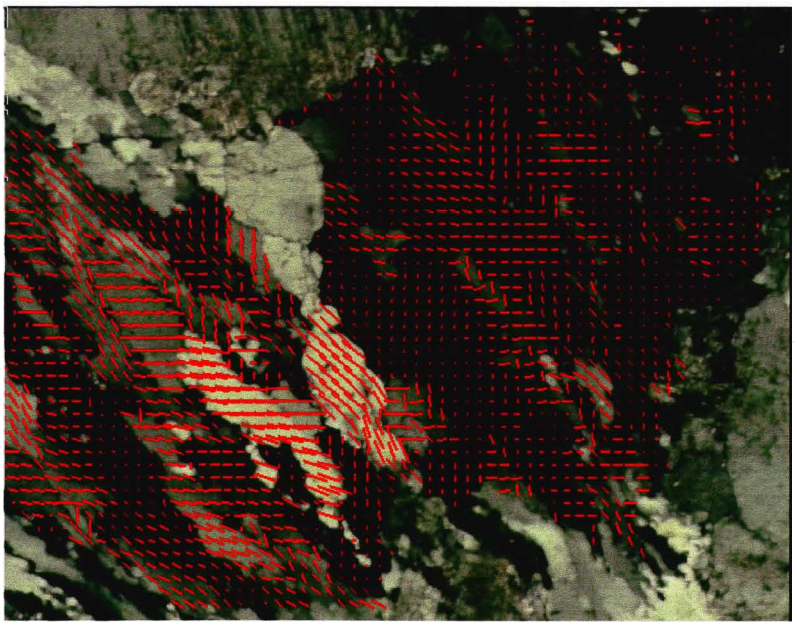

b

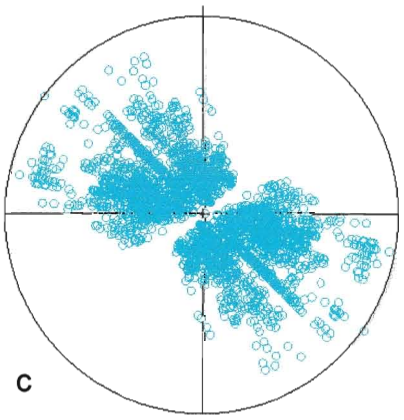

c

identified as pixels representing quartz. With this, the calculation of the orientation of *c*-axes is performed using enough pixels such that comparisons can be meaningfully made between different grid elements.

Discussion

Using the Rotating Polarizer Stage to create the maximum position and maximum intensity images and applying the formulae specified above produces *c*-axes for quartz in the viewed area of a thin section. The *c*-axes can be calculated for individual quartz pixels, individual quartz grains or they can be calculated on a rectangular grid within a region containing quartz. Calculated *c*-axes can be overlain on top of a composite image of the thin section or plotted on a stereo net for analysis.

Although the angle of inclination can be accurately calculated, the fact that *c*-axes measurements are made on images of a horizontal thin section makes it impossible to uniquely determine the sense of the inclination. The calculated inclination can correspond to a real *c*-axis oriented either above or below the plane of the thin section (Figure 5.11). In practice, however, this is not a critical problem. If the thin section is cut properly, so that the lineation direction is known, we are then mainly interested in the asymmetries in quartz *c*-axis orientations. Studying thin sections in this way removes the need to know whether or not the quartz *c*-axes are pointing above or below the plane of the thin section.

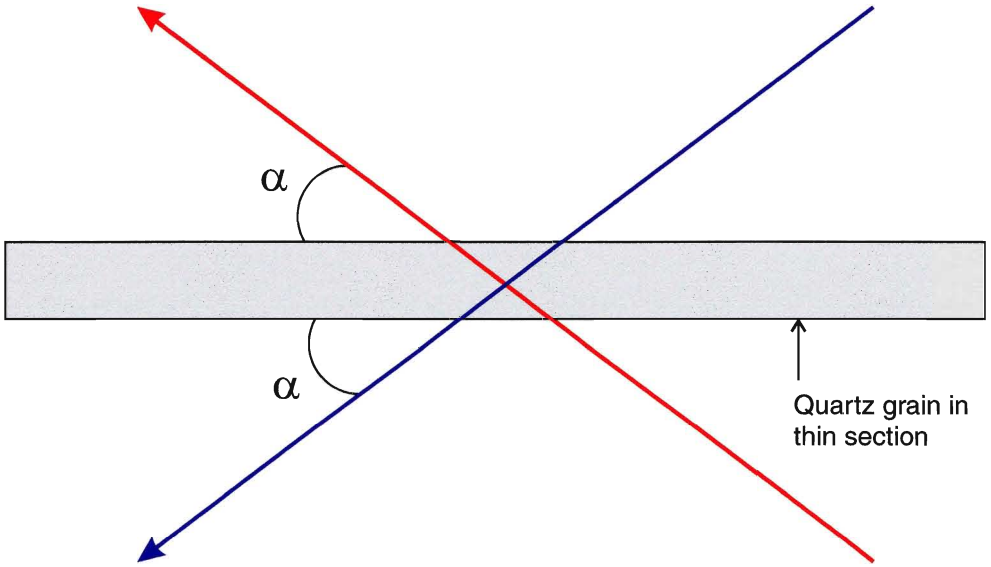
α
α
Quartz grain in
thin section

Since *c*-axes calculations are made for both trend and inclination using an 8-bit range of data, there are inevitable gaps in the set of points plotted on the stereo net. The best way to illustrate this shortcoming is with an example. In the formula for inclination (Equation 5.12), if we assume a maximum intensity value of 255 (full 8-bit range for data), the *c*-axis angle produced for quartz with an intensity of 0 is 90^0, as expected. If the same calculation is done for quartz with a maximum intensity of 1, the *c*-axis angle produced is 86.4^0. Therefore, there is a 3.6^0 gap in inclination between quartz with intensity 0 and quartz with intensity 1, which will never have points plotted in it. A possible way to reduce (but not eliminate) this inclination gap would be to expand the intensity range. Instead of calculating intensity over an 8-bit range, we could calculate it over a 3 * 8-bit range by modifying equation 5.13 so that it takes the following form:

$$I = R + G + B \qquad (5.14).$$

Using equation 5.14, the (theoretical) inclination gap is reduced to 2.1^0, between intensity value 0 and intensity value 1.

Even with the gaps in the plotted points on a stereo net produced by the 8-bit range of input data, the overall performance of the quartz *c*-axes determination algorithm is very good. The determination of quartz *c*-axes using a rectangular grid allows for a description of *c*-axes that was previously impossible to attain. The *c*-axes 'fields' produced can show variation in *c*-axes within a large quartz grain as well as variation within a region containing very fine grained quartz. This method of *c*-axes determination is much easier to implement than the method described by Beyna *et al.* (1990) and is less time consuming than

conventional petrographic techniques (Turner and Weiss 1963; Martinez 1958; Price 1973, 1980).

References

Beyna, G., Leymarie, P., Buffet, G., & Laurent, N., (1990). Principie de l'analyse des fabriques d'axes C du quartz par le traitement d'images numeriques. *C.R. Acad. Sci. Paris,* **t.310**, **Serie II**, p. 1233-1239.

Fueten, F., (1997). A computer controlled rotating polarizer stage for the petrographic microscope. *Computers & Geosciences* **Vol. 23**, p. 203-208.

Goodchild, J. S., & Fueten, F. Edge detection in petrographic images using the Rotating Polarizer Stage. In prep.

Heilbronner, R. P. & Pauli, C., (1993). Integrated spatial and orientation analysis of quartz *c*-axes by computer aided microscopy. *Journal of Structural Geology*, **Vol 15, Nos. 3-5,** p. 369-382.

Martinez, J. D., (1958). Photometer method for studying quartz grain Orientation. *Bull. Amer. Ass. Petrol. Geologists,* **Vol. 42, No. 3**, p. 588-608.

McKie, C., & McKie, D. (1974). Crystalline Solids. *Halsted Press, New York, 628p.*

Nesse, W. D. (1991). Introduction to Optical Mineralogy. *Oxford University Press, New York, 335p.*

Pauli, C., Schmid, S. M. & Heilbronner, R. P., (1996). Fabric domains in quartz mylonites: localized three dimensional analysis of microstructure and texture. *Journal of Structural Geology*, **Vol 18, No. 10,** p. 1183-1203.

Price, G. P., (1973). The photometric method in microstructural analysis. *American Journal of Science.* **Vol. 273**, p. 523-537.

Price, G. P., (1980). The analysis of quartz *c*-axis fabrics by the photometric method. *Journal of Geology*, **Vol. 88**, p. 181-195.

Turner, F. J., & Weiss, L. E., (1963). Structural Analysis of Metamorphic Tectonites. *McGraw-Hill Book Company, New York, 545p.*

Chapter 6:
Conclusions

Conclusions

The goal of this research was to create an image processing application for analyzing standard petrographic thin sections using the Rotating Polarizer Stage. The research focused on three major areas of petrographic image processing:

1) Edge detection.
2) Mineral grain classification.
3) Partial crystallographic orientation determination for quartz grains.

Edge Detection

For edge detection, a gradient operator was passed across each sequential image taken during the sampling process. Normally, the gradient values at visible boundaries between grains are less than the gradient values in the interior of grains. The gradient values obtained for each pixel are summed in an array element representing that pixel and are scaled to an 8 bit range upon completion of the sampling process. This creates a grey level image with high/bright values representing mineral grain boundaries and low/dark areas representing mineral grain interiors. Applying a series of image processing routines to the gradient image creates a bi-level image containing only edges and interiors. The extracted edges are required to form closed contours. Therefore, there are no dangling or broken boundaries in the final edge extracted image.

Although the edge detection algorithm does a very good job, there are still problems of missing edges and edges occurring in areas where there is no real grain boundary present. These false edges are normally the result of fractures within grains and require further work. One possibility for removal of the false edges would be to use some form of texture analysis on adjacent mineral grains. The grain boundary in question would then only be removed if the two mineral grains were determined to be measurably the same. Other future work could include the development of a method to automatically determine which (if any) grain boundaries were missed. For this, the other composite images obtained in the sampling process may be useful.

Mineral grain classification

The classification algorithm developed during the research for this thesis is a very simple yet effective method of mineral grain categorizing in images of a thin section. Before the algorithm is run, a user must first select, from the image of the thin section, a set of representative grains that include all the mineral types present in the thin section. The classification algorithm uses statistical information from these grains to classify the remainder of the mineral grains within the thin section. The statistical measure used for classification is the mode of the intensity of pixels making up a mineral grain in colour space. Each unknown grain is assigned to the type of the representative grain whose mode is closest to the mode of the unknown grain in question. The accuracy of

classification increases as the number of representative grains selected in the image of the thin section increases.

Although this method works well it is not a truly automated classification procedure. Future research in this area could focus on applying neural nets to the problem of mineral grain classification. The neural nets could allow the computer to be 'taught' how to classify a number of different mineral types on its own, without human aid, as is necessary in the current algorithm. Another area for future research using the current algorithm would be to attempt to devise a method that allows a computer to be able to resolve quartz and feldspars. One possible suggestion would be to use the fact that feldspars exhibit twinning while quartz does not. The twins in feldspars will produce a strong bi-modal intensity distribution which can be used to distinguish the feldspar from quartz.

Partial crystallographic orientation determination for quartz

The algorithm developed for the determination of quartz grain *c*-axis orientations is a quick and accurate alternative to the conventional universal stage method. For each pixel in an image of a thin section, the maximum intensity and the orientation, relative to the planes of polarization, at which the maximum intensity occurred (maximum position) are measured during the rotation of the polarizers through 180^0. For pixels making quartz grains, the maximum position is related to the trend of the *c*-axis, while the maximum intensity value can be related to the plunge of the *c*-axis. The calculated *c*-axes are plotted on an equal area net but can also be overlain on the image of a thin

section. The final results compare favourably when plotted against data obtained on a universal stage.

In summary, the data gathering possibilities of the Rotating Polarizer Stage along with the application of specific image processing routines, creates a powerful computer vision tool to be used by the Earth Scientist when studying rocks in thin section. As it is, the system developed here is still in its infancy. There is still a great deal of work left to do which will surely occupy many people for some time to come. Finally, as computers become faster, larger and more complex algorithms can be employed which will surely improve the quality and accuracy of future petrographic imaging systems.

Appendix I:
Convolutions And The Gradient

Appendix I
Convolutions and the Gradient

Convolutions

To detect changes in image intensity, edge detection algorithms rely on the use of convolution operations using spatial masks. A convolution mask is a weighted matrix operator, usually with an odd number of rows and columns, that is centered on the pixel being investigated (Gonzalez and Woods 1992; Parker 1994) (Figure I.1). Each pixel covered by the mask is multiplied by the value, or weight, of its corresponding position in the mask. The new value of the central pixel is then computed as the sum of the individual products. A convolution is applied to an image as a whole in two steps. First the mask is passed across each pixel in the image storing the new value for each pixel in memory. These new pixel values then replace the original values in the image, producing the convolved image. A convolution normally associated with edge detection is the discrete approximation to the gradient (Kitchen and Malin 1989; Gonzalez and Woods 1992; Parker 1994; Jain *et al.* 1995).

The Gradient

The gradient is the two-dimensional equivalent of the first derivative and is a measure of change of a function (Figure I.2). If we model edges in an image as step discontinuities, edge detection is essentially the operation of locating these significant local intensity changes. Applying a gradient convolution to the

Figure I.1: The convolution operation.
a) Portion of an image that will be convolved by mask in b.
b) Convolution mask passed across each pixel in the image. New values for each pixel in the image are produced as a result of the convolution.

a	b	c	d	e
f	g	h	i	j
k	l	m	n	o
p	q	r	s	t
u	v	w	x	y

(a)

-1	-1	-1
-1	8	-1
-1	-1	-1

(b)

The convolution (a)*(b) at m, producing a new value for m, is:

$$new\_m = 8m - (g + h + i + l + n + q + r + s)$$

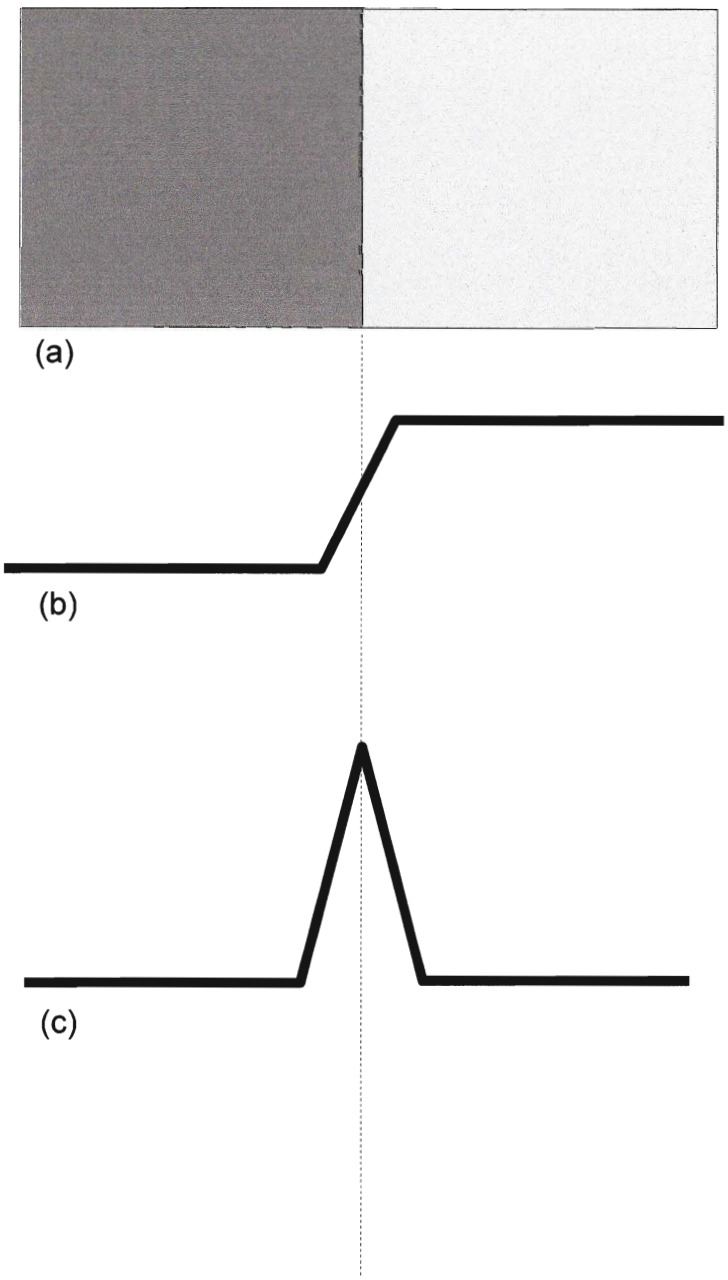
(a)
(b)
(c)

image will localize and enhance significant step discontinuities, while suppressing or flattening the rest of the image.

Considering an image $f(x,y)$ to be a continuous function of image intensity, the gradient of the image at location (x,y) is defined by the vector:

$$\vec{G}[f(x,y)] = \begin{bmatrix} G_x \\ G_y \end{bmatrix} = \begin{bmatrix} \frac{\partial f}{\partial x} \\ \frac{\partial f}{\partial y} \end{bmatrix} \qquad \text{(I.1)}$$

with magnitude

$$G[f(x,y)] = \sqrt{(G_x^2 + G_y^2)} \qquad \text{(I.2)}$$

which can be approximated using absolute values (Jain *et al.* 1995):

$$G[f(x,y)] \approx |G_x| + |G_y| \qquad \text{(I.3)}$$

or $$G[f(x,y)] \approx \max(|G_x|, |G_y|) \qquad \text{(I.4)}.$$

The direction of the gradient is defined as:

$$\alpha(x,y) = \tan^{-1}(G_y / G_x) \qquad \text{(I.5)}$$

where α is the angle measured with respect to the x axis. For the purposes of this study it is worth noting that the magnitude of the gradient is independent of the direction.

Captured petrographic images, however, are not continuous in nature and a discrete approximation to the gradient is required. For captured images, the derivatives in Equation I.1 can be approximated by intensity differences

(Gonzalez and Woods 1992; Parker 1994; Jain *et al.* 1995). The gradient approximations used for each pixel $[x, y]$ are as follows:

$$G_x \cong f[x, y] - f[x-1, y] \qquad \text{(I.6)}$$

$$G_y \cong f[x, y] - f[x, y-1] \qquad \text{(I.7)}.$$

These approximations can be implemented by using the two convolution masks shown below:

$$G_x = \begin{bmatrix} 1 & -1 \end{bmatrix} \qquad G_y = \begin{bmatrix} 1 \\ -1 \end{bmatrix} \qquad \text{(I.8)}.$$

When applied to an image, these simple convolutions will show high values where the image intensity changes rapidly and low values where the image intensity changes slowly.

References

Gonzalez, R. C. & Woods, R. C. (1992). Digital Image Processing. *Addison-Wesley Publishing, New York, 716p.*

Jain, R. Kasturi, R. & Schunck, B. G. (1995). Machine Vision. *McGraw-Hill, New York, 549p.*

Kitchen, L. J. & Malin, J. A. (1989). The Effect of Spatial Discretization on the Magnitude and Direction Response of Simple Differential Edge Operators on a Step Edge. *Computer Vision, Graphics, and Image Processing.* **Vol. 47**, p. 243-258.

Parker, J. R. (1994). Practical Computer Vision Using C. *John Wiley & Sons, Toronto, 476p.*

Appendix II:
Derivation Of The Gaussian Mask Used In Edge Extraction

Appendix II
Derivation of Gaussian Mask Used in Edge Extraction

The Gaussian smoothing mask used in the edge extraction process has the following form:

$$\begin{bmatrix} 1 & 1 & 2 & 2 & 2 & 1 & 1 \\ 1 & 2 & 2 & 4 & 2 & 2 & 1 \\ 2 & 2 & 4 & 8 & 4 & 2 & 2 \\ 2 & 4 & 8 & 16 & 8 & 4 & 2 \\ 2 & 2 & 4 & 8 & 4 & 2 & 2 \\ 1 & 2 & 2 & 4 & 2 & 2 & 1 \\ 1 & 1 & 2 & 2 & 2 & 1 & 1 \end{bmatrix} \qquad \text{(II.1)}$$

The mask weights are computed directly from the discrete Gaussian distribution function

$$g[x,y] = c\exp\left(\frac{-(x^2+y^2)}{2\sigma^2}\right) \qquad \text{(II.2)}$$

where σ determines the degree of smoothing applied and c is a normalizing constant. Dividing both sides by c gives us

$$\frac{g[x,y]}{c} = \exp\left(\frac{-(x^2+y^2)}{2\sigma^2}\right) \qquad \text{(II.3).}$$

Choosing a value of $\sigma = 1$, we can evaluate equation II.3 over a 7x7 pixel window to obtain the mask in II.1. In a 7x7 pixel window, both x and y will obtain values from -3 to 3. Using this, we can build the following array of normalized values with equation II.3.

[X,Y]	-3	-2	-1	0	1	2	3
-3	1	1	2	2	2	1	1
-2	1	2	2	4	2	2	1
-1	2	2	4	8	4	2	2
0	2	4	8	16	8	4	2
1	2	2	4	8	4	2	2
2	1	2	2	4	2	2	1
3	1	1	2	2	2	1	1

The normalization was performed such that the value in the top left corner was equal to 1. This is the convolution mask used in the Gaussian smoothing process. However, the weights of the mask do not sum to 1. Therefore, when the convolution is performed, the value assigned to a pixel must be normalized by the summed weights of the Gaussian mask.

Appendix III:
Complete Derivation Of The Equation Relating Inclination Of Quartz *c*-axes To Maximum Intensity Under Cross Polarized Light

Appendix III

Complete derivation of the equation relating Inclination of quartz *c*-axes to maximum intensity under cross polarized light

In the uniaxial (positive) indicatrix, the two allowed, mutually perpendicular vibration directions, will always lie in an elliptical section that is perpendicular to the wave normal direction of the incident light. The vibration directions are parallel to the axes of the elliptical section and the refractive indices define the lengths of the axes.

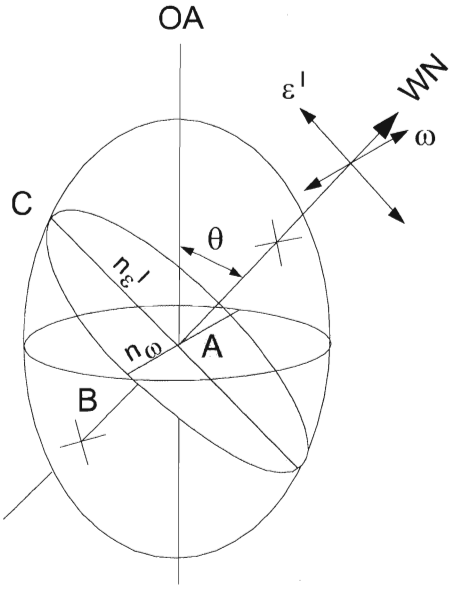

Figure III.1a. Uniaxial positive . indicatrix

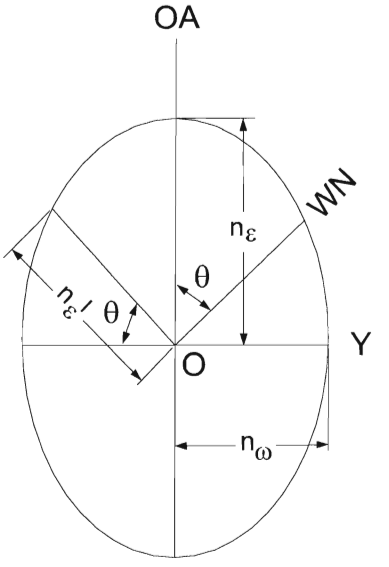

Figure III.1b. Principal section of uniaxial positive indicatrix.

In Figure III.1a, the ordinary ray, ω, vibrates parallel to AB and has refractive index n_ω. The component of the extraordinary ray, ε', vibrates parallel to AC and has refractive index n'_ε and the angle between the wave normal (WN) and the optic axis (OA), θ, is equivalent to the angle between n'_ε and the plane of the circular section (Figure III.1b).

In any uniaxial mineral, such as quartz, the *c* crystallographic axis is coincident with the optic axis of its indicatrix. We also know that the wave normal of the incident light on a thin section in a petrographic microscope is vertically oriented. Hence, the angle θ, in Figure III.1a and Figure III.1b, can be thought of as defining the angle between the *c* crystallographic axis in a quartz grain and vertical.

We can define the principal section of the uniaxial positive indicatrix in Figure III.1b, by the equation of an ellipse:

$$\frac{y^2}{n_\omega^{\,2}} + \frac{z^2}{n_\varepsilon^{\,2}} = 1 \qquad \text{(III.1)}$$

To put equation (III.1) into polar form, let $y = n'_\varepsilon \cos\theta$ and $z = n'_\varepsilon \sin\theta$

$$\frac{n'^{2}_\varepsilon \cos^2\theta}{n_\omega^{\,2}} + \frac{n'^{2}_\varepsilon \sin^2\theta}{n_\varepsilon^{\,2}} = 1 \qquad \text{(III.2)}$$

dividing both sides by n'^{2}_ε

$$\frac{\cos^2\theta}{n_\omega^{\,2}} + \frac{\sin^2\theta}{n_\varepsilon^{\,2}} = \frac{1}{n'^{2}_\varepsilon} \qquad \text{(III.3)}$$

$$\frac{n_\varepsilon^{\,2}\cos^2\theta + n_\omega^{\,2}\sin^2\theta}{n_\omega^{\,2} n_\varepsilon^{\,2}} = \frac{1}{n'^{2}_\varepsilon} \qquad \text{(III.4)}$$

therefore

$$n'^{2}_\varepsilon = \frac{n_\omega^{\,2} n_\varepsilon^{\,2}}{n_\varepsilon^{\,2}\cos^2\theta + n_\omega^{\,2}\sin^2\theta} \qquad \text{(III.5)}$$

We need to solve equation (III.5) for θ. To accomplish this it is desirable to have only one term in the equation that includes θ. Therefore, some re-arranging must be done.

$$n_{\varepsilon}'^{2} = \frac{n_{\omega}^{2} n_{\varepsilon}^{2}}{n_{\varepsilon}^{2}\left(\frac{n_{\omega}^{2}}{n_{\varepsilon}^{2}}\sin^{2}\theta + \cos^{2}\theta\right)} \qquad \text{(III.6)}$$

$$n_{\varepsilon}'^{2} = \frac{n_{\omega}^{2}}{\left(\frac{n_{\omega}^{2}}{n_{\varepsilon}^{2}}\sin^{2}\theta + \cos^{2}\theta\right)} \qquad \text{(III.7)}$$

Adding and subtracting $\sin^{2}\theta + \cos^{2}\theta = 1$ in the denominator

$$n_{\varepsilon}'^{2} = \frac{n_{\omega}^{2}}{\left(\frac{n_{\omega}^{2}}{n_{\varepsilon}^{2}}\sin^{2}\theta + \cos^{2}\theta + \left(\sin^{2}\theta + \cos^{2}\theta\right) - \left(\sin^{2}\theta + \cos^{2}\theta\right)\right)} \qquad \text{(III.8)}$$

$$n_{\varepsilon}'^{2} = \frac{n_{\omega}^{2}}{\left(\frac{n_{\omega}^{2}}{n_{\varepsilon}^{2}}\sin^{2}\theta + \cos^{2}\theta + \left(\sin^{2}\theta - \cos^{2}\theta\right) + \left(\cos^{2}\theta - \sin^{2}\theta\right)\right)} \qquad \text{(III.9)}$$

Using the identities $\sin^{2}\theta - \cos^{2}\theta = 2\sin^{2}\theta - 1$ and $\cos^{2}\theta - \sin^{2}\theta = 1 - 2\sin^{2}\theta$

$$n_{\varepsilon}'^{2} = \frac{n_{\omega}^{2}}{\frac{n_{\omega}^{2}}{n_{\varepsilon}^{2}}\sin^{2}\theta + \cos^{2}\theta + 2\sin^{2}\theta - 1 + 1 - 2\sin^{2}\theta} \qquad \text{(III.10)}$$

$$n_{\varepsilon}'^{2} = \frac{n_{\omega}^{2}}{\frac{n_{\omega}^{2}}{n_{\varepsilon}^{2}}\sin^{2}\theta + \cos^{2}\theta + 2\sin^{2}\theta - \sin^{2}\theta - \sin^{2}\theta} \qquad \text{(III.11)}$$

$$n_{\varepsilon}'^{2} = \frac{n_{\omega}^{2}}{\frac{n_{\omega}^{2}}{n_{\varepsilon}^{2}}\sin^{2}\theta + \cos^{2}\theta + \sin^{2}\theta - \sin^{2}\theta} \qquad \text{(III.12)}$$

$$n_{\varepsilon}'^{2} = \frac{n_{\omega}^{2}}{\left(\left(\frac{n_{\omega}^{2}}{n_{\varepsilon}^{2}}\sin^{2}\theta - \sin^{2}\theta\right) + \left(\cos^{2}\theta + \sin^{2}\theta\right)\right)} \qquad \text{(III.13)}$$

$$n'^{2}_{\varepsilon} = \frac{n_{\omega}^{\ 2}}{\left(\frac{n_{\omega}^{\ 2}}{n_{\varepsilon}^{\ 2}} - 1\right)\sin^2\theta + 1} \qquad \text{(III.14)}$$

Equation (III.14) has only one term involving θ, hence, we can continue and solve for θ.

$$1 + \left(\frac{n_{\omega}^{\ 2}}{n_{\varepsilon}^{\ 2}} - 1\right)\sin^2\theta = \frac{n_{\omega}^{\ 2}}{n'^{2}_{\varepsilon}} \qquad \text{(III.15)}$$

$$\left(\frac{n_{\omega}^{\ 2}}{n_{\varepsilon}^{\ 2}} - 1\right)\sin^2\theta = \frac{n_{\omega}^{\ 2}}{n'^{2}_{\varepsilon}} - 1 \qquad \text{(III.16)}$$

$$\sin^2\theta = \frac{\left(\frac{n_{\omega}^{\ 2}}{n'^{2}_{\varepsilon}} - 1\right)}{\left(\frac{n_{\omega}^{\ 2}}{n_{\varepsilon}^{\ 2}} - 1\right)} \qquad \text{(III.17)}$$

$$\sin^2\theta = \frac{n_{\omega}^{\ 2}}{n_{\omega}^{\ 2}} \frac{\left(\frac{1}{n'^{2}_{\varepsilon}} - \frac{1}{n_{\omega}^{\ 2}}\right)}{\left(\frac{1}{n_{\varepsilon}^{\ 2}} - \frac{1}{n_{\omega}^{\ 2}}\right)} \qquad \text{(III.18)}$$

$$\sin^2\theta = \frac{\left(\frac{1}{n'^{2}_{\varepsilon}} - \frac{1}{n_{\omega}^{\ 2}}\right)}{\left(\frac{1}{n_{\varepsilon}^{\ 2}} - \frac{1}{n_{\omega}^{\ 2}}\right)} \qquad \text{(III.19)}$$

Now, using the identity $\sin^2\theta = \frac{1}{2} - \frac{1}{2}\cos 2\theta$, equation (III.19) becomes

$$\frac{1}{2} - \frac{1}{2}\cos 2\theta = \frac{\left(\frac{1}{n'^{2}_{\varepsilon}} - \frac{1}{n_{\omega}^{\ 2}}\right)}{\left(\frac{1}{n_{\varepsilon}^{\ 2}} - \frac{1}{n_{\omega}^{\ 2}}\right)} \qquad \text{(III.20)}$$

$$\frac{1}{2}\cos 2\theta = \frac{1}{2} - \frac{\left(\frac{1}{n_\varepsilon'^2} - \frac{1}{n_\omega^2}\right)}{\left(\frac{1}{n_\varepsilon^2} - \frac{1}{n_\omega^2}\right)} \qquad \text{(III.21)}$$

$$\cos 2\theta = 1 - 2\frac{\left(\frac{1}{n_\varepsilon'^2} - \frac{1}{n_\omega^2}\right)}{\left(\frac{1}{n_\varepsilon^2} - \frac{1}{n_\omega^2}\right)} \qquad \text{(III.22)}$$

$$2\theta = \cos^{-1}\left[1 - 2\frac{\left(\frac{1}{n_\varepsilon'^2} - \frac{1}{n_\omega^2}\right)}{\left(\frac{1}{n_\varepsilon^2} - \frac{1}{n_\omega^2}\right)}\right] \qquad \text{(III.23)}$$

$$\theta = \frac{1}{2}\cos^{-1}\left[1 - 2\frac{\left(\frac{1}{n_\varepsilon'^2} - \frac{1}{n_\omega^2}\right)}{\left(\frac{1}{n_\varepsilon^2} - \frac{1}{n_\omega^2}\right)}\right] \qquad \text{(III.24)}$$

Equation (III.24) relates the angle between the *c*-axes and vertical to the ratio of partial birefringence to birefringence. However, to utilize this formula we would need to be able to easily measure n'_ε, n_ε and n_ω, which we cannot do. The solution to this problem is to replace the ratio of partial birefringence to birefringence with the ratio of maximum intensity attained in a 180^0 rotation to maximum possible intensity in a 180^0 rotation. The justification for this is as follows:

The theoretical percentage light transmission through the analyzer given by Price (1973) (see also McKie and McKie 1974) is

$$I = \cos^2\phi - \sin 2(\tau - \phi)\sin 2\tau \sin^2\left(\frac{\pi d(n'_\varepsilon - n_\omega)}{\lambda}\right) \qquad \text{(III.25):}$$

where, I represents the percentage of light transmitted through the analyzer; ϕ represents the angle between the allowed vibration directions in the polarizer and analyzer; τ represents the angle between the polarizer's allowed vibration direction and the quartz grain's closest allowed vibration direction; d represents the thickness of the sample; and λ represents the wavelength of the light.

In this study, all measurements were made at $\phi = 90^0$ (crossed polars) and at the position of maximum intensity $\tau = 45^0$ or 135^0. Substituting these values into equation (III.25) produces:

$$I = \sin^2\frac{\pi d(n'_\varepsilon - n_\omega)}{\lambda} \qquad \text{(III.26)}$$

In Uniaxial substances, both of the principal refractive indices are wavelength dependent (McKie and McKie 1974). This means both the size and shape of the indicatrix can vary with wavelength. In quartz, the dispersion of the extraordinary and ordinary rays are small and they follow a similar path (Figure 4.8). Consequently, the dispersion of the birefringence is negligible. This causes the size of the quartz indicatrix to vary with wavelength, with the shape remaining constant.

Hence, for a sample of constant thickness and light of any wavelength, the maximum intensities that different quartz grains, in a thin section, acquire are controlled solely by the birefringence of each individual grain in question.

Using the above mentioned relation we can approximate the birefringence in a quartz grain by the maximum intensity that grain acquires in a 180^0 rotation. To accomplish this mathematically, we replace the term $\left(\frac{1}{n_\varepsilon'^2}-\frac{1}{n_\omega^2}\right)$ in equation (III.24) with the maximum intensity the mineral grain acquires in a 180^0 rotation (I); and the term $\left(\frac{1}{n_\varepsilon^2}-\frac{1}{n_\omega^2}\right)$ in equation (III.24) with the maximum possible intensity a Quartz grain can acquire in a 180^0 rotation (I_{max}). Substituting into equation (III.24) produces:

$$\theta=\frac{1}{2}\cos^{-1}\left[1-2\frac{I}{I_{\max}}\right] \qquad \text{(III.27)}$$

Equation (III.27) relates the *c*-axis orientation measured from the vertical to the intensity ratio the grain acquires in a 180^0 rotation. To finish the equation we now need to have the *c*-axis orientation measured from the horizontal as this is the customary way to measure *c*-axis inclination. To do this we replace θ with $\frac{\pi}{2}-\theta$ in equation (III.27). This produces the final equation relating *c*-axis inclination to the maximum intensity a quartz grain acquires in a 180^0 rotation:

$$\theta=\frac{\pi}{2}-\frac{1}{2}\cos^{-1}\left[1-2\frac{I}{I_{\max}}\right] \qquad \text{(III.28)}$$

Which simplifies to the final form of the equation:

$$\theta=\frac{1}{2}\cos^{-1}\left[2\frac{I}{I_{\max}}-1\right] \qquad \text{(III.29).}$$

References

McKie, C., & McKie, D. (1974). Crystalline Solids. *Halsted Press, New York, 628p.*

Price, G. P., (1973). The photometric method in microstructural analysis. *American Journal of Science.* **Vol. 273**, p. 523-537.

Appendix IV:
Complete Reference List

References

Allard, B. & Benn, K. (1989). Shape Preferred Orientation Analysis Using Digitized Images on a Microcomputer. *Computers & Geosciences,* **Vol. 15**, 441-448.

Beyna, G., Leymarie, P., Buffet, G., & Laurent, N., (1990). Principie de l'analyse des fabriques d'axes C du quartz par le traitement d'images numeriques. *C.R. Acad. Sci. Paris,* **t.310**, **Serie II**, p. 1233-1239.

Canny, J. (1986). A Computational Approach to Edge Detection. *IEEE Trans. Pattern Anal. Mach. Intell.* **PAMI-8(6)**, p. 679-698.

Fabbri, A. G. (1984). Image Processing of Geological Data. *Van Nostrand Reinhold, New York, 224p.*

Foley, J. D., van Dam, A., Feiner, S. K. & Hughes, J. F. (1995). Computer Graphics Principles and Practice. *Addison-Wesley Publishing, New York, 1174p.*

Fueten, F. (1997). A computer controlled rotating polarizer stage for the petrographic microscope. *Computers & Geosciences* **Vol. 23**, p 203-208

Goodchild, J. S., & Fueten, F., Edge detection in petrographic images using the Rotating Polarizer Stage. In prep.

Gonzalez, R. C. & Woods, R. C. (1992). Digital Image Processing. *Addison-Wesley Publishing, New York, 716p.*

Heilbronner, R. P. & Pauli, C., (1993). Integrated spatial and orientation analysis of quartz *c*-axes by computer aided microscopy. *Journal of Structural Geology*, **Vol 15, Nos. 3-5,** p. 369-382.

Horn, B. K. P. (1986). Robot Vision. *MIT Press, Cambridge, Mass, 509p.*

Jain, R. Kasturi, R. & Schunck, B. G. (1995). Machine Vision. *McGraw-Hill, New York, 549p.*

Kitchen, L. J. & Malin, J. A. (1989). The Effect of Spatial Discretization on the Magnitude and Direction Response of Simple Differential Edge Operators on a Step Edge. *Computer Vision, Graphics, and Image Processing*. **Vol. 47**, p. 243-258.

Launeau, P., Bouchez, J.-L. and Benn, K., (1990). Shape preferred orientation of object populations: automatic analysis of digitized images: *Tectonophysics*, **Vol. 180**, p. 201-211.

Lumbreras, F. & Serrat, J. (1996). Segmentation of petrographical images of marbles. *Computers & Geosciences*, **Vol. 22**, p. 547-558.

Marr, D. & Hildreth, E. (1980). Theory of Edge Detection. *Proceedings of the Royal Society of London*, Series B. **Vol. 207**, p. 187-217.

Martinez, J. D., (1958). Photometer method for studying quartz grain Orientation. *Bull. Amer. Ass. Petrol. Geologists,* **Vol. 42, No. 3**, p. 588-608.

Marschallinger, R. (1997). Automatic mineral classification in the macroscopic scale. *Computers & Geosciences*, **Vol. 23**, p. 119-126.

McKie, C., & McKie, D. (1974). Crystalline Solids. *Halsted Press, New York, 628p.*

Nesse, W. D. (1991). Introduction to Optical Mineralogy. *Oxford University Press, New York, 335p.*

Parker, J. R. (1994). Practical Computer Vision Using C. *John Wiley & Sons, Toronto, 476p.*

Pauli, C., Schmid, S. M. & Heilbronner, R. P., (1996). Fabric domains in quartz mylonites: localized three dimensional analysis of microstructure and texture. *Journal of Structural Geology*, **Vol 18, No. 10,** p. 1183-1203.

Pfleiderer, S., Ball, D.G.A and Bailey, R.C. (1992). AUTO: A computer program for the determination of the two-dimensional auto-correlation function of digital images: *Computers & Geosciences*, **Vol. 19**, p. 825-829.

Petruk, W., ed. (1989). Image analysis in Earth Sciences: *Mineralogical Association of Canada Shortcourse Handbook*

Price, G. P., (1973). The photometric method in microstructural analysis. *American Journal of Science.* **Vol. 273**, p. 523-537.

Price, G. P., (1980). The analysis of quartz *c*-axis fabrics by the photometric method. *Journal of Geology*, **Vol. 88**, p. 181-195.

Richards, J.A. (1986). Remote Sensing Digital Image Analysis An Introduction. *Springer-Verlag, New York.*

Samantaray, A. K. (1993). Computer assisted petrographic image analysis and quantization of rock textures. Unpublished Ph.D. thesis, *University of Western Ontario, Ontario, Canada, 176p.*

Shoji, T. (1991). An interactive system to assist mineral identification with the petrographic microscope. *Geoinformatics* **Vol. 2**, p. 219-224.

Shoji, T., & Hiroaki, K. (1994). An interactive system to assist in mineral identification in ore microscopy. *Mathematical Geology* **Vol. 26 No. 8**, p. 961-972.

Simigian, S. & Starkey, J. (1989). IMAGE: Modified For Use on a Microcomputer Based System. *Computers & Geosciences*. **Vol. 15**, p. 237-254.

Starkey, J. and Samantaray, A.K., (1991). An evaluation of noise reduction filters, with particular reference to petrographic images: *Journal of Computer-Assisted Microscopy*, **Vol. 3**, p. 171-188.

Starkey, J. & Samantaray, A. K. (1993). Edge Detection in Petrographic Images. *Journal of Microscopy*. **Vol. 172**, p. 263-266.

Turner, F. J., & Weiss, L. E., (1963). Structural Analysis of Metamorphic Tectonites. *McGraw-Hill Book Company, New York, 545p.*

Venkatesh, S. & Kitchen, L. J. (1992). Edge Evaluation Using Necessary Components. *Computer Vision, Graphics and Image Processing: Graphical Models and Image Processing*. **Vol. 54**, p. 23-30.

Wang, L. (1995). Automatic identification of rocks in thin sections using textural analysis. *Mathematical Geology* **Vol. 27 No. 7**, p. 847-865.